



Modeling and Simulation of Charge Carrier
Recombination Dynamics in $\text{Cu}(\text{In},\text{Ga})\text{Se}_2$
Thin Film Solar Cells

Von der Fakultät für Mathematik und Naturwissenschaften der Carl
von Ossietzky Universität Oldenburg zur Erlangung des Grades eines

Doktors der Naturwissenschaften (Dr. rer. nat)

angenommene Dissertation

von

José Fabio López Salas

geboren am 14.09.1990

in San José, Costa Rica

Betreuer: **Dr. Stephan J. Heise**

Erstgutachter: **Prof. Dr. Jürgen Parisi**

Zweitgutachter: **PD. Dr. Petra Groß**

Tag der Disputation: 12.04.2018

Abstract

Solar cells with thin $\text{Cu}(\text{In,Ga})(\text{S,Se})_2$ absorber films are well established in the photovoltaics market. They offer an advantage over other thin film technologies thanks to their lower content of elements with high toxicity or low earth abundance like cadmium and tellurium. One approach to further improve the quality of production of these cells is to develop a method of material quality assessment during production that is fast, contactless and non-destructive. Time-resolved photoluminescence (TRPL) measurements offer all these characteristics. Previous works show indications that a correlation may exist between measured photoluminescence decay lifetimes of bare $\text{Cu}(\text{In,Ga})(\text{S,Se})_2$ absorber films and the photoconversion efficiency of entire solar cells produced from those films. However, in other sources it has been reported that this correlation can be broken under certain conditions, for example when the density of defect states inside the band gap fluctuates between samples.

This work aims to establish the requirements to extract meaningful information about charge carrier recombination dynamics and solar cell performance parameters from TRPL measurements. To achieve this goal experiments and simulations are carried out. The material parameters are extracted from experiments and are then built into the simulation model. Results from experiments also serve as the basis to verify the validity of this model. Parameter variations within the simulations function as one of the main methods in this work to gain deeper physical insight into the processes taking place during TRPL measurements.

This work concentrates on the sulfur-free material $\text{Cu}(\text{In,Ga})\text{Se}_2$. Using the simulation model, results of experiments are accurately reproduced. This includes TRPL decay curves as well as measurements in quasi-steady-state conditions (EQE, IV). Utilizing the insight gained from simulations, predictions about the behavior of $\text{CdS}/\text{Cu}(\text{In,Ga})\text{Se}_2$ junctions in TRPL experiments at different injection levels are made. These prediction are experimentally tested.

The results show that additional data about material composition is needed to gain truly reliable information about solar cell performance from TRPL measurements. This is because fluctuation in certain material parameters, e.g. band gap grading, can result in a non-correlation between photoluminescence decay lifetime and open circuit voltage. Moreover, experiments and simulations show that the presence of a p-n junction at the $\text{CdS}/\text{Cu}(\text{In,Ga})\text{Se}_2$ interface can significantly alter the results of TRPL measurements at sufficiently low injection levels. The injection level at which this becomes an issue, according to the results, is dependent on the doping concentration of the absorber. An experimental method of extraction of the doping concentration of very thin (<100 nm) CdS buffer layers, so far not available experimentally, is proposed based on these results.

Kurzfassung

Solarzellen mit dünnen Cu(In,Ga)(S,Se)_2 -Absorberschichten sind bereits auf dem Photovoltaikmarkt etabliert. Ihr geringerer Inhalt an toxischen oder seltenen Elementen wie Cadmium oder Tellur ist einer ihrer Vorteile gegenüber anderen Dünnschichttechnologien. Ein Ansatz, um die Produktionsqualität dieser Zellen zu steigern, ist die Entwicklung einer kontaktlosen und zerstörungsfreien Methode zur Qualitätsauswertung während der Produktion. Zeitaufgelöste Photolumineszenzmessungen (auf Englisch: „time-resolved photoluminescence“, abgekürzt: „TRPL“) erfüllen alle diese Bedingungen. Die Literatur enthält Hinweise auf eine Korrelation zwischen der gemessenen Zerfallszeit der Photolumineszenz reiner Cu(In,Ga)(S,Se)_2 -Absorberschichten und der photovoltaischen Effizienz ganzer Solarzellen aus dem gleichen Material. Gleichzeitig wird in anderen Quellen berichtet, dass diese Korrelation unter bestimmten Bedingungen verletzt wird, zum Beispiel wenn die Dichte der Defekte innerhalb der Bandlücke zwischen Proben fluktuiert.

Das Ziel dieser Arbeit ist, die notwendigen Bedingungen zu erkennen, bei denen TRPL-Messungen zuverlässige Informationen über die Rekombinationsdynamik der Ladungsträger und die Leistungsparameter der Solarzellen liefern. Zu diesem Zweck werden Simulationen und Experimente durchgeführt. Die Materialparameter werden mithilfe von Experimenten bestimmt und in das Simulationsmodell eingebaut. Darüber hinaus dienen die Experimente als Grundlage, um die Gültigkeit des Simulationsmodells zu überprüfen. Parametervariationen innerhalb der Simulationen sind eine der Hauptmethoden in dieser Arbeit, um das physikalische Verständnis über die Prozesse, die bei TRPL-Experimenten eine Rolle spielen, zu vertiefen.

Diese Arbeit befasst sich mit dem schwefelfreien Absorbermaterial Cu(In,Ga)Se_2 . Mittels Simulationen werden die Ergebnisse aus optoelektronischen Experimenten in quasi-stationären Bedingungen (EQE, IV) und aus zeitaufgelösten Photolumineszenz-Messungen (TRPL) reproduziert. Basierend auf den Ergebnissen dieser Simulationen, wird das Verhalten von CdS/Cu(In,Ga)Se_2 -Schichtstapeln in TRPL-Experimenten bei unterschiedlichen Anregungsdichten vorhergesagt. Diese Vorhersagen werden wiederum experimentell überprüft.

Die Ergebnisse zeigen, dass zusätzliche Daten über die Zusammensetzung des Materials notwendig sind, um aussagekräftige Informationen über die Solarzellenleistung aus TRPL-Messungen zu gewinnen. Der Grund hierfür ist, dass Schwankungen im Wert bestimmter Materialparameter, wie der Stärke der Bandlückengraduierung, eine fehlende Korrelation zwischen Zerfallszeit der Photolumineszenz und Leerlaufspannung ergeben können. Außerdem zeigen Experimente und Simulationen, dass das Auftreten eines p-n-Übergangs an der Grenzschicht CdS/Cu(In,Ga)Se_2 die Ergebnisse aus TRPL-Messungen signifikant beeinflussen kann, wenn die Anregungsdichte niedrig genug gewählt wird. Des Weiteren zeigt sich, dass der spezifische Wert der Anregungsdichte, bei dem dieser Effekt auftritt, abhängig von der Dotierkonzentration des Absorbermaterials ist. Darauf aufbauend wird eine experimentelle Methode zur Auswertung der Dotierkonzentration sehr dünner (<100 nm) CdS -Pufferschichten formuliert.

Contents

Abstract	v
Kurzfassung	vii
1 Introduction	1
2 Theory	5
2.1 Cu(In,Ga)Se ₂ solar cells	5
2.1.1 Basic functioning principle	5
2.1.2 Charge carrier statistics	7
2.1.3 Optical generation	10
2.1.4 Charge carrier dynamics	11
2.1.5 Device structure	15
2.1.6 Metastability	16
2.2 Time-resolved photoluminescence	17
2.2.1 Injection Level	18
2.2.2 Contribution of defect states	19
2.2.3 Inhomogeneities	22
3 Methods	27
3.1 Experimental setups	27
3.1.1 Time-resolved photoluminescence	27
3.1.2 Electrical characterization	32
3.2 Lifetime extraction	33
3.3 Simulation	35
3.3.1 Introduction to the simulation tool	35
3.3.2 Simulation model	36
3.3.3 Material parameters	41
4 Results	43
4.1 Parameter study and metastability	43
4.1.1 Research steps	44
4.1.2 Results	45
4.1.3 Summary	48

4.2	Correlation between photoluminescence lifetime and open circuit voltage	50
4.2.1	Theory	50
4.2.2	Research steps	51
4.2.3	Results	54
4.2.4	Summary	58
4.3	Influence of p-n junction	60
4.3.1	Theory	60
4.3.2	Research steps	60
4.3.3	Results	63
4.3.4	Summary	71
4.4	General Discussion	74
5	Summary	77
	Appendices	I
	Bibliography	III
	Publications	XI
	Danksagung	XIII
	Agradecimientos	XV
	Erklärung	XVII
	Lebenslauf	XIX

1 Introduction

Photovoltaic technology steadily gains more importance as the installed capacity for electric current production from photovoltaics increases worldwide every year [1]. In Germany the percentage of electric production from renewable sources also rises continuously, having surpassed the 30% mark in recent years [2]. From this total renewable capacity in Germany, photovoltaics covers more than 20% of the total current production [2]. Among the available photovoltaic technologies, thin film devices present the most potential to reduce production costs due to their low material consumption and very high absorption coefficients [3, 4]. Of the two dominant thin film photovoltaic technologies not based on silicon, $\text{Cu}(\text{In}_{1-x}\text{Ga}_x)(\text{S}_{1-y}\text{Se}_y)_2$ cells make use of less toxic materials when compared to CdTe devices [5]. With laboratory record efficiencies of 22.6% [6] and submodule efficiencies of 19.2% [7, 8], $\text{Cu}(\text{In,Ga})(\text{S,Se})_2$ solar cells have managed to stay competitive. The focus of current research on this material is to close the gap between record and module efficiencies. To achieve this goal, it is important to develop methods of reliable and fast material quality assessment applicable during production.

Time-resolved photoluminescence (TRPL) is a fast, contactless and non-destructive method of analysis for thin-film semiconductor materials. In TRPL, a time profile of the decay in the emission of photoluminescence (PL) of the material is measured. This is done after illumination with a short pulse which excites the charge carriers. TRPL is a very flexible method thanks to the possibility to tune the spectrum of excitation, spectrum of detection as well as the time scales investigated. This makes it suitable for a wide variety of fields, e.g. physics, chemistry and biology. In the field of semiconductor physics this method gains its importance due to the relation between basic material characteristics like recombination and diffusion rates of charge carriers and the time development of TRPL decay curves. Therefore, such measurements can provide insight into the recombination behavior and lifetime of charge carriers in thin-film semiconductor materials. All these attributes make TRPL a powerful tool to characterize thin-film materials for photovoltaic applications. This also gives TRPL measurements the potential to become a method of quality assessment during production of thin-film solar cells.

A deep understanding of the investigated system is vital to gain meaningful interpretations from TRPL measurements. As mentioned above, the time development of TRPL decay curves is closely related to the charge carrier dynamics, i.e. generation, recombination, drift and diffusion. By use of simulation methods it becomes possible to investigate the influence that these physical processes have on the TRPL behavior of samples. Additionally, computational simulations are helpful for the interpretation of the data, as they provide a tool to analyze the role of physical parameters in

1 Introduction

the model used to describe the system. Simultaneously, simulations shall be based on experimental results, as these are the reference point for what the simulation model should be able to describe. Moreover, to ensure that simulations describe the behavior of real samples, parameter values obtained from experiments must be included into the simulations. One advantage that simulations have over experimental approaches however, is the possibility to investigate the influence of parameters that are not experimentally reachable or that cannot be externally tuned. Simulations also serve to evaluate previous assumptions about the system by testing the physical model. By reproducing some of the basic features present in TRPL decay curves via simulations, a deeper insight into the physical processes taking place during TRPL measurements can be achieved.

The goal of this work is not a numerically accurate reproduction of experimental data via simulation, but rather a principle understanding of the physical interactions giving shape to the time development of PL emission. For this, the role of basic input parameters in the simulation model must be investigated. Once this is achieved, a further goal is to develop a method of quality assessment of $\text{Cu}(\text{In,Ga})(\text{S,Se})_2$ samples only by TRPL measurements. With these goals in mind, this work is divided into the following chapters.

In the Theory chapter the focus lies on the information necessary to understand the physical system being investigated. This includes the basic characteristics of the $\text{Cu}(\text{In,Ga})(\text{S,Se})_2$ thin film material and the physical models needed to describe its interaction with short light pulses. Additionally, several analytical models used to calculate the time evolution of PL decay are presented.

In the Methods chapter the most important questions surrounding experiment, simulation and data analysis are answered: What are the physical requirements for experimental setups used to investigate the subjects of this work? What information is accessible from the measurements carried out with these setups? What are the requirements that the simulation model must meet to be able to produce meaningful results?

In the Results chapter the analysis and interpretation of data from simulations and experiments is divided into four sections. Each section is dedicated to a specific topic. In the first section the roles of individual model parameters and of metastable changes in the studied samples are investigated. The second section focuses on the validity of using TRPL to characterize photovoltaic efficiency. An investigation on the possible types of correlation between photoluminescence lifetime and open circuit voltage is presented. The third section explores the influence of p-n junctions on the time development of PL emission. In this section the predictive power of the simulation model is tested. The second and third question provide insight into how and when TRPL is suitable as a method of material quality assessment for $\text{Cu}(\text{In,Ga})\text{Se}_2$ thin film absorbers. A fourth and last section provides a discussion of the assumptions made at each step and how they affect the interpretation of the results, as well as presenting questions left open for future investigations.

One of the new contributions in this work is the application of a simulation model capable of reproducing not only time-resolved PL experiments of the bare absorber and of p-n-junctions containing the absorber, but also the data from electric characterization methods of entire cells, such as current-voltage characteristics and quantum efficiency spectra. So far no such model has been presented. The other main new contribution of this work are the findings produced by

applying this simulation model to reproduce experimental data and predict the results of new experiments. By this method it was recognized that among the material parameters measured to change in Cu(In,Ga)Se₂ absorbers due to their metastable behavior, the doping concentration is the one contributing the most to the observed metastable changes in TRPL decay [9]. Moreover, it was found that fluctuations in the amplitude of the gallium content grading along the depth of the Cu(In,Ga)Se₂ material can disturb the correlation between photoluminescence decay lifetime of the absorber and the open circuit voltage of solar cells produced from it [10]. This point relates to the application of TRPL as a method of material quality assessment during production. With these results it becomes apparent that additional information about the material composition of the absorber is necessary before meaningful data about the solar cell efficiency can be gained from TRPL measurements. Additionally, it was shown that under low injection conditions and high doping concentrations, the presence of a thin CdS buffer layer on top of the absorber can have a significant influence on the TRPL behavior of the samples, making such measurements not suitable for the characterization of the charge carrier lifetimes of pure absorbers. With simulations, this effect was shown to stem from the influence of charge carrier separation in the space charge region.

The simulation model presented here builds upon the model developed by Heise et al. [11], adding the time-resolved component for TRPL simulations. The computational tool Sentaurus TCAD from Synopsys was used to perform the simulations. The samples investigated in this work were fabricated by the industry partner Manz AG and are of the sulfur-free type Cu(In,Ga)Se₂. This work has its basis on the work of V. Gerliz [12], from which the experimental data in some of the chapters are originated.

2 Theory

In this chapter the theoretical framework is presented. The first section contains the physics concerning the description of $\text{Cu}(\text{In,Ga})\text{Se}_2$ solar cells, while the second section addresses the knowledge required to interpret time-resolved photoluminescence measurements correctly. The contents of this chapter are the base necessary to understand the simulation model, simulation tool, results and discussion presented in later chapters.

2.1 $\text{Cu}(\text{In,Ga})\text{Se}_2$ solar cells

In this section the structure and working principle of $\text{Cu}(\text{In,Ga})\text{Se}_2$ solar cells are detailed. First the device structure will be discussed, followed by a general description of the physical principles driving a solar cell. Thereafter a more in-depth analysis of each aspect of the physics needed to accurately describe the behavior of such a cell after excitation with a laser pulse will be carried out. From here on the abbreviation “CIGS” represents the more general family of materials $\text{Cu}(\text{In,Ga})(\text{S,Se})_2$, while the short form “CIGSe” stands for the sulfur-free type of cells, which are the focus of this work.

2.1.1 Basic functioning principle

Inorganic solar cells are semiconductor devices capable of absorbing light in order to generate a gradient in electrochemical potential energy of holes and electrons, which then drives an electrical current that can be used to feed an electrical load. The overall effect is the transformation of solar energy into electrical energy.

Semiconductor materials are characterized by their energetic band structure containing at least one band gap of less than 4 eV in size [13]. A zero band gap would correspond to a metallic material, while a larger band gap would correspond to an insulator. The gaps in the electronic structure are a result of the overlapping wave functions of electrons in a spatially periodical potential, such as the one present in the crystal structure of semiconductors [13].

A semiconductor is capable of absorbing photons that have an energy equal to or larger than its energetic band gap. The absorption of a photon elevates an electron from a state in the lower valence band to a state in the higher conduction band. This effectively leaves an electron vacancy in the valence band. The vacancy can be filled by electrons from neighboring atoms if there is a

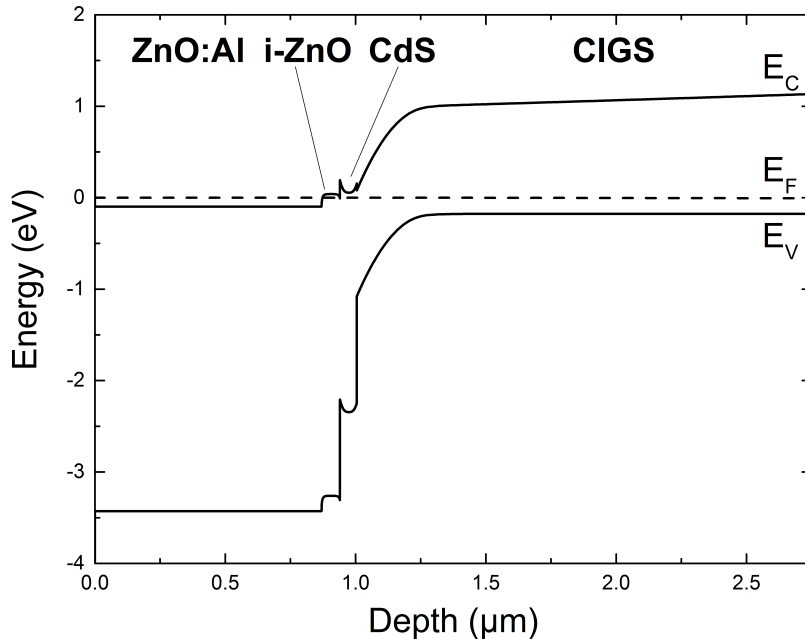


Figure 2.1: Band diagram of a CIGS solar cell in dark conditions and equilibrium. The conduction band edge E_C , valence band edge E_V and Fermi energy E_F have been calculated via simulation. The layer structure is displayed: a window layer consisting of aluminum doped ZnO (ZnO:Al) and intrinsic ZnO (i-ZnO), a CdS buffer layer and a CIGS absorber layer. Also visible is the bending of the energetic bands at the space charge region near the junction between p-layer (CIGS) and n-layers (ZnO/i-ZnO/CdS).

sufficient potential difference driving the transport of electrons. As the vacancy moves throughout the crystal, it behaves as a quasi-particle, called a “hole”, with charge $+q$ (in contrast to an electron which has charge $-q$) and an effective mass that depends on the dispersion relation of the material. The density of states in conduction and valence band of semiconductors can be different, and therefore the effective mass of electrons and holes is often not the same. Notably, holes have the behavior of moving towards higher electrical potential. As a result, an electron-hole pair generated at a location with a proper gradient of electrochemical potential will be separated, since both charge carriers are driven in opposite directions by the electrochemical force, as long as the mobility of at least one of the two types of charge carriers is sufficiently high.

To achieve a gradient in electrochemical potential, most solar cells make use of a p-n junction. This refers to the contacting of two semiconductors of the same or of different materials, one of which is p-doped and the other, while the other one is n-doped.

When in the dark, the difference between the two materials in charge carrier densities of each type creates a chemical potential that drives the diffusion of electrons into the p-material and of holes into the n-material. As an effect of this diffusion the region closest to the interface in each material becomes electrically charged. This region is called the space charge region. The space charge region grows up to a size at which the electric potential induced by the separation of charges exactly counteracts the chemical potential created by the difference in charge carrier concentrations between both sides. This point of dynamic equilibrium is characterized by having no gradient in

the electrochemical potential at the p-n junction and thus there is no net force driving an electrical current. This can be seen most clearly in Fig. 2.1 as the Fermi level is completely flat.

Under illumination the equilibrium is disturbed by the excitation of electron-hole pairs by absorption of photons. In this case a single Fermi energy is not sufficient to describe the statistics of holes and electrons simultaneously. Instead the concept of quasi Fermi levels, one for each type of charge carrier, is introduced. More details about the statistics of charge carriers in semiconductors can be found in section 2.1.2.

In illuminated conditions the generated electron-hole pairs can recombine in most of the volume of each material, however, in the space charge region the electric field mentioned previously drives electrons in the p-material towards the n-side. Similarly the field drives holes in the space charge region of the n-material towards the p-side, where they can recombine with the electrons. This current is driven as long as electron-hole pairs are being generated by illumination. The overall effect is the separation of electron-hole pairs generated in the space charge region, which then contribute to an electrical current driven by the electrochemical potential gradient at the p-n junction and which exists as long as the device is illuminated.

In the next sections, the physics needed to describe a solar cell are discussed in more detail.

2.1.2 Charge carrier statistics

In a semiconductor, the total charge carrier densities are calculated by the integral of their density of states as a function of energy multiplied with the corresponding Fermi probability of occupation of those states [14].

$$n = \int_{E_C}^{\infty} D_C(E) \left[\exp\left(\frac{E - E_{F,n}}{kT}\right) + 1 \right]^{-1} dE \quad (2.1)$$

$$p = \int_{-\infty}^{E_V} D_V(E) \left(1 - \left[\exp\left(\frac{E - E_{F,p}}{kT}\right) + 1 \right]^{-1} \right) dE \quad (2.2)$$

Here n is the density of electrons, p is the density of holes, $D_C(E)$ stands for the density of states in the conduction band, while $D_V(E)$ is the density of states in the valence band, $E_{F,n}$ is the Fermi energy of electrons and $E_{F,p}$ is the Fermi energy of holes, E_V is the energy of the valence band edge and E_C is the energy of the conduction band edge.

The charge carrier densities can alternatively be expressed as a function of the effective density of states in the conduction band N_C , the effective density of states in the valence band N_V and of the Fermi-Dirac integral $F_{1/2}(x)$ [15]:

$$n = N_C F_{1/2}\left(-\frac{E_C - E_{F,n}}{kT}\right) \quad (2.3)$$

$$p = N_V F_{1/2} \left(-\frac{E_{F,p} - E_V}{kT} \right) \quad (2.4)$$

$$F_{1/2}(\eta_F) = \int_0^{\infty} \frac{\eta^{1/2}}{1 + \exp(\eta - \eta_F)} d\eta \quad (2.5)$$

One simplified way of expressing the densities n and p is by using the Boltzmann approximation $E_F < (E_C - 3kT)$. In this case the expressions simplify to give the following:

$$n = N_C \exp \left(-\frac{E_C - E_{F,n}}{kT} \right) \quad (2.6)$$

$$p = N_V \exp \left(-\frac{E_{F,p} - E_V}{kT} \right) \quad (2.7)$$

Two factors γ_n and γ_p describe the ratio between the charge carrier densities calculated with Fermi statistics and the Boltzmann approximation.

$$\gamma_{n,p} = \frac{F_{1/2}(-\eta_{n,p})}{\exp(-\eta_{n,p})} \quad (2.8)$$

$$\eta_p = \frac{E_C - E_{F,n}}{kT} \quad (2.9)$$

$$\eta_p = \frac{E_{F,p} - E_V}{kT} \quad (2.10)$$

From the effective density of states N_C and N_V , the effective mass of electrons m_e^* and of holes m_h^* are calculated using following equations [14]:

$$\frac{m_e^*/h}{m_{e,0}} = \left(\frac{N_{C/V}(300 \text{ K})}{2 \left(\frac{2\pi k_B}{h^2} \right)^{3/2} (m_{e,0} \cdot 300 \text{ K})^{3/2}} \right)^{2/3} = \left(\frac{N_{C/V}(300 \text{ K})}{2.5049 \cdot 10^{19} \frac{1}{\text{cm}^3}} \right)^{2/3} \quad (2.11)$$

By using Eq. (2.6) and Eq. (2.7) the equilibrium charge carrier densities n_0 and p_0 can be defined, by assuming thermal equilibrium and no external optical generation. This means there is a single intrinsic Fermi level $E_{F,i} = E_{F,n} = E_{F,p}$. The intrinsic charge carrier density n_i is then a function of the band gap E_g [16].

$$n_i^2 = n_0 p_0 = N_C N_V \exp \left(-\frac{E_g}{kT} \right) \quad (2.12)$$

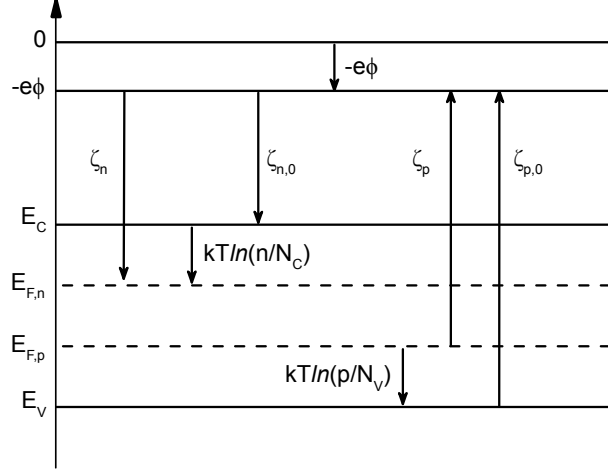


Figure 2.2: Schematic of all contributions to the electrochemical potentials of electrons and holes.

Lastly, the results of Eq. (2.6) and Eq. (2.7) can be combined to calculate the intrinsic Fermi energy $E_{F,i}$.

$$E_{F,i} = \frac{E_C + E_V}{2} + \frac{1}{2}kT \ln \left(\frac{N_V}{N_C} \right) \quad (2.13)$$

The Fermi energies of holes and electrons can be also seen as their electrochemical potentials, being composed of an electrical potential $q\varphi$ and a chemical potential $\zeta_{n,p}$, which depend on the affinity of the charge carriers $\zeta_{n,p,0}$, their total density and the density of states in the conduction and valence bands [14].

$$E_{F,n} = -q\varphi + \zeta_n = -q\varphi + \zeta_{n,0} + kT \ln \left(\frac{n}{N_C} \right) \quad (2.14)$$

$$E_{F,p} = -q\varphi - \zeta_p = -q\varphi - \zeta_{p,0} - kT \ln \left(\frac{p}{N_V} \right) \quad (2.15)$$

Moreover, the energy band edges can also be represented as a function of the electric potential and the material characteristic electron affinity.

$$E_C = \zeta_{n,0} - q\varphi \quad (2.16)$$

$$E_V = \zeta_{n,0} - q\varphi - E_g \quad (2.17)$$

Figure 2.2 shows the relations between the Fermi levels and all contributing potentials.

2.1.3 Optical generation

Photons enter the sample from the top and generate electron-hole pairs. In Fig. 2.1 this would correspond to a propagation of photons in a direction from left to right. The absorption of photons is dependent on the absorption coefficient, which itself is material dependent and also a function of photon energy. For semiconductor materials the absorption spectrum contains an edge at the wavelength of photons with energy close to or equal to their band gap E_g . For photons of shorter wavelengths, i.e higher energies, the absorption is considerable, while for photons of longer wavelength, absorption is much lower or negligible. The transition between these two regimes can be very sharp for direct semiconductors or less steep for indirect semiconductors. Since the band gaps of the ZnO, i-ZnO and CdS layers are larger than that of CIGSe, it becomes possible to choose a wavelength such that the absorption in all layers other than CIGSe is negligible. These conditions are met for TRPL measurements, as will be described in more detail in section 3.1.1. For measurements of current-voltage characteristics and quantum efficiency spectra the illumination spectrum is different, as will also be discussed in section 3.1.2 and therefore there is absorption in all layers. In this section the case of absorption only in the CIGSe material is further discussed.

After a pulsed excitation described by a delta pulse $\delta(t)$, which is a reasonable approximation for pulses of a width much shorter than the photoluminescence lifetime, electron-hole pairs are generated in the absorber material. With an absorption coefficient α , dependent on the wavelength λ , the generation of electron-hole pairs G over the depth x follows the Beer-Lambert law and is described by following equation:

$$G(x, t) = \alpha I_0 \exp(-\alpha x) \delta(t) \quad (2.18)$$

This function gives a depth profile for the generated density of charge carriers. This equation can be used to define an initial state in simulations of TRPL measurements. From this initial state, which is not in equilibrium, the dynamics of the charge carriers are governed by the processes of recombination, drift and diffusion, which will be discussed in section 2.1.4.

From the overall number of photons reaching the uppermost layer of the sample, a certain fraction is reflected. The fraction of photons reflected depends on the real part of the refractive index of the two materials at the interface (n_1, n_2). For the case of normal incidence it is described by the reflection coefficient R with following formula:

$$R = \left| \frac{n_1 - n_2}{n_1 + n_2} \right|^2 \quad (2.19)$$

More details about the optical generation model used in the simulations can be found in section 3.3.2.

2.1.4 Charge carrier dynamics

After charge carriers have been excited, three main mechanisms affect their behavior. The first two are drift and diffusion, which are defined by the electrochemical potential. The third one is recombination, which can happen radiatively from band to band, also called radiative recombination, or via defect states, which can be bulk defect states or interface defect states. The physics of solar cells have been described in great detail by Würfel [14] and are summarized here.

Current densities

The density of charge carriers in semiconductors follows the continuity equations. These are derived from the fundamental laws of conservation. In a given unit of volume in a semiconductor, any change over time in the density of charge carriers is a result of electric current, recombination or generation. This can be written as:

$$\frac{\partial n}{\partial t} = -\frac{1}{q}\nabla\vec{J}_n + (G_n - R_n) \quad (2.20)$$

$$\frac{\partial p}{\partial t} = -\frac{1}{q}\nabla\vec{J}_p + (G_p - R_p) \quad (2.21)$$

These equations contain all the possible mechanisms contributing to the time evolution of the charge carrier densities. Here q is the charge of an electron, $\vec{J}_{n,p}$ are the current densities of holes and electrons, while $G_{n,p}$ stands for the total generation rate and $R_{n,p}$ for the total recombination rate.

The charge carrier current densities are a result of a gradient in the electrochemical potential [14]:

$$\vec{J}_n = -\mu_n n \nabla(-q\varphi + \zeta_n) \quad (2.22)$$

$$\vec{J}_p = -\mu_p p \nabla(q\varphi + \zeta_p) \quad (2.23)$$

Here $\mu_{n,p}$ stand for the mobilities of electrons and holes respectively. From the definitions of the Fermi energies in Eq. 2.14 and 2.15, these expressions can then be simplified to:

$$\vec{J}_n = -\mu_n n \nabla E_{F,n} \quad (2.24)$$

$$\vec{J}_p = \mu_p p \nabla E_{F,p} \quad (2.25)$$

In summary, the total current of electrons and holes is defined by the product of their respective densities, mobilities and the gradient of their electrochemical potentials. To reach this result the assumption of an Einstein relation between diffusion coefficients $D_{n,p}$ and mobilities $\mu_{n,p}$ was made.

$$D_{n,p} = \frac{\mu_{n,p}kT}{q} \quad (2.26)$$

Radiative recombination

The theory of radiative recombination in photoluminescence of semiconductors is explained in great detail by Ahrenkiel and Lundstrom [17]. In this section the most relevant points for the description of radiative recombination are summarized.

The radiative recombination rate R_{rad} is a function of position and time and is described at one location by the following equation:

$$R_{rad} = -\frac{dn}{dt} = B_{rad}np = B_{rad}(n_0 + \Delta n)(p_0 + \Delta p) \quad (2.27)$$

Here n_0 and p_0 describe the electron and hole concentration in equilibrium, while Δn and Δp describe the excess carrier concentrations after excitation. In the case of a p-type absorber this equation can be simplified by assuming that the hole concentration is given by the doping concentration $p_0 = N_A$, which is also much larger than the density of electrons in equilibrium $N_A \gg n_0$. Additionally, it is assumed that the density of electrons in equilibrium is negligible when compared to the density of excited electrons $n \approx \Delta n$.

$$R_{rad} = -\frac{dn}{dt} = B_{rad}(N_A n + n^2) \quad (2.28)$$

This represents a differential equation for the density of electrons n . Since the term n^2 is contained in the equation, this case is commonly called the case of bimolecular recombination. The solution to this differential equation, which here will be called the ‘‘bimolecular model’’ is given by the following formula:

$$n(t) = \frac{\Delta n_0 \exp(-t/\tau_{rad})}{1 + \frac{\Delta n_0}{N_A} [1 - \exp(-t/\tau_{rad})]} \quad (2.29)$$

Here Δn_0 corresponds to an initial density of electrons after excitation with a laser pulse. The radiative lifetime τ_{rad} is defined as follows:

$$\tau_{rad} = \frac{1}{B_{rad}N_A} \quad (2.30)$$

To calculate the radiative recombination as a function of time, Eq. (2.29) can then be inserted into Eq. (2.28). The formula for $n(t)$ can be simplified further if the density of excited electron-hole

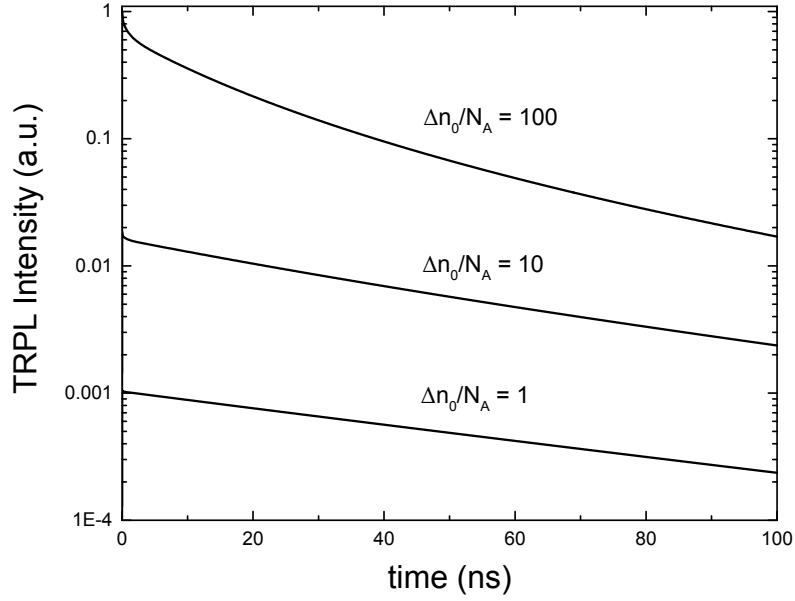


Figure 2.3: Photoluminescence decay of an ideal absorber after excitation with a laser pulse. Here only radiative recombination is considered and excitation is homogeneous over the volume of the absorber. Injection level is expressed as $\Delta n_0/N_A$.

pairs is much lower than the doping concentration of the absorber material $\Delta n_0 \ll N_A$. Since Δn_0 is the maximum value $n(t)$ can reach, then in this case it is also true that $n^2 \ll N_A n$. In total the equations for $n(t)$ and for the recombination rate can then be simplified as follows:

$$n(t) = \Delta n_0 \exp(-t/\tau_{rad}) \quad (2.31)$$

$$R_{rad}(t) = B_{rad} N_A n(t) \quad (2.32)$$

This is called the low injection case and is characterized by a radiative recombination that can be described as a single exponential decay. For cases of higher injection where the assumption $\Delta n_0 \ll N_A$ is no longer valid, the full form of Eq. (2.27) and (2.29) must be used.

At this point the injection level will be defined for the rest of this work as the quotient $\Delta n_0/N_A$. In Fig. 2.3 the influence of the injection level on the photoluminescence decay is exemplified for an ideal absorber. At low injection a simple exponential decay can be observed. At higher intensities the n^2 term in Eq. (2.28) becomes larger and the shape of the decay curve at times $t < \tau_{rad}$ is changed.

Finally, it is relevant to keep in mind that non-radiative recombination of charge carriers over defect states affects the measured photoluminescence lifetime, as the radiative recombination rate depends on the concentration of carriers n (Eq. (2.27)), which itself is affected by all recombination mechanisms. Therefore it is important to consider all channels for recombination, as they play an important role in the measurement and interpretation of TRPL.

Shockley-Read-Hall recombination

Recombination over deep defect states inside the band gap is most commonly described by the model of Shockley, Read and Hall [18, 19]. This is one of the most relevant mechanisms of efficiency loss in CIGS solar cells. These defects arise from crystallographic imperfections or chemical impurities [20, 21].

The recombination rate at these defects R_{SRH} is defined with following equation:

$$R_{SRH} = \frac{np - n_i^2}{\tau_p(n + n_t) + \tau_n(p + p_t)} \quad (2.33)$$

Here n_i is the intrinsic charge carrier density defined in Eq. (2.12), while $\tau_{n,p}$ are the SRH recombination lifetimes of electrons and holes respectively. They depend on the capture cross sections of the defect states $\sigma_{n,p}$ for electrons and holes, on the respective thermal velocities $v_{th,n,p}$ and on the density of defects N_t .

$$\tau_{n,p} = \frac{1}{\sigma_{n,p}v_{th,n,p}N_t} \quad (2.34)$$

The densities n_t and p_t correspond to the density of charge carriers that occupy trap states with energy E_T in equilibrium and are given by the expressions:

$$n_t = n_i \exp\left(\frac{E_T - E_{F,i}}{kT}\right) \quad (2.35)$$

$$p_t = n_i \exp\left(-\frac{E_T - E_{F,i}}{kT}\right) \quad (2.36)$$

Here $E_{F,i}$ is the intrinsic Fermi level defined in Eq. (2.13).

When considering Fermi statistics, as described in section 2.1.2, the recombination rate must be corrected with the factors $\gamma_{n,p}$ as given in Eq. (2.8):

$$R_{SRH} = \frac{np - \gamma_n\gamma_p n_i^2}{\tau_p(n + \gamma_n n_t) + \tau_n(p + \gamma_p p_t)} \quad (2.37)$$

Interface recombination

Interface recombination refers to the recombination over defects at the interfaces between the layers of the solar cell. This type of defects arises from crystallographic imperfections since at the surface of a crystal, the lattice symmetry is interrupted and atoms with not fully paired valence electrons are left. As the valence electrons change their energetic states, defect states within the band gap emerge [22, 23]. Impurities and the diffusion of elements from one layer to the other

create further defects at the interfaces [24]. Furthermore higher recombination can also take place at the interface between grain boundaries in the polycrystalline CIGS material, where impurities accumulate and elements of the material are redistributed [25].

The rate for this type of recombination follows the same basic structure of the SRH recombination, but here the lifetimes are replaced with recombination velocities S_n and S_p for electrons and holes respectively, while $n_{t,s}$ and $p_{t,s}$ describe the density of charge carriers trapped in surface defects, analogue to Eq. (2.35) and (2.36) [17].

$$R_{Surf} = \frac{np - n_i^2}{S_p^{-1}(n + n_{t,s}) + S_n^{-1}(p + p_{t,s})} \quad (2.38)$$

2.1.5 Device structure

The thin film solar cells investigated in this work come from an in-line production and have all been provided by an industry partner. These samples use a device structure like the one shown in Fig. 2.4. The details of production can be found in Ref. [26]. The cells have been deposited on a soda lime float glass which has been coated with a molybdenum back contact. The CIGSe absorber layer has been produced by co-evaporation of the elements Cu, In, Ga and Se. A CdS buffer layer is deposited on top of the absorber via chemical bath deposition. An intrinsic ZnO (i-ZnO) layer is deposited by radio frequency sputtering and a final layer of aluminum-doped ZnO (ZnO:Al) is deposited by DC sputtering. The investigated samples lack any monolithic structuring and have not been encapsulated.

The molybdenum back contact serves as a conductive electrode, which allows the lateral collection of current from the back side. The formation of a MoSe₂ layer between absorber and back contact is an important topic of research, as such a layer can act as a barrier for current extraction and can have a significant impact on solar cell efficiency [27–31].

Sulfur is not present in the studied absorber layers, which represents a special case of the more general Cu(In,Ga)(S,Se)₂ material [9, 11]. The CIGS and CIGSe materials are direct band gap semiconductors and have p-type conductivity. The CIGSe absorber is grown to a depth of approximately 2 μm . The excess of holes comes from native crystal defects. Acceptor type copper vacancies are regarded as the main source of p-doping [32]. By controlling the $[\text{Ga}]/([\text{Ga}] + [\text{In}])$ ratio the band gap of the material can be tuned. This ratio is an important parameter for this work and will be abbreviated as “GGI”. Changing the gallium content specifically alters the conduction band edge E_C [33]. In the investigated samples this property is used to enhance the electric field by producing the absorber with a constant increase of the GGI towards the back contact, driving excited electrons towards the p-n junction and hindering their diffusion into the volume of the absorber. This has an overall positive effect on the open circuit voltage of the solar cells. The GGI gradient has been characterized by Heise et al. [11] and has been found to be linearly dependent on the depth of the absorber, with $\text{GGI} = 0.2$ at the front surface of the CIGS absorber and 0.5 at the back side.

i-ZnO/n-ZnO	0.25 – 1 μm
Buffer	50 nm
Cu(In,Ga)(S,Se) ₂	1 – 3 μm
Mo	0.5 – 1 μm
Glass, metal, polymer	

Figure 2.4: From [32]. Basic schematic of the structure of a CIGS solar cell.

The CdS buffer layer is an n-type semiconductor with a much larger band gap than the CIGSe, which reduces the parasitic absorption of photons. It is one of the n partners for the p absorber to build a p-n junction. One further purpose of the CdS is the passivation of the surface of the CIGSe absorber.

The ZnO:Al and i-ZnO layers also have n-type conductivity, with a much higher carrier concentration than the CIGSe absorber. The band gaps of these two materials are much larger than those of CdS or CIGSe, avoiding any significant optical absorption. While the electrical resistivity of the i-ZnO is high, which is detrimental for the cell, it has also been found to be necessary for reproducibility in the production of this type of cells, probably because this layer prevents shunting [34, 35]. The doped ZnO:Al layer on the other hand has very high conductivity thanks to the very high charge carrier concentration. It is an excellent transparent conductive material and is used for lateral collection of current from the front contact of the cell without any significant ohmic losses.

2.1.6 Metastability

CIGS solar cells show a metastable behavior under light exposure, by which the open circuit voltage is increased [36]. The conditioning of the material is a reversible process that changes the charge state of defects within the band gap [37]. Additionally a metastable behavior under voltage bias has also been identified [38], which is also reversible and is linked to the migration of copper ions driven by the electric field [39].

Heat treatment in the darkness is called “dark annealing”, from here on abbreviated as “DA”, while heat treatment under illumination is referred to as “light soaking”, or “LS”.

The change in the charge of defects induced by conditioning of the cell has an influence on multiple characteristics of the absorber. As explained in the model by Lany and Zunger [40], the most relevant defects contributing to this process are the copper vacancy V_{Cu} and the selenium vacancy V_{Se} , which build a divacancy complex $(V_{\text{Cu}}, V_{\text{Se}})$. This complex can take on three different charge states with different state energies, namely $(V_{\text{Cu}}, V_{\text{Se}})^+$, $(V_{\text{Cu}}, V_{\text{Se}})^-$ and $(V_{\text{Cu}}, V_{\text{Se}})^{3-}$. After optical excitation of a hole-electron pair the donor state $(V_{\text{Cu}}, V_{\text{Se}})^+$ can capture the excited electron and become $(V_{\text{Cu}}, V_{\text{Se}})^0$. From this state the lattice can relax via thermal treatment, reducing the distance between indium atoms and changing the defect from donor to acceptor. A second electron can be captured causing a transition to the state $(V_{\text{Cu}}, V_{\text{Se}})^-$. The net effect of this process is a change of the defects from positively charged donor to negatively charged acceptor, which results in an increase in the net p-type doping density of the material. Thus light soaking, again a treatment with heat under light bias, increases the doping of the material. The reverse reaction is thermally activated and requires the capture of two holes, while changing the defect from acceptor back to donor, reducing the p-type doping. This means that dark annealing reduces the doping of the material. This effect is used to tune the doping density of the investigated absorber material.

2.2 Time-resolved photoluminescence

In time-resolved photoluminescence (TRPL) just like in spectrally resolved photoluminescence, the investigated material is excited with a laser, changing the states of electrons and injecting them into the conduction band. For each absorbed photon a single electron hole pair is generated. After a short time, usually in the order of nanoseconds to microseconds, depending on the investigated semiconductor, electrons and holes recombine with each other in band to band transitions that release a photon with an energy corresponding to the band gap of the material. Deviations from this photon energy can result when charge carriers recombine over shallow defects, i.e. defects near the band edges. It is therefore possible to gain information about the band structure of the material and about the defect landscape by looking at the spectrum of the photons emitted. In TRPL however, the focus lays not in the spectral distribution of the emitted photons, but in their temporal distribution, i.e. the distribution of their times of emission. The information gained from the temporal distribution of photon emission corresponds to the recombination time of the charge carriers. Additionally, it is possible to combine the analysis of spectral and temporal distribution, as has been done by Kuciauskas et al. [41].

The measurement of time-resolved photoluminescence makes use of the fact that excited electron-hole pairs do not recombine instantaneously after the optical generation. In TRPL the measured quantity is the number of photons emitted by radiative recombination after the arrival of an excitation pulse, as a function of time. Moreover, the measured quantity is the radiative recombination rate integrated over the illuminated volume. During detection this quantity is reduced by a constant corresponding to the small solid angle of detection. Other losses can come from the optical components in the experimental setup.

As seen in the equations for the different recombination mechanisms (Eqs. (2.27), (2.37), (2.38)), the decay in the density of excited charge carriers is a function of time that generally depends on the

density of charge carriers itself and on a characteristic lifetime that is specific to each recombination mechanism ($\tau_{rad}, \tau_n, \tau_p$). The combination of all these effects gives rise to an effective charge carrier lifetime that can be described as a function of all recombination lifetimes.

By analyzing the shape of measured decay curves, determining how large the contribution of each recombination mechanism is and extracting values for the respective lifetimes, a great amount of physical information can be gained. This includes information about the density and position of defects within the layer or at interfaces, their capture cross sections and energy distributions. However, because of the large amount of information contained in a single TRPL decay curve, interpretation of a single curve can be ambiguous. The main problem for interpretation arises from the dependence of the radiative recombination rate R_{rad} on the density of charge carriers n . Since n is itself dependent on all the other recombination rates, writing the complete equation for $n(t)$ would result in an underdetermined equation, containing multiple variables in the form of $n, p, \tau_{rad}, \tau_n, \tau_p$. Therefore it is very important for TRPL investigations to carry out variations in the experimental conditions to create a system of equations that contains sufficient information to determine the interesting variables. By changing the experimental conditions, the set of parameter values that can solve all equations can be determined with higher confidence. This is true since the space of possible solutions for the system of equations is reduced rapidly by increasing the number of different experiments that the model should describe.

In this section the theory necessary to carry out discussions about TRPL decay curves is presented.

2.2.1 Injection Level

The injection level has been defined as the quotient of excited charge carriers and doping concentration ($\Delta n_0/N_A$). The value of the injection level, i.e. the initial conditions for the TRPL decay have been shown to have an influence on the time development of the PL emission.

The simplest idealized case will now be discussed as a basis on which all other more complex cases will build upon. This would correspond to a homogeneous absorber, which becomes homogeneously excited, i.e. having the same generation rate at every point in its volume, and containing no defects. Therefore the only possible recombination path for excited charge carriers is radiative band to band recombination. As presented in the previous section, the recombination rate is describe by Eq. (2.28) and the time evolution of the charge carrier density follows Eq. (2.29). In Fig. 2.3 it is shown how such a TRPL decay curve depends on the initially excited charge carrier density $\Delta n_0 \propto P_0$. Here a distinction is made between the case with $\Delta n_0 \ll N_A$ and all other cases. The former is called the low injection case and for it $n(t)$ can be simplified to take the form in Eq. (2.31).

For this simplified case the curve would look like a straight line in a half-logarithmic plot, i.e. $\log(n(t))$ vs. t . In this case τ_{rad} would correspond to the inverse of the slope. Such a decay curve is also usually called “monoexponential”.

In the cases of higher injection, for which $\Delta n_0 \ll N_A$ is no longer valid, the slope of the curve in the semi-logarithmic plot is dependent on time, starting at a value smaller than τ_{rad} , but converging toward τ_{rad} with time. This means that after some amount of time the “bimolecular” recombination, i.e. the term in Eq. (2.27) proportional to n^2 , becomes so small that the decay curve becomes basically monoexponential.

In summary, for an ideal, homogeneous absorber under homogeneous excitation, the radiative lifetime can be extracted from the inverse of the slope in the linear regime of the semi-logarithmic plot, or monoexponential regime, of the photoluminescence decay.

2.2.2 Contribution of defect states

Defect states can influence photoluminescence in two main ways. The first is serving as recombination centers, while the second way is by trapping charge carriers and releasing them at a later time to the energetic bands. In this section the influence of both mechanisms on the photoluminescence lifetime is discussed.

Defects as recombination centers

Ahrenkiel has presented a very thorough analysis of the contributions of recombination mechanisms to the overall photoluminescence lifetime [17]. As long as the injection level is kept low and the probabilities of recombination are additive, it is possible to generalize the lifetime of the decay. The second assumption is generally valid, since the recombination rates behave as velocities in the sense that they can be linearly added. Therefore in presence of multiple recombination mechanisms, each with recombination rate R_i , the differential equation for the density of charge carriers can be written as:

$$-\frac{dn(t)}{dt} = \sum_i R_i \quad (2.39)$$

An assumption must be made at this point, that every recombination rate can be simplified to take the following form, depending only on the charge carrier density and the corresponding lifetime τ_i :

$$R_i = \frac{n}{\tau_i} \quad (2.40)$$

Therefore:

$$-\frac{dn(t)}{dt} = \left(\sum_i \frac{1}{\tau_i} \right) n(t) \quad (2.41)$$

From this form the general photoluminescence lifetime is defined:

$$\frac{1}{\tau_{PL}} = \left(\sum_i \frac{1}{\tau_i} \right) \quad (2.42)$$

The solution to the differential equation is simple:

$$n(t) = \Delta n_0 \exp\left(-\frac{t}{\tau_{PL}}\right) \quad (2.43)$$

Since the relevant physical quantity for measurements is the rate of radiative recombination R_{rad} , it is interesting to take a look at it in dependence of all other recombination mechanisms. Here we keep the assumption of low injection:

$$R_{rad} = B_{rad} N_A n(t) = \frac{n(t)}{\tau_{rad}} = \frac{\Delta n_0}{\tau_{rad}} \exp\left(-\frac{t}{\tau_{PL}}\right) \quad (2.44)$$

To give an example for τ_{PL} in the investigated cells, for which Shockley-Read-Hall and surface or interface recombination are considered, we use τ_{SRH} as the Shockley-Read-Hall lifetime and τ_{Surf} as the surface or interface recombination lifetime, each still using the assumption in Eq. (2.40). The result is:

$$\frac{1}{\tau_{PL}} = \frac{1}{\tau_{rad}} + \frac{1}{\tau_{SRH}} + \frac{1}{\tau_{Surf}} \quad (2.45)$$

The simplification in Eq. (2.40) is not trivial, especially in the cases of SRH-like recombination. Here it is helpful to look at the recombination rate R_{SRH} from Eq. (2.37) and apply the simplification of low injection $\Delta n_0 \ll N_A$, which also means that $n \ll N_A$. Moreover we use the simplification of heavily doped material $n_0 \ll n$, which means $n = \Delta n$ and is generally valid for CIGSe. In this case it also holds true $p = N_A$. With these simplifications R_{SRH} becomes:

$$R_{SRH} \approx \frac{n N_A}{\tau_p n + \tau_n N_A} = \frac{N_A n}{N_A (\tau_p n N_A^{-1} + \tau_n)} \approx \frac{n}{\tau_n} \quad (2.46)$$

The right hand side of this equation is exactly in the necessary form. What can be seen here is that in low injection, the SRH lifetime of the minority charge carriers determine the entire SRH recombination lifetime.

The same simplification can be carried out for the surface recombination rate in Eq. (2.38), resulting in the surface recombination lifetime under low injection conditions being determined by the surface recombination velocity of minority charge carriers:

$$R_{Surf} \approx \frac{n N_A}{S_p^{-1} n + S_n^{-1} N_A} \approx \frac{n}{S_n^{-1}} \quad (2.47)$$

In summary, under low injection, even in the presence of radiative and non-radiative recombination, the photoluminescence curve will take a monoexponential shape, as seen in Eq. (2.43), with a lifetime τ_{PL} that is the inverse of the sum of the inverse lifetimes of all involved recombination mechanisms.

Defects as traps

If the defects states inside the band gap do not act purely as recombination centers, but also are considered to capture minority charge carriers and emit them back to the conduction band after a certain time, a new type of behavior arises. Maiberg et al. [42] have done an extensive theoretical analysis of this phenomenon. This section summarizes the results of their work.

The solution for the density of charge carriers $n(t)$ yields:

$$n(t) = -C_1 \exp\left(-\frac{t}{\tau_1}\right) + C_2 \exp\left(-\frac{t}{\tau_2}\right) \quad (2.48)$$

The constants C_1 and C_2 take a rather complex form, which will not be discussed here. They are dependent on the total recombination lifetime τ_n , the capture lifetime τ_c , the emission lifetime τ_e , the initial density of free charge carriers Δn_0 and the initial density of trapped carriers $n_{t,0}$. More details can be found in Ref. [42].

More interesting here are the lifetimes τ_1 and τ_2 . The decay curve resulting from Eq. (2.48) has a so called ‘‘biexponential’’ shape, meaning that there are two distinct terms, each with a monoexponential form. The first term is characterized by a short decay lifetime τ_1 and the second term contains a longer decay lifetime τ_2 .

If the capture rate is very slow compared to the recombination lifetime, then the entire equation becomes the monoexponential decay already seen in previous sections ($\tau_c \gg \tau_n$):

$$n(t) = \Delta n_0 \exp\left(-\frac{t}{\tau_n}\right) \quad (2.49)$$

In the other cases, the capture lifetime is similar to or smaller than the recombination lifetime. This means that most excited electrons become trapped quickly. The behavior then becomes mainly dependent on the emission lifetime. If the emission lifetime is much smaller than the other two, then the captured electrons are emitted in a very short time and recombine, again resulting in the monoexponential decay of Eq. (2.49) ($\tau_e \ll \tau_n, \tau_c$).

The most interesting case arises when all lifetimes are in a similar range. In the case of $\tau_e > \tau_c$ the electrons are trapped quickly and then slowly emitted back. Only then can they recombine. In this case τ_1 and τ_2 can be written as:

$$\frac{1}{\tau_1} = \frac{1}{\tau_n} + \frac{1}{\tau_c} + \frac{1}{\tau_e} \left(1 - \frac{\tau_c}{\tau_n}\right) \quad (2.50)$$

$$\frac{1}{\tau_2} = \frac{\tau_c}{\tau_e \tau_n} \quad (2.51)$$

In summary, if there are traps that can capture electrons and do not act as recombination centers, the decay takes a biexponential form. The longer the capture lifetime becomes, the closer the curve comes back to the monoexponential case, while for the emission lifetime the opposite is true. Such traps can usually exist only near to the conduction band edge, since otherwise they would be occupied already even in equilibrium and it would not be possible for electrons to become trapped. Recombination in these cases can happen over deeper defects closer to the band gap middle.

2.2.3 Inhomogeneities

The models described in the previous sections generally assume low injection and homogeneous generation of charge carriers over the volume of the absorber, as well as a material with very homogeneous characteristics. Experimental conditions, however, tend to break one or many of these assumptions. In this section models of describing TRPL decay which are closer to the experimental reality will be presented.

Generation profile and diffusion

With a laser pulse as the source of excitation, generation cannot be perfectly homogeneous over the volume of the absorber. Firstly, a laser pulse always presents a lateral profile with light intensity decaying with distance from the center of the beam. Secondly, absorption of photons in a semiconductor follows the Beer-Lambert law, making the density of excited electrons Δn_0 dependent on the depth x and on the wavelength-dependent absorption coefficient $\alpha(\lambda)$ of the material. The intensity of the light I as a function of depth behaves as following:

$$I(x) = I_0 \exp(-\alpha x) \quad (2.52)$$

The position dependent intensity profile creates a further disturbance in the system in the form of a concentration gradient. As described in Eqs. (2.14) and (2.15), a gradient in the densities of charge carriers results in a gradient in the Fermi energies. This then results in a redistribution of charge carriers due to a diffusion current, as resulting from Eqs. (2.24) and (2.25). Ahrenkiel [17] offers one of the most general models to describe the time decay of PL signals $I_{PL}(t)$ taking into account the Beer-Lambert profile of excitation with absorption coefficient α , surface recombination with recombination velocity S_n , diffusion of charge carriers with diffusion constant D_n (Eq. (2.26)), radiative recombination with radiative lifetime τ_{rad} and photoluminescence lifetime τ_{PL} as seen in Eq. (2.45).

$$I_{PL}(t) = \frac{I_0}{\tau_{rad}} \exp\left(-\frac{t}{\tau_{PL}}\right) \left\{ \frac{S_n}{S_n - \alpha D_n} \exp(\alpha^2 D_n t) \operatorname{erfc}(\alpha \sqrt{Dt}) - \frac{\alpha D_n}{S_n - \alpha D_n} \exp\left(\frac{S_n^2 t}{D_n}\right) \operatorname{erfc}\left(S_n \sqrt{\frac{t}{D_n}}\right) \right\} \quad (2.53)$$

Here I_0 is the initial PL signal intensity. The expression “erfc” represents the complementary error function defined as:

$$\operatorname{erfc}(z) = \frac{2}{\pi} \int_z^\infty \exp(-t'^2) dt' \quad (2.54)$$

In this case the slower the surface recombination becomes, the closer the curve converges towards the monoexponential case. Moreover, for very thin films or films with very high mobility, in which the diffusion length of the charge carriers is in the order of magnitude of the layer thickness, the function simplifies and becomes monoexponential as well.

p-n junction

When measuring TRPL at a p-n junction instead of in an isolated CIGS absorber, the bending of the energy bands in the space charge region creates a strong electric field. As shown in Eqs. (2.22) and (2.23) this gradient in the electrical potential results in a drift of excited electrons and holes in opposite directions. This so called “charge separation” has a direct effect on the rate of radiative recombination, as it is dependent on the local product of $n(x, t)$ and $p(x, t)$ at each position (Eq. (2.27)). As the distributions of charge carriers shift in opposite directions, their product at each position becomes smaller and therefore the radiative recombination decays very rapidly. Metzger et al. [43] have experimentally demonstrated this effect with ZnO/CdS/CIGS p-n junctions. They also report that removing the ZnO layer and leaving only a CdS/CIGS is enough to reduce the electric field to the point where this effect disappears.

Kuciauskas et al. [44] have implemented a biexponential approach to analyze the decay curves of CIGS samples, i.e. describing the curves via equations with the same form as Eq. (2.48). They have done their experiments on devices including a p-n junction and applying voltage bias, while also investigating the TRPL decay’s spectrum and the influence of the excitation wavelength. Their results show that from the two resulting lifetimes, τ_1 corresponds to the decay in the region directly at the interface. Here τ_{diff} represents a diffusion lifetime and τ_{th} a thermionic emission lifetime.

$$\frac{1}{\tau_1} = \frac{1}{\tau_{rad}} + \frac{1}{\tau_{surf}} + \frac{1}{\tau_{diff}} + \frac{1}{\tau_{th}} \quad (2.55)$$

The longer lifetime τ_2 describes the photoluminescence behavior in the space charge region using the expression proposed by Maiberg et al. [45, 46]:

$$\frac{1}{\tau_2} = \frac{1}{\tau_n} + \frac{1}{\tau_p} + \frac{q(\mu_p + \mu_n)}{4kT} E^2 \quad (2.56)$$

Here E is the applied electrical field, $\mu_{n,p}$ are the mobilities of electrons and holes, $\tau_{n,p}$ are the bulk lifetimes of electrons and holes, while τ_{rad} is the radiative recombination lifetime as seen in previous sections. For surface recombination lifetime the following expression can be used [47]:

$$\frac{1}{\tau_{surf}} = \alpha S \quad (2.57)$$

With α as the absorption coefficient and S as the surface recombination velocity.

Meanwhile the diffusion lifetime uses the form proposed by Ahrenkiel [17]:

$$\frac{1}{\tau_{diff}} = \frac{\pi^2 D_n}{4x_n^2} \quad (2.58)$$

Here D is the diffusion coefficient and x_n is the depth of the region in which light is absorbed.

As for the thermionic emission lifetime τ_{th} , it can be written using L_w as the width of the barrier, which in this case is the width of the CdS buffer layer, m_n as the effective mass of electrons and ΔE as the height of the barrier, i.e. the conduction band offset at the CdS/CIGS interface [48]:

$$\frac{1}{\tau_{th}} = \frac{1}{L_w} \sqrt{\frac{kT}{2\pi m_n}} \exp\left(-\frac{\Delta E}{kT}\right) \quad (2.59)$$

Composition gradient over depth

A further source of complexity in the PL emission of the investigated absorber are composition gradients. Specifically in CIGS it is common to produce the absorber with a gradient in the gallium content [49,50], as this produces a gradient in the energy of the conduction band edge while leaving the valence band edge mostly unchanged, thus increasing the band gap [51]. This characteristic of the CIGS layers gives rise to several effects. First the case of a continuous linear increase in the band gap, as the one seen in the samples investigated in this work [9,10,52] is considered. In such a material, the gradient in conduction band edge energy results in an electric force acting against the direction of diffusion of highly concentrated charge carriers at the surface of the absorber after excitation. Second, there are samples with a so called v-grading, i.e. an increase in gallium content towards both front and back contact. This configuration is commonly used in record efficiency devices [49,50]. In this case there is a complex dependence of the shape of TRPL decay curves both on the wavelength used for excitation as well as the wavelength used for detection of the PL signal. Kuciauskas et al. [41,44] have presented an extensive study on this topic. They have shown that the spectrum of the TRPL signal shifts over time, with the energy of peak PL emission changing toward the energy corresponding to the band gap minimum. Measuring TRPL at a photon

energy equal to the band gap minimum yields different results from the decay curves measured at higher photon energies. For photon energies higher than the band gap minimum, the PL signal is coming from regions with a strong drift of charge carriers towards the regions of lower electrical potential. Therefore the TRPL decay curve has a very fast initial decay with lifetime τ_1 that quickly transitions to a much slower longer decay with lifetime τ_2 . At photon energies close to the band gap minimum however, the contribution of the term containing τ_1 is reversed, i.e. the PL signal gets stronger with a short lifetime corresponding to τ_1 and after this initial increase the long decay lifetime τ_2 dominates. The contribution of the first decay is negative for the regions where charge carriers are drifting away, while it is positive at the region towards which the charge carriers are drifting.

Lateral inhomogeneities

Lateral inhomogeneities in the absorber and in the excitation profile can have an influence on TRPL as shown by Maiberg et al. [53]. In their work they investigate the effect of laser spots used for excitation in TRPL having a lateral dependence of the photon density, while assuming a two dimensional Gaussian curve for the distribution. It is then shown that for TRPL experiments in which the area of excitation as well as the area of detection are much larger than the grain size of the material, the lateral diffusion caused by the laterally inhomogeneous excitation has a negligible effect. In these cases the TRPL curves can be modeled to a high degree of agreement with the approximation of laterally homogeneous average excitation. Additionally, the results of such experiments are usually the average over the fluctuating characteristics of single grains inside the measured area. A much more careful approach must be taken for experiments in which either the excitation area or the detection area, or both, are in the order of or smaller than the grain size of CIGS, i.e. approximately 1 μm diameter [32]. In these cases, the diffusion, drift, trapping and recombination of charge carriers can be dominated by lateral inhomogeneities in band gap, electric potential, trap density, recombination lifetime, etc.

Summary

In summary, the large number of ways that a TRPL curve can be analyzed need to be considered. For the general purposes of the experiments carried out in this work the simplification of homogeneous excitation and low injection conditions is not useful, since the experiments can often be far away from these conditions. On the other hand, as the size of the laser spot used in experiments here is much larger than the crystal size of CIGSe, the consideration of lateral inhomogeneities can be omitted. Important effects on the TRPL decay arrive from composition gradient, generation profile, diffusion, influence of the p-n junction, thermionic emission, trapping, emission and recombination. All of these effects must be considered before assigning a value extracted from experimental data to the charge carrier lifetime. In the methods chapter it will be discussed how these issues are addressed.

3 Methods

In this chapter the tools for experiments, analysis and simulation will be presented. In the first section the TRPL experimental setup and the time-correlated single photon counting measurement technique will be described in detail. Experimental setups for other methods applied will also be explained. The second section presents the methods to extract information, e.g. PL lifetime values, from TRPL decay curves both in experiments and simulations. The third section features the details of the simulation model and the chosen computational tool. A list of material parameters is also provided.

3.1 Experimental setups

The main experimental method for this work is time-resolved photoluminescence. Therefore the details of this type of measurements and its experimental setup will be presented in most detail. Other measurements detailed here serve as a complement. These additional methods help characterize the investigated solar cells, extract material parameters for simulation and serve as further verification for the simulation model.

3.1.1 Time-resolved photoluminescence

The basic requirements for a TRPL experimental setup will be listed below. First, a source of photons for excitation of the sample is required. In this work the excitation is performed by a pulsed laser system. Second, the photons emitted by the sample via photoluminescence must be detected. Here this is achieved by photomultiplier tubes. Third, the number of detected photons must be resolved over their time of detection. This must be done with a time resolution high enough to gain significant information from the PL decay. Several techniques exist for this step. For this work the technique of time-correlated single photon counting (TCSPC) has been chosen.

Laser system

The laser system is the source of excitation light and is the first of several larger building blocks for the TRPL experimental setup. The basic requirements for the laser system are multiple. The photons of the laser must have an energy larger than the band gap of the investigated material. Moreover, the time in which the sample is illuminated must be several orders of magnitude shorter

than the time of PL signal decay of the sample. Therefore the light source must be periodically interrupted. Additionally, the time between the arrival of consecutive light pulses must be large when compared to the time of PL signal decay. In this section the necessary components to meet these requirements are presented.

The laser system consist of three basic components. These are a pump laser, a dye laser system driven by the pump laser and a cavity dumper for outcoupling of pulses towards the rest of the setup. Fig. 3.1 shows a schematic of the laser system.

The pump laser is a commercially available Nd:YAG laser system (Spectra Physics Vanguard 2000-HM532) [54]. It emits photons at 532 nm wavelength and has a pulse rate of 80 MHz. The pump laser is guided to the dye laser system to excite emission from the dye.

In the dye laser system (Spectra Physics 375) [55], a mechanical pump drives the flow of the dye solution. The dye has a short distance open jet in its cycle, after coming out of a nozzle as a laminar flow. At this position the pump laser hits the dye compound 4-Dicyanomethylene-2-methyl-6-p-dimethylaminostyryl-4H-pyran, also known as DCM. When excited it emits photons in the range between 595 nm and 690 nm [56]. With a wavelength selector located inside the laser resonance cavity and composed of a Fabry-Pérot interferometer, the wavelength can be tuned [55]. In this case the dye laser system has been tuned to emit at 650 nm, which corresponds to a photon energy of approximately 1.9 eV. This energy is higher than the band gap of CIGSe thin film absorbers, which ranges from approximately 1.0 eV to 1.7 eV [57].

The cavity dumper (Spectra Physics 344s) [58] serves two basic functions. It works to couple laser pulses out towards the rest of the setup. Additionally, it reduces the pulse rate of the output when compared to the original pulse rate of the pump laser. The cavity dumper is located inside the resonance cavity of the dye layer system. It replaces the opaque mirror used for output in more conventional laser systems. In the cavity dumper the output of the laser is achieved by guiding the pulse through a piezo-crystal. By changing the refraction index of the crystal via a sound wave, laser pulses inside the crystal are diffracted into a different path away from the resonator and towards the rest of the experimental setup. The output rate can be tuned by modulation of the sound wave. The pressure wave comes from a radio-frequency generator (Camac CD 5000 - RFGen) connected to a loudspeaker. This loudspeaker is in direct contact with the crystal. To synchronize the pulses from the pump laser with those of the cavity dumper, a trigger diode modulates the radio frequency generator. The trigger diode is coupled to the pump laser by a wave divider, which guides a small percentage of the laser power towards it. A control unit between the trigger diode and the radio frequency generator permits to decrease the pulse rate by a constant factor. A laser with synchronized pump laser and cavity dumper is called “synchronously pumped”. This method has the advantage of keeping the output pulses at the same temporal width of the pump laser [59]. For the pulse rate of the pump laser (80 MHz), the time between arrival of consecutive pulses is 12.5 ns. This would be well below the time of PL signal decay expected for CIGSe material, which lies between 0.2 ns and 250 ns [32, 43, 60–62]. Therefore the pulse rate is set to 2 MHz, giving the PL signal enough time to decay completely, before the next pulse arrives and PL emission starts again.

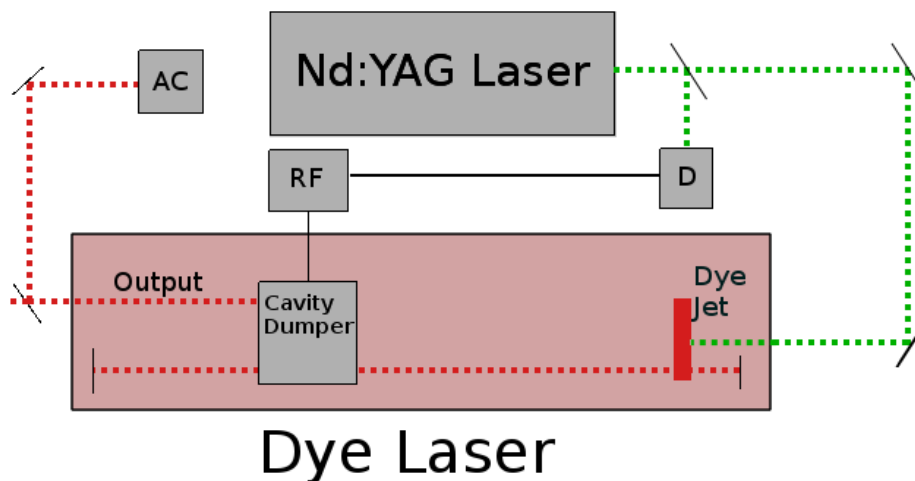


Figure 3.1: Schematic of the dye laser system including the Nd:YAG pumping laser. A sensor diode (D) controls the radio frequency generator (RF), which feeds into the cavity dumper. Part of the output power is guided to the autocorrelator (AC) for monitoring.

The shape of the pulses, i.e. their intensity over time, is monitored constantly by an autocorrelator. After exiting the laser cavity, a beam divider leads a fraction of the output power towards the autocorrelator (Spectra Physics, model 409) [63]. The pulses in this setup are approximated with a Gaussian curve and their full width half maximum (FWHM) was measured to be 7 ps [12].

There is an intrinsic power fluctuation to the mode-locked pump laser system and therefore to the overall output of the laser system as well. By measurement with a powermeter (Thorlabs S130C) over an integration time of 1 hour it was found that the power fluctuation is smaller than 3%. This range of stability allows to work with the simplification of constant average power. The error in the PL decay lifetime introduced here is negligible.

Photoluminescence emission and detection

After the laser pulse leaves the laser system via the cavity dumper, it is guided towards the investigated sample. The laser photons then excite charge carriers, which can recombine, with a portion of these carriers recombining radiatively and producing photoluminescence emission in the sample. The emission happens isometrically in all solid angles. An array of lenses focuses a fraction of the PL emission towards a monochromator. The monochromator serves to filter the signal to only detect wavelengths corresponding to the maximum of the PL emission spectrum of the samples, which was previously characterized. After the signal has been filtered, it is guided towards a photomultiplier, which then creates a voltage signal from the detected photons. This signal is captured and analyzed by electronic components and is then compiled into the final measurement data. Further details about each step of this processes are presented below.

The laser beam hits the sample at an angle of approximately 45° . Because of its angle of incidence, the laser spot has an elliptical shape. The diameter of the laser spot, defined here as the FWHM of the lateral intensity profile was measured with a beam profiler (DataRay WinCamD-UCD15). The

diameter was found to be 450 μm for the major elliptical axis and 250 μm for the minor axis. This is several orders of magnitude above the grain size in CIGS. Therefore the effect of lateral charge carrier diffusion due to inhomogeneous excitation can be neglected, as discussed in Section 2.2.3.

It is important for the measurement of TRPL to separate the dynamics of PL decay from the time dependence of generation. However, due to the finite spectral width of the laser pulse, it suffers from broadening as the photons with different wavelengths pass through the multiple optical components of the setup. If the width of the pulse is close to or even greater than the time of PL decay, it is then necessary to analyze the data by deconvoluting the signal to separate PL emission from the laser pulse [64]. To monitor this effect the broadening of the pulse was determined by measuring TRPL on a white reflector and detecting at the same wavelength of excitation. The detected pulse width (FWHM) was 200 ps, and thus much smaller than the PL decay times of the investigated samples. For this reason the deconvolution of laser pulse and TRPL signal is omitted in this work. This error arising from this simplification is negligible.

After emission from the sample, a fraction of the photons is collimated by a plano-convex lens. The collimated photons are then focused by a second plano-convex lens onto the entrance slit of a monochromator (Newport Cornerstone 260). Before entering the monochromator the signal goes through a longpass edge filter, which cuts out the wavelength of the excitation laser, thus avoiding false detection at the second order refraction wavelength, i.e. at the position of the monochromator grating corresponding to double the wavelength of excitation.

The photon detection is carried out by a peltier-cooled, near-infrared (NIR) sensitive photomultiplier tube (PMT) module (Hamamatsu H10330-75). This detector can be connected to a lock-in amplifier (Stanford Research Systems SR810) for spectral PL measurements or to a TCSPC module for TRPL measurement (Becker&Hickl, SPC150). Detection is done at the wavelength of maximum PL emission of the investigated CIGSe absorber (1050 nm). The spectral width of detection is determined by the width of the exit slit of the monochromator. Previous experiments [12] have found that with an exit slit width of 1 mm, the spectral resolution of detection is of around 10 nm. Additionally, the spectral width (FWHM) of the excitation laser pulse was measured to be approximately 10 nm. Since the previously mentioned monochromator was used to measure this and since the spectral width is in the same order of magnitude as the error coming from the monochromator, both uncertainties can be expected to influence one another and to result in a total spectral uncertainty of 10 nm. The error in photoluminescence decay from this 10 nm error range in detection is negligible. The slit width of 1 mm was chosen as a balance between spectral resolution and signal amplitude. A slit width much smaller than 1 mm would result in a signal too weak when compared to the noise level, especially in conditions of very low excitation power. A slit width much larger than 1mm on the other hand would result in a spectral uncertainty leading to a false interpretation of the data. Therefore the slit widths for measurement stay in a similar order of magnitude (0.5-2 mm).

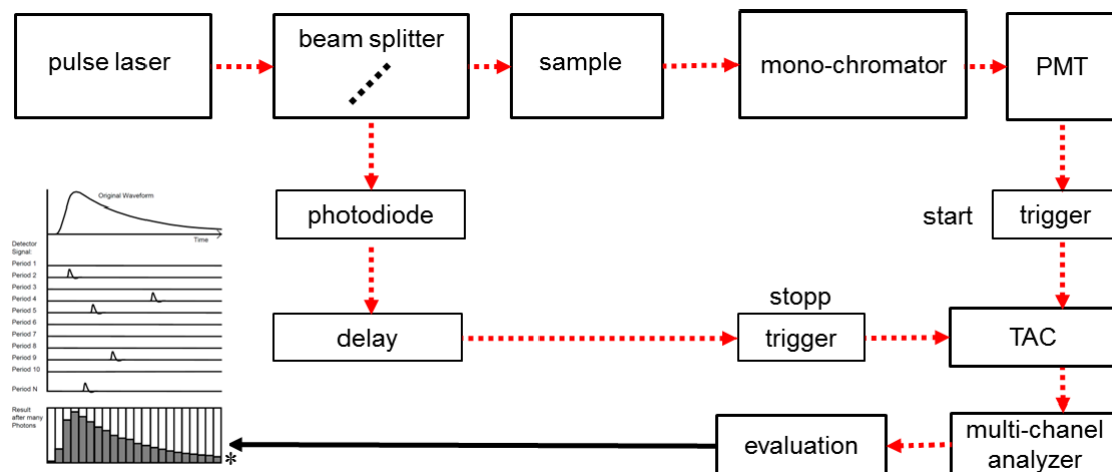


Fig. 3.2: From [12], [64]. Schematic of the experimental setup for measurement of time-resolved photoluminescence via time-correlated single photon counting.

Time-correlated single photon counting

The method of detection for time-resolved photoluminescence applied here is time-correlated single photon counting. This is a highly sensitive technique in which single photons of a periodic signal are detected, while the time difference between a reference signal and the time of detection of these photons is measured. With it time resolutions in the order of magnitude of picoseconds can be achieved [64]. The basic structure of the measurement setup for TCSPC is shown in Fig. 3.2 and further details can be found in Ref. [64]. The main outline of this method will be presented here.

The principle behind TCSPC is considering the detection of photons during the photoluminescence decay as a random process. The probability of single photon detection at each point in time is assumed to be directly proportional to the intensity of the overall PL signal at that same time. By plotting the distribution of the detected photons versus their time of arrival at the detector, the shape of the signal can then be reconstructed. By repeating the cycle of excitation and emission, e.g. with a pulsed laser, it becomes possible to gather data over times several orders of magnitude longer than the time of decay of the PL signal.

The time of detection of photons at the photomultiplier (PMT) is measured with the help of a time-to-amplitude converter or TAC. The TAC takes a start and a stop signal from two different detectors as triggers and converts the time difference between these signals into a voltage value that can be worked with by further electronic components. The stop signal comes periodically from the excitation laser, which hits the stop diode after passing through a beam splitter. The start signal comes from detections at the photomultiplier, which do not happen in every excitation cycle. If a detection happens, the time value from the TAC is assigned to a time bin in a histogram by the electronics. For each detection, one entry is added to the corresponding bin. After numerous repetitions of the cycle, the histogram takes the form of the PL decay signal. This type of array is called a “reversed start-stop configuration” (Fig. 3.2). This means that only actual detections at the photomultiplier are considered as start signals for the TAC. One further point to consider

is that the signal of the stop trigger must be delayed before reaching the TAC, so it is received by the TAC after the start signal. This delay must be chosen so that an entire decay curve can be measured but it also must be smaller than the time between pulses so the cycles of detection do not overlap. Moreover the time between start and stop must be subtracted from the delay to get the time of arrival of the photon.

3.1.2 Electrical characterization

Further experimental methods help characterize the samples at an electrical level. These methods will be presented here shortly. In some cases the measurements were done to provide additional data, and to serve as a method of verification of the simulation model. Examples of this are measurements of current-voltage characteristics and quantum efficiency spectra. In other cases the main goal of the measurement is the extraction of a material parameter for use in the simulation model.

From current-voltage characteristics (IV) the photovoltaic efficiency of the samples can be analyzed. Further results from this measurement are the extraction of the short circuit current density (J_{SC}) and the open circuit voltage (V_{OC}). IV measurements were carried out at 25 °C. The temperature of the sample was held constant by a water-cooled stage and monitored via a thermal sensor placed on top of a dummy cell next to the investigated sample. The dummy cell is also a CIGS sample on a glass substrate of the same thickness. The solar spectrum of AM1.5g was closely approximated by a solar simulator (Photo Emission Tech SS100AAA). The adjustment of the light intensity was carried out by tuning the measured J_{SC} to the one extracted from quantum efficiency measurements (see below) and corresponding to the light intensity of 1000 W/m² in the case of a perfect solar spectrum. The collection and measurement of the current is done via a 4-point geometry, i.e. four metallic probe heads contacting the sample. Voltage source and current detector are united into a single source measurement unit (Keithley 2400). Two probe heads provide the voltage source and two probe heads parallel to the other two are connected to the current detector. This is done as to minimize the effect of external resistances on the measured current, e.g. those of cables and measurement equipment [65].

Quantum efficiency is defined as the ratio of electron-hole pairs extracted as electric current from the sample and the number of photons shining on it. This ratio is usually measured as a function of the excitation wavelength. The measurement of external quantum efficiency spectrum (EQE) can give insight into the spectral response of the sample. From this spectrum the theoretical value of J_{SC} for a AM1.5g spectrum at exactly 1000 W/m² can be calculated [66], which is then taken as the reference to adjust the light intensity in IV measurements. For this calculation, the spectrum of the actual illumination source in IV measurements, which can vary slightly from the AM1.5g standard, was taken into account.

In the EQE setup the amplitude of the electrical current extracted at each wavelength must be divided by the number of incoming photons at that same wavelength. The setup consists of a chopped light source to excite the charge carriers, a monochromator to select the wavelength

of excitation, a current collector to extract the electric current from the sample and a lock-in-amplifier to filter the noise out and to obtain results from the weak current signal coming from monochromatic excitation. The light source contains a xenon lamp and a quartz halogen lamp combined into a module (Bentham ILD-XE-QH). The output light is fed into a monochromator (Bentham TMc300) and the monochromatic light is guided onto a sample after being periodically modulated. The modulated monochromatic signal creates a very small current in the sample due to its narrow spectral width. This signal is amplified by a lock-in amplifier (Stanford Research Systems SR830). This provides access to the number of extracted electrons. Two calibration cells, one made of silicon (Bentham DH_Si) and one made of germanium (Bentham DH_Ge) allow to determine the intensity of the emission spectrum of the lamps and therefore gain access to the number of photons reaching the sample at each wavelength. With these data, the quantum efficiency at each wavelength can be calculated. No additional light bias was present during the measurements and these were done at room temperature with no temperature control.

For capacitance-voltage (CV) measurements, which permit to extract the values of the doping density of CIGS, were done with an impedance/gain-phase analyzer module (Hewlett Packard 4194A). The equivalent circuit of the solar cell assumed for this measurement is composed of a capacitor and a resistance in parallel, representing the space charge region of the solar cell. By applying an alternating voltage on the p-n junction and evaluating the phase shift of the detected current relative to the input voltage, the capacitance can be calculated according to the chosen equivalent circuit [67]. By then changing the amplitude of the applied voltage, the density of charge carriers, and thus the density of doping can be evaluated [67]. To avoid the influence of defects on the measurement, a capacitance-frequency analysis is first carried out. It must be guaranteed that the frequency of the alternating voltage is much higher than the response time of defects, so these do not have enough time to charge themselves and disturb the measurement by changing the density of carriers. Measurements of CV were done at room temperature, in dark conditions and at a voltage frequency of 100 kHz.

3.2 Lifetime extraction

A critical aspect of the evaluation of TRPL data is the extraction of the PL lifetime values. One of the most common methods of achieving this is by fitting the measured curves with monoexponential, biexponential or multi-exponential decay models [11, 60, 62, 68]. As discussed in Section 2.2, all of these lifetime models assume either low injection conditions or homogeneous generation over the depth of the absorber. However these two generalizations are seldom met in experiments or simulations carried out for this work. As a consequence, a more general model for lifetime extraction, one that is also valid under high injection conditions, is necessary.

Instantaneous lifetime

Ahrenkiel presents a very general method of lifetime extraction [17] by introducing the concept of an effective lifetime, from here on also called the “instantaneous lifetime” τ_{inst} . It is defined at

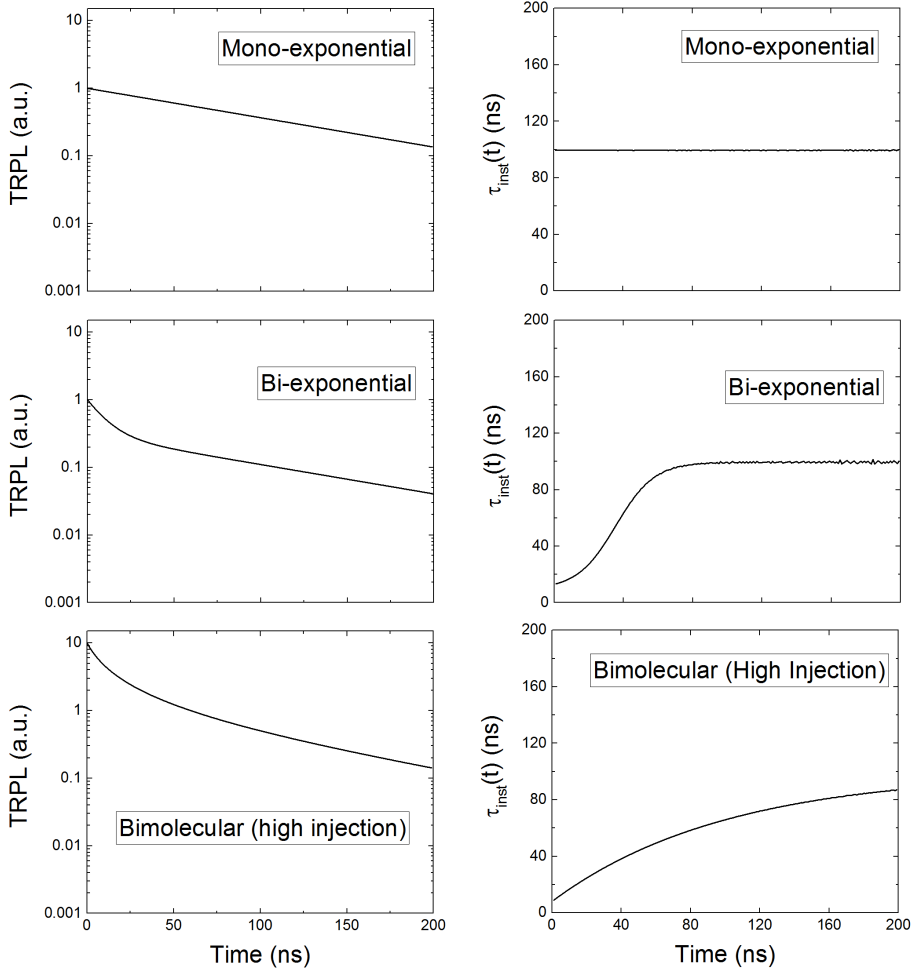


Figure 3.3: Left side: calculated TRPL curves. Right side: corresponding instantaneous lifetimes $\tau_{inst}(t)$ as a function of time for monoexponential (upper row), biexponential (middle row) and bimolecular (lower row) decay models.

each time value as a function of the PL intensity $I_{PL}(t)$ and its derivative over time:

$$\tau_{inst}(t) = \left(-\frac{1}{I_{PL}(t)} \frac{dI_{PL}(t)}{dt} \right)^{-1} \quad (3.1)$$

As in other analytical models for lifetime extraction, this equation relates the slope of the curve to the decay lifetime. In this case the slope is divided by the absolute value of the curve. In contrast to other methods, the definition of the instantaneous lifetime takes into consideration that the slope of the decay can change continuously over time during PL decay. In general, the instantaneous lifetime takes its minimum value at $t = 0$ and grows continuously. For monoexponential decays (Eq. 2.31), the value of τ_{inst} is constant. In a biexponential case (Eq. 2.48) there are two nearly constant regimes in the graph of $\tau_{inst}(t)$, corresponding to the two lifetimes in the model τ_1 and τ_2 . Between these two regimes there is a step. In a bimolecular decay curve (Eq. 2.29), τ_{inst} converges over time towards a maximum, from here on called the “asymptotic lifetime” τ_∞ (Eq. 3.2). Fig. 3.3 shows examples of monoexponential, bimolecular and biexponential decay curves and their respective time evolution of the instantaneous lifetime.

The asymptotic lifetime can be defined as the limit towards which τ_{inst} converges over time.

$$\tau_{\infty} = \lim_{t \rightarrow \infty} [\tau_{inst}(t)] \quad (3.2)$$

For ideal cases (homogeneous excitation over depth, no p-n junction and no defect recombination) the value of τ_{∞} corresponds to the pure low injection radiative lifetime τ_{rad} (Eq. 2.30). For less ideal cases the early part of TRPL decay curves can be strongly influenced by effects such as charge separation, diffusion and bimolecular recombination. These effects are largely relevant for time-resolved measurements but play no significant role in the measurement of device performance. On the other hand, in the presence of defect recombination, the asymptotic lifetime is influenced strongly by the trapping, emission and defect recombination lifetimes. These are all effects closely related to the solar cell efficiency [69, 70]. For this reason, the instantaneous lifetime becomes an important tool to investigate the dynamics of TRPL decay, since it describes the actual charge carrier recombination lifetime if the measurement time is sufficiently long. Thus, the asymptotic lifetime is a strong candidate for a fitting PL lifetime value to correlate with the device efficiency [10], which will be an important factor in the investigations presented in later sections.

3.3 Simulation

The interpretation of TRPL measurements is a complex problem with many more variables than what could be determined from a single measurement. While the variation of sample characteristics and experimental conditions helps providing a larger set of equations to extract more meaningful information, many variables remain unknown. In some cases this is because they are not experimentally measurable, while inevitably each variation introduces new variables. Simulations can help verify some of the assumptions made during the interpretation of experimental data by testing them with concrete physical models. They are an important tool in understanding the influence of specific material properties on TRPL measurements and on device performance. In this work the simulations are performed via the finite element method. The key equations for the simulation to solve are the Poisson and continuity equations, which give access to the electric potentials and the charge carrier concentrations. Details about the simulation tool are included below.

In this section, a short motivation for the choice of Sentaurus TCAD [71] as the simulation tool will be given. After that the characteristics of the simulation model will be presented. This includes the physical models taken into account, possible simplifications and assumptions that had to be made and a detailed list of parameter values. A basic description of how the simulation tool works is also included.

3.3.1 Introduction to the simulation tool

The simulation tool required for this work must be able to describe the time-dependent PL behavior of bare absorber layers while also being able to reproduce the data from quasi-stationary

IV and EQE measurements performed on entire devices. From the many freely and commercially available tools, only few satisfy all these requirements. Here a list of well-known tools for simulation of semiconductor devices is presented. By analyzing their strengths and weaknesses it can be recognized which are best suited for the goals of this work.

To categorize the simulation tools it is useful to look at their capacities of carrying out quasistationary or transient calculations. For the definitions of transient and quasistationary models see section 3.3.2. One of the most well-known and widespread tools is the freely available SCAPS-1D (Solar Cell Capacitance Simulator) by M. Burgelman from the University of Gent [72]. This tool allows quasistationary optoelectrical simulations in a quick and flexible manner for 1-dimensional models of layer stacks. Other freely available simulation tools are SC-Simul by the research group GRECO of the University of Oldenburg, R. Brüggemann [73], AMPS-1D (Analysis of Microelectronic and Photonic Structures) developed at the Pennsylvania State University by S. Fonash et al. [74] and AFORS-HET (Automat FOR Simulation of HETerostructures) developed by R. Varache et al. at the Helmholtz Zentrum Berlin [75].

The most common tool for simulation studies of time-resolved photoluminescence is the commercially available program Sentaurus TCAD (Technology Computer Aided Design) [42, 45, 46, 76, 77], developed by Synopsys [71]. The free applications named previously have the limitations of working only with one-dimensional models, while focusing mainly on quasistationary simulations. AFORS-HET, while being free, also has the capability of doing simulations of transient measurement methods, including photo-electroluminescence, in a 1-D environment. With Sentaurus TCAD it is possible to simulate in one, two or three dimensions, while having access to quasistationary and transient calculations. Another advantage of Sentaurus TCAD over the other options is the possibility of working with pulsed light sources. Both the consideration of transient calculations and the use of pulsed light sources for the excitation are essential for the proper calculation of time-dependent radiative recombination. For these reasons, Sentaurus TCAD was chosen as the tool for simulation. Most of the development of the model was carried out with the program version J-2014.09 [78]. The results presented in chapter 4 were calculated using version L-2016.03 [79].

3.3.2 Simulation model

The simulation model presented in this work builds upon the previous work by Heise et al. [11], Keller [80] and Richter et al. [81–84]. In order to simulate TRPL, a transient simulation was implemented in addition to the already existing quasistationary simulations. A list of material parameters is given in section 3.3.3. The most important characteristics of the model are listed:

- **Layer stack:** The simulated layer stack is the standard ZnO:Al/i-ZnO/CdS/CIGSe configuration for CIGSe thin film cells, as it is the one corresponding to the investigated cells [11]. For TRPL simulations either CdS/CIGSe junctions or bare CIGSe absorbers are simulated.
- **One dimensional:** The equations are all solved along a single axis, which is perpendicular to the surfaces of the layers and parallel to the propagation of light. Similarly only the component of the current that is parallel to the simulation axis is calculated. Moreover, the composition

of the layers as well as the intensity of light are assumed to be laterally homogeneous, so no force is driving a current in any direction other than that of the simulation axis.

- **Composition grading:** Along the depth axis, a gradient in the gallium content of the CIGSe absorber was implemented, corresponding to the one detected in Ref. [11].
- **Front and back contact:** The boundaries at the upper and lower surfaces of the layer stack are ideal metallic contacts. The possible formation of Schottky barriers between metal and semiconductor at these interfaces was not taken into account.
- **Boundary conditions:** The lateral boundaries of the simulation are assumed as ideal Neumann boundary conditions. As a result, no current density flows through the lateral boundaries and the electrostatic potential at the boundaries, as well as its derivative, are continuous [79].
- **Circuit:** Sentaurus TCAD uses a method of calculation for the output current of the devices called a “mixed-mode system”. This means that first the physical simulations regarding semiconductor physics and any other physical models are performed for the defined layer stack. This layer stack is then connected as a single component into an electrical circuit to carry out the necessary experiments. This circuit can be complemented with any number of additional classical electric components such as resistances, capacitors, voltage sources, etc.
- **Circuit conditions:** A voltage value between the front and back contact of the layer stack can be defined. For TRPL simulations this value was held constant at zero. A very large resistance ($>10^{10} \Omega$) was added in series to the circuit as the only other component to simulate the open circuit conditions of TRPL measurements. For IV and EQE measurements the resistance is set to the measured value of the series resistances from current-voltage characteristics. In IV simulations the voltage is changed step-wise over the measurement range. In EQE simulations the voltage is held at zero, while the wavelength is changed.
- **Meshing:** As part of the so-called “finite element method”, Sentaurus TCAD as well as most other simulation tools, divides the simulated space into discrete points. The program then solves the equations required at each of those points. The definition of the point grid throughout the space is called “meshing”. In the case of 1-D simulations these points lie all on the same axis. However, the distance between the points is not constant. A simple function creates the grid using a minimum step size of 1 nm at each boundary of the layer and increasing the step size by a constant factor over each new step until it reaches a maximum step size of 70 nm towards the middle of the layer. Using this definition, the mesh is finest towards the interfaces, where the gradients of the carrier concentrations are strongest due to recombination and transport.
- **Time resolution:** As with the spatial resolution, the temporal resolution is not constant. It is defined to be finer when the largest time derivatives are found, i.e. when the laser pulse reaches the sample. For the duration of the pulse the temporal resolution is set to the order of magnitude of 1 ps. For times long after the pulse (>10 ns) the time step increases to 0.1 ns.

- **Temperature:** All simulations were carried out at a fixed temperature of 300 K.

Quasistationary and transient calculations

Two different types of simulation have been distinguished so far. Here a basic definition for both types, quasistationary and transient, is provided.

In quasistationary simulations the numerical solution of each equation is repeatedly calculated until equilibrium is reached. This step is repeated for each of the different conditions simulated for the experiment. For example, in IV calculations this happens individually at every voltage value and in EQE simulations at each excitation wavelength.

In transient simulations there is a time component which is relevant to the simulated experiment. This means that the solutions to each equation are calculated for a number of time steps. These calculations must consider the time derivatives of physical quantities such as the charge carrier concentration and current density. This means that in transient calculations the solution of the previous time step is taken as the initial condition for the following time step. In other words, the system is not necessarily in equilibrium. This also means that the initial conditions have a large influence on the calculated solutions. One clear example of this effect is the influence of the injection level in TRPL simulations. For different injection levels, i.e. different densities of charge carriers initially excited, the TRPL decay behaves differently.

Optical model

The propagation of light within the layer stack is calculated with a simplified model called “Optbeam”. This method only takes reflection at the top of the layer stack into account, while neglecting reflection at interfaces within the layer stack. To reduce the error introduced by this method, the reflection at the uppermost layer of the stack (ZnO:Al) is not set to that of real isolated ZnO:Al but instead to the measured reflection of the entire layer stack. Thus, the light intensity entering the device $I_{0,int}$ is calculated as follows:

$$I_{0,int}(\lambda) = I_0(\lambda) [1 - R(\lambda)] \quad (3.3)$$

Here $R(\lambda)$ is the wavelength dependent reflection as defined in Eq. (2.19) and $I_0(\lambda)$ is the light intensity reaching the surface of the device from the outside. The absorption and hence the charge carrier generation over the depth of the layer stack is calculated according to Beer-Lambert law as seen in Eq. (2.18). This is a function of the absorption coefficient $\alpha(\lambda)$. Both $R(\lambda)$ and $\alpha(\lambda)$ are dependent on the components of the complex refractive index $\mathbf{n}(\lambda)$, which is defined as follows:

$$\mathbf{n}(\lambda) = n(\lambda) + ik(\lambda) \quad (3.4)$$

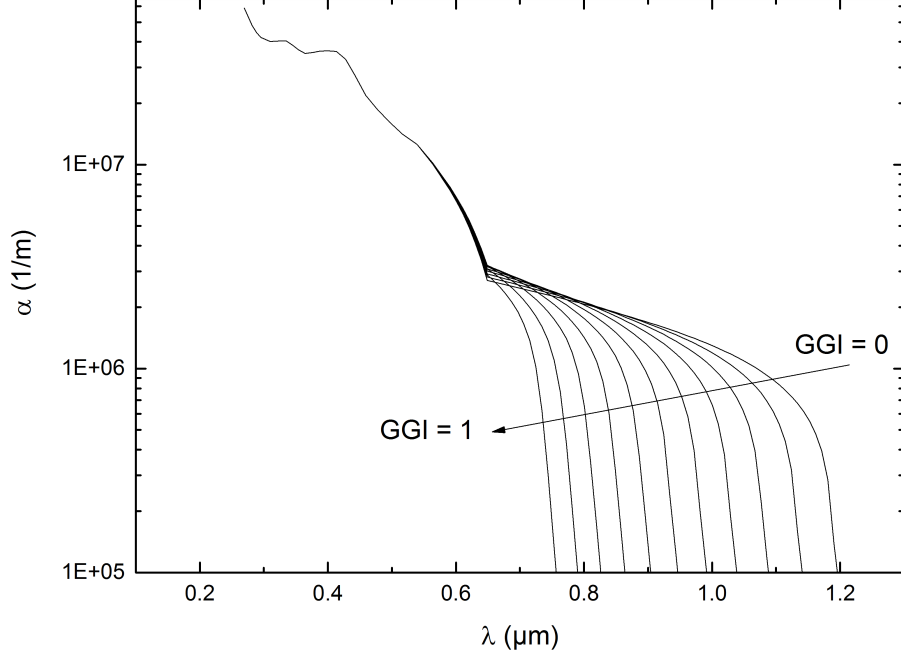


Figure 3.4: CIGSe absorption coefficient for GGI between 0 and 1 in equidistant 0.1 steps.

The real component $n(\lambda)$ goes into $R(\lambda)$ (Eq. (2.19)), while $\alpha(\lambda)$ can be calculated from the imaginary component $k(\lambda)$:

$$\alpha(\lambda) = \frac{4\pi k(\lambda)}{\lambda} \quad (3.5)$$

In Sentaurus TCAD the optical parameters for each material are given in terms of $n(\lambda)$ and $k(\lambda)$. While the real component of the layers below ZnO:Al are neglected in the Optbeam optical model, their imaginary component is relevant for the absorption. The three n-type layers ZnO:Al, i-ZnO and CdS have a step-like function in $k(\lambda)$, with a change of several orders of magnitude in the absorption around the wavelength of photons with energy corresponding to the respective band gap. For the CIGSe absorber the optical constants are taken from Paulson et al. [85] in the range $\lambda < 650$ nm. For longer wavelengths Ref. [11] calculates the absorption coefficient as follows:

$$\alpha = A_{direct} \sqrt{(\hbar\omega - E_g) / \hbar\omega} \quad (3.6)$$

Here \hbar is the reduced Planck constant and $\omega = 2\pi c/\lambda$ is the angular frequency of photons. The constant A_{direct} describes the direct band to band transition via absorption. Its value is set to $2.9 \cdot 10^4 \text{ cm}^{-1}$ for CIGSe and $6.5 \cdot 10^4 \text{ cm}^{-1}$ for CGSe, which is interpolated for intermediate compositions. This absorption spectrum is complemented with the addition of absorption via tail states near the band edges, also called Urbach tails [86].

$$\alpha = A_U \exp((\hbar\omega - E_g) / E_U) \quad (3.7)$$

3 Methods

The Urbach prefactor is set to $A_U = 3 \cdot 10^3 \text{ cm}^{-1}$ and the Urbach characteristic energy to $E_U = 25 \text{ meV}$. The optical constants of each layer are presented in Appendix A. Figure 3.4 shows the resulting absorption coefficient of the CIGSe layers with different compositions. This is plotted as a function of wavelength and the $[\text{Ga}]/([\text{Ga}] + [\text{In}])$ -ratio (GGI).

The intensity time profile of the laser pulse $I(t)$ was approximated by a Gaussian curve with I_{max} as the maximum intensity, t_S as the standard deviation of the time profile and t_0 as the time of maximum intensity. To simulate the experiment conditions as closely as possible, I_{max} was calculated as a function of the average laser power P_{Laser} used in experiments, while t_S was calculated from the measured FWHM time of the pulse $t_{FWHM} = 7 \text{ ps}$ [12]. In simulations the intensity of the laser pulse is assumed to be laterally homogeneous. Its maximum value is calculated from experimental data as the average intensity of a pulse with a Gaussian shape. For this, the standard deviation is calculated from the experimentally measured FWHM $D_{FWHM} = 460 \text{ }\mu\text{m}$. As discussed in section 2.2.3, the width of the laser spot is several orders of magnitude larger than the grain size in CIGSe. Therefore this approximation does not introduce any significant error.

$$I(t) = I_{max} \exp\left(-\left(\frac{t-t_0}{t_S}\right)^2\right) \quad (3.8)$$

$$t_S = \frac{t_{FWHM}}{2\sqrt{\ln(2)}} \quad (3.9)$$

The average laser power is a simple function of pulse energy E_{Pulse} and pulse rate, while the energy of a single pulse can be defined as the product of an area, in this case $A = \pi(D_{FWHM}/2)^2$ and an average energy density U_{Pulse} . At the same time the pulse energy density must be the integral of the intensity over time:

$$P_{Laser} = E_{Pulse} f_{Laser} \quad (3.10)$$

$$E_{Pulse} = U_{Pulse} A \quad (3.11)$$

$$U_{Pulse} = I_{max} \int \left(\exp\left(-\left(\frac{t-t_0}{t_S}\right)^2\right) \right) dt \quad (3.12)$$

By combining Eqs. (3.10), (3.11) and (3.12), the maximum intensity can be calculated from the experimental conditions:

$$I_{max} = \frac{P_{Laser}}{2\pi\sqrt{2\pi}t_S f_{Laser} (D_{FWHM}/2)^2} \quad (3.13)$$

Charge carrier dynamics

To calculate the Fermi energy levels (Eqs. (2.14) and (2.15)) of each charge carrier type the electric potential φ is needed. For this, the Poisson equation must be solved.

$$\epsilon \nabla^2 \varphi = -q(p - n + N_D - N_A) - N_t \quad (3.14)$$

Here N_D is the ionized donor concentration, N_A is the ionized acceptor concentration and N_t is the density of charged trap states. The charge carrier concentrations n and p are calculated according to the Fermi statistics presented in section 2.1.4. Since the band edge energies E_V and E_C can be given as simple functions of the electric potential (Eqs. (2.16) and (2.17)), φ becomes the only variable in the Poisson equation, which then can be solved numerically and its result can be used to solve all other surrounding equations.

The current densities are calculated from Eqs. (2.22) and (2.23), following the drift/diffusion model. Simultaneously, charge carrier concentrations follow their respective continuity equations for their time evolution (Eqs. (2.20) and (2.21)). In these equations the total recombination rate is the sum of the rates of all recombination mechanisms taken into account (see section 2.1.4). At the CdS/CIGSe interface thermionic emission is considered (Eq. (2.59)) as well as interface recombination (Eq. (2.38)). In the bulk material radiative and SRH recombination are considered (Eqs. (2.27) and (2.37)).

Defect densities N_t are defined as a distribution over defect energies with a Gaussian shape, with N_0 as the maximum value, E_T as the central energy and E_S as the standard deviation:

$$N_t(E) = N_0 \exp\left(-\frac{(E - E_T)^2}{2E_S^2}\right) \quad (3.15)$$

For defects acting as traps, the rates of capture R_c and emission R_e are dependent on the fraction of occupied traps f_t , which ranges between 0 and 1.

$$R_c = \sigma_n v_{th} n N_t (1 - f_t) \quad (3.16)$$

$$R_e = \sigma_n v_{th} N_t f_t N_C \exp\left(-\frac{E_C - E_T}{kT}\right) \quad (3.17)$$

3.3.3 Material parameters

Table 3.3.1 contains an overview of the most relevant material parameters for each layer.

Simulation parameter	ZnO:Al	i-ZnO	CdS	CIGSe
Thickness d (μm)	0.87	0.07	0.065	1.92
Electron affinity $\zeta_{n,0}$ (eV)	4.47	4.47	4.27	4.34(f)
Band gap E_g (eV)	3.33	3.3	2.4	1.18 (f)... 1.36 (b)
Absorption coefficient α at $\lambda = 650$ nm (μm^{-1})	X	X	1	2.91 (f)... 3.15 (b)
Doping concentration N_A (cm^{-3})	$n:1\cdot10^{20}$	$n:5\cdot10^{17}$	$n:5\cdot10^{17}$	$p:1\cdot7\cdot10^{15}$ (DA) / $p:2\cdot2\cdot10^{16}$ (LS)
Electron mobility μ_n (cm^2/Vs)	100	100	100	60
Hole mobility μ_p (cm^2/Vs)	25	25	25	5
Dielectric constant ϵ_r	9	9	10	13.6
Effective density of states cond. band N_C (cm^{-3})	$2\cdot2\cdot10^{18}$	$2\cdot2\cdot10^{18}$	$2\cdot2\cdot10^{18}$	$2\cdot2\cdot10^{18}$
Effective density of states val. band N_V (cm^{-3})	$1\cdot8\cdot10^{19}$	$1\cdot8\cdot10^{19}$	$1\cdot8\cdot10^{19}$	$1\cdot8\cdot10^{19}$
Radiative recombination constant B_{rad} (cm^3s^{-1})	-	-	-	$2\cdot10^{-9}$
Thermal velocity v_{th} (cm s^{-1})	$1\cdot10^7$	$1\cdot10^7$	$1\cdot10^7$	$1\cdot10^7$
Maximum of defect density distribution N_0 (cm^{-3})	10^{17}	10^7	$4\cdot5\cdot10^{17}$	$1\cdot1\cdot10^{16}$ (DA, T1) / $9\cdot9\cdot10^{14}$ (DA, T2) $3\cdot2\cdot10^{16}$ (LS, T1) / $9\cdot9\cdot10^{14}$ (LS, T2)
Central energy of defect distribution $E_C - E_T$ (eV)	1.65	1.65	1.2	0.119 (DA, T1) / 0.227 (DA, T2) 0.094 (LS, T1) / 0.227 (LS, T2)
Standard deviation of defect energy distribution E_S (eV)	0.0707	0.0707	0.0707	0.0162 (DA, T1) / 0.05 (DA, T2) 0.0177 (LS, T1) / 0.05 (LS, T2)
Electron capture cross section of defects σ_n (cm^2)	$1\cdot10^{-12}$	$1\cdot10^{-12}$	$8\cdot10^{-17}$	$1\cdot10^{-14}$ (DA, T1) / $3\cdot10^{-14}$ (DA, T2) $1\cdot10^{-14}$ (LS, T1) / $3\cdot10^{-14}$ (LS, T2)
Hole capture cross section of defects σ_p (10^{-14} cm^2)	$1\cdot10^{-12}$	$1\cdot10^{-12}$	$8\cdot10^{-12}$	$1\cdot10^{-18}$ (LS, T1) / $1\cdot10^{-18}$ (LS, T2) $1\cdot10^{-18}$ (LS, T1) / $1\cdot10^{-18}$ (LS, T2)
Interface recombination velocity S_0 (cm s^{-1})	ZnO:Al/i-ZnO: -	i-ZnO/CdS: -	CdS/CIGSe: 10^4	-

Table 3.3.1: Main parameters for simulation. For the band gap E_g of the CIGSSe absorber, there is a linear increase from front (f) to back (b). The same is true for the absorption coefficient α . The doping concentration N_A of the absorber layer changes between conditioning states DA and LS. The CIGSe absorber also has two identified defect states (T1, T2).

4 Results

In this chapter the simulation model detailed in previous chapters is applied to three different topics of investigation. The steps taken and results obtained are presented in three sections, with each section focusing on one single topic of investigation. All three topics are closely related to the evaluation of material quality and solar cell efficiency via time-resolved photoluminescence measurements.

The first topic (Section 4.1) is the influence on TRPL measurements of changes in single material parameters affected by metastability. The second topic (Section 4.2) is the correlation between photoluminescence lifetime and open circuit voltage. The third topic (Section 4.3) is the influence of p-n junction on TRPL measurements.

4.1 Parameter study and metastability

The metastable changes in CIGSe thin film solar cells caused by heat and illumination treatment have an influence on their efficiency as well as on their PL decay. Therefore it is relevant to understand which of the parameters changed by such conditioning has the strongest influence on efficiency and PL lifetime. This analysis is key if the results of time-resolved photoluminescence measurements are to be used to evaluate device efficiency.

A basic one dimensional SCAPS-1D simulation model was previously developed within the research group by Heise et al. [11] and Keller [80]. Especially Ref. [11] focuses on the exact same samples as the ones investigated in this work. For these devices the TRPL behavior was measured and they were electrically characterized to extract their parameters for simulation. The metastable changes were observed to have an influence on the electrical behavior, i.e. IV characteristic and IQE spectrum, as well as on TRPL decay curves. It was found that samples annealed in the dark for 15 hours at 90 °C have a lower doping density than samples which were first dark annealed and then additionally light soaked under an AM1.5 spectrum for 9 hours at 90 °C. Moreover, light soaking increases the defect density of the samples and shifts the energy of the defects.

The simulation focuses on reproducing these effects of metastable changes of material parameters. The SCAPS-1D simulation model was set to contain only three main changes after light soaking, namely increased doping concentration, increased defect density and change in defect energy. It was verified that the change in these three material characteristics is sufficient to explain the observed changes in internal quantum efficiency and current-voltage characteristic. Furthermore, it was

demonstrated via electron beam-induced current measurements that the diffusion length of electrons was reduced after light soaking. This was interpreted as proof of a reduced photoluminescence lifetime in the light soaked samples, which fits well with the observed behavior measured in TRPL and with the measured increase in doping concentration and defect density. Nevertheless, TRPL measurements of these samples have only been characterized by analytical fitting so far. In this work, the existing simulation model is expanded to include time-resolved simulations.

The goal of this section is to recognize via simulation which of the material parameters affected by metastability has the strongest influence on TRPL measurements. To analyze this topic, a parameter variation was carried out. The starting point is presented as a simulation model capable of accurately reproducing the TRPL measurement results of the investigated samples. From this simulation model as a basis, the effect of changing the values of single material parameters is recorded. The results in this section have also been summarized in Ref. [9].

4.1.1 Research steps

The simulation model used for this section is the one described previously in section 3.3. The material parameters are directly taken from table 3.3.1.

TRPL measurements and simulations are based on research done by Heise et al. [11] on the investigated samples. Some of the experimental values are also taken from Ref. [11]. Additional experimental data was used in order to include a variation of experimental conditions. As discussed in section 2.2, simulating data from experiments with different conditions makes it possible to determine the parameter values for the simulation model with higher confidence.

Measurements were performed on samples that were chemically etched to remove the ZnO:Al and i-ZnO n-type window layers. The etching was done with 5% acetic acid for 3 minutes. Thus, the samples consist only of CdS buffer layer and CIGSe absorber. Two sets of samples were investigated. All samples were dark annealed for 15 hours at 90 °C. The first set of samples, here labeled “DA” was left in this state. A second set of samples, labeled “LS”, was additionally light soaked under AM 1.5 spectrum for 9 hours and at 90 °C.

A number of material parameters were detected to change between the DA and LS states [11]. Table 3.3.1 contains the values of these parameters for each of the states. Specifically the doping concentration, the density of defect states and their distance from the conduction band were experimentally found to change with metastable conditioning. Two distinct defect states near the conduction band were found, also detailed in Table 3.3.1. The capture cross sections of these traps were adjusted as one of the free fitting parameters to accurately simulate the TRPL behavior of the samples. The reason why the capture cross sections are an adequate fitting parameter is that they cannot be experimentally determined. Therefore they constitute one of the degrees of freedom for tuning of the simulation model. To obtain good results it was necessary to assume a doping concentration lower than that measured for both states. Nevertheless, the ratio between measured and simulated doping concentration was equal for both states $N_{A,meas}/N_{A,sim} = 1.63$. The discrepancy between measurement and model can be a result of the contribution of defect states to the

measurement of the capacitance of the space charge region. This effect can lead to experimental values of N_A that are too high [29, 87].

The variation of experimental conditions was done by changing the power of the excitation laser. This was done to increment the level of confidence on the parameter set used for the model and to gain deeper physical insight into the processes happening in TRPL measurements, as discussed in sections 2.2 and 3.3. Using neutral density filters the laser power was varied and measurements were carried out for values $P_{Laser} = 0.5, 1, 2$ and 7 mW. The initial density of excited carriers Δn_0 is given here as a multiple of the doping density N_A , which is dependent on the state of the sample. For DA samples the values of Δn_0 range from $6 \cdot N_A$ to $85 \cdot N_A$, meaning that the samples are always under high injection conditions. For LS samples Δn_0 ranges from $0.5 \cdot N_A$ to $7 \cdot N_A$. This corresponds to low injection for the first value and high injection for the last one, with a transition between both regimes for the intermediate laser powers.

After simulating the variation of experimental conditions, a further series of simulations was performed. In each set of simulations a single material parameter of the CIGSe absorber was varied. The focus of this parameter variation was on the parameters detected to change between DA and LS states, i.e. doping concentration, defect density and defect energy. Further parameters were also varied, which could have a strong effect on the PL decay behavior, in this case the radiative recombination constant and interface recombination velocity. The range for variation of each parameter are indicated in Fig. 4.2 and Fig. 4.3.

Simulations of the TRPL experiments were carried out with Sentaurus TCAD version J-2014.09-SP1 [78]. A total time of 200 ns after arrival of the laser pulse was simulated. The detected defect states were taken mainly as traps, i.e. the recombination rate over these defects is very low. Using strongly asymmetric capture cross sections (see table 3.3.1) the recombination is greatly reduced. This makes the defect states have their main effect by trapping and emitting electrons from and to the conduction band. Simulations and experiments were performed at a temperature of 300 K.

4.1.2 Results

This first implementation of the simulation model was successful in simulating the experimental results of time-resolved photoluminescence of CdS/CIGSe layer junctions. Figure 4.1 shows the experimental data next to the corresponding simulations for DA and LS samples at different injection levels, i.e. quotient between initially generated charge carrier densities Δn_0 and doping concentration N_A . From the analytical model (Eq. 2.29), the time evolution of PL emission is expected to be a function of the injection level. In the experimental data it can be recognized that the PL decay of LS samples is significantly faster than that of DA samples under similar injection levels. This can be seen when comparing the case with $\Delta n_0 = 6 \cdot N_A$ for DA and $\Delta n_0 = 7 \cdot N_A$ for LS samples. This difference in PL decay time can be theorized to be a result of the increased doping concentration or defect density in the LS state. The variation of single parameters is aimed to help recognize which of these parameters has the dominant influence, if any.

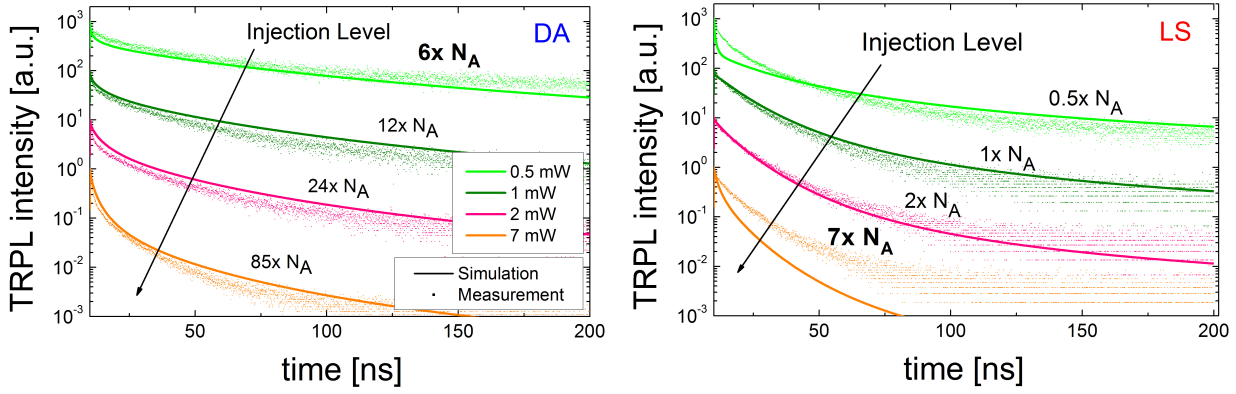


Figure 4.1: From [9]: Simulated curves (solid lines) and experimental data (scattered) of TRPL decay for dark annealed (DA) and light soaked (LS) conditions of CdS/CIGSe junctions. A variation of the excitation laser power was carried out. The injection level is given in multiples of the doping concentration N_A .

For the DA state, the agreement between experiment and simulation is good throughout all simulated injection levels. In the case of LS samples, the agreement is better at intermediate injection levels. In low injection, a very fast PL decay is simulated which is not observed in experiments. At high injection, the simulated PL decay for the LS sample is faster than that observed in experiments.

The results of varying the doping density of the CIGSe absorber are shown in Fig. 4.2. Here the values for the defect states of the DA samples were taken, while exclusively the doping concentration was changed. The blue curve in Fig. 4.2 corresponds to the N_A value of the DA state, while the red curve corresponds to that of the LS state. As observed previously in the variation of excitation power, with higher doping density a very fast decay during the first few nanoseconds ($t < 20$ ns) appears. The doping concentration can influence the PL decay lifetime in two distinct ways. Firstly, it reduces the overall radiative lifetime of the charge carriers (Eq. (2.30)). However this would not lead to a marked transition between a fast and a slow decay. Secondly, a higher doping concentration creates a stronger bending of the energy bands at the space charge region. This leads to a stronger charge separation (see section 2.2.3) and to a short, fast decay in the first few nanoseconds after excitation. This has also been observed for other samples from the same producer [88] and for samples with a p-n junction containing ZnO and CdS as the n-partners [43]. This effect will be studied in more detail in a later section.

Two further parameters observed to change between LS and DA state were investigated (Fig. 4.3 “a” and “b”). In the case of the defect density N_t , the difference in value between the two states creates an effect, which is significantly weaker than that of the change in doping concentration. Since the defects are assumed to act almost exclusively as traps, i.e. having very low recombination, the density would have to be increased by more than one order of magnitude to observe a significant change in TRPL decay. This would be a change much larger than the one measured. Regarding the influence of shifting the defect energy on PL decay, in this case the difference observed between LS and DA states is negligible.

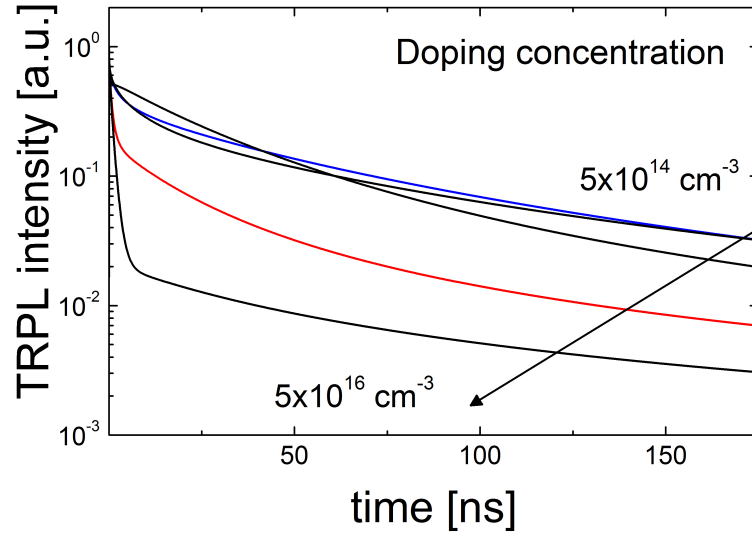


Figure 4.2: From [9]: Simulated curves of TRPL decay under variation of the doping concentration of the CIGSe absorber and constant excitation power. The blue curve corresponds to the doping concentration of the dark annealed state, while the red curve corresponds to the doping density of light soaked samples.

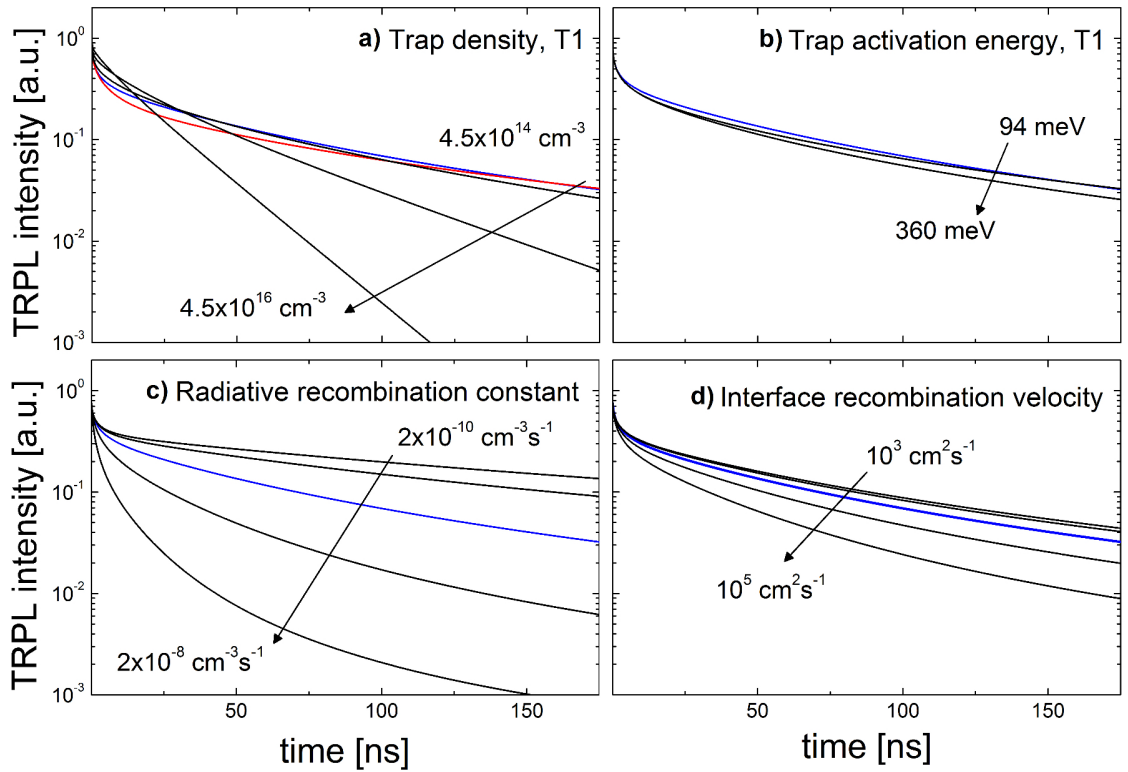


Figure 4.3: From [9]: Simulated curves of TRPL decay under variation of multiple material parameters: a) defect density, b) distance of defect states from the conduction band edge, c) radiative recombination constant and d) interface recombination velocity. Blue curves have parameter values corresponding to the dark annealed state, while red curves correspond to the values used for light soaked samples.

From the parameter variations discussed so far it can be concluded that the change in TRPL behavior between dark annealed and light soaked samples is dominated by their difference in doping concentration. Other treatment methods that increase efficiency of CIGSe solar cells by increasing the doping concentration of the absorber can be expected to have similar results on the TRPL behavior, namely faster decay at constant excitation power.

The last two parameters varied were independent on the state of the sample (Fig. 4.3 “c” and “d”). The radiative recombination constant is characteristic to the material quality of the CIGSe absorber and the interface recombination velocity depends on the interface partner and the quality of the production of the layer stack. For these cases the base values of the DA state were used. While these parameters can also be observed as free fitting parameters, to achieve a significant difference in TRPL decay they have to be varied by one or more orders of magnitude, which greatly reduces their role as fitting parameters, as the values are kept in the order of magnitude found in literature.

4.1.3 Summary

A reasonable agreement between TRPL simulations and experiments was achieved. This result was obtained with the same simulation model applied previously [11] to accurately simulate IV and EQE measurements performed on the same samples, which was then expanded in this work to perform time-resolved simulations. Two types of samples, dark annealed and light soaked, were investigated. Between these two conditioning states some differences were experimentally found. Namely the doping concentration of the CIGSe absorber, its density of defect states and the distance of these states from the conduction band were detected to change. These parameter changes were implemented in the model to simulate the two different CIGSe conditioning states. The capture cross sections of defect states in the absorber were used as free fitting parameter, as they are one of the material parameters not experimentally available. Additionally, the doping concentration assumed for the CIGSe absorber also had to be adjusted in simulations to achieve good results. This adjustment is estimated to be within the uncertainty in the measured values. Additionally, the factor by which the doping concentration was measured to shift between the two conditioning states of the absorber was kept in the simulations. The difference between measured and simulated doping density can be attributed to the influence of defect states on the capacitance voltage measurements carried out to determine the doping concentration.

As a variation of experimental conditions, the laser power for excitation was changed both in experiments and simulations. This allowed to find the correct parameter values for the simulation model (capture cross sections and doping density) with a higher level of confidence. Several parameter variations were done inside the simulation with the aim of recognizing which of the material parameters affected by metastability plays the most important role in the changes observed in TRPL decay between DA and LS states. Of the parameters investigated, the doping concentration was found to have the strongest influence on TRPL decay curves.

A deviation between simulations and experiments at low injection conditions and high doping concentration of the absorber was observed. In such cases the model calculates a very fast and

short decay in the first nanoseconds after excitation, which was not observed in experiments. It is estimated that this is an effect of charge carrier separation at the p-n junction. To better understand the source of this deviation, the influence of the p-n junction on TRPL measurements will be investigated in later sections.

4.2 Correlation between photoluminescence lifetime and open circuit voltage

Before TRPL is applied to determine the quality of CIGSe material during production, a clear correlation between the results of TRPL measurements, e.g. photoluminescence lifetime τ_{PL} or minority carrier lifetime τ_n , and device performance must be demonstrated. Currently, however, this is still a topic of study and discussion in the scientific community. In this section the most recent findings in the topic are presented. After this introduction, the research steps taken and results obtained in the investigation of this topic will be summarized. The results in this section have been previously published in Ref. [10]. In order to simulate the solar cell performance parameters, such as open circuit voltage, simulations of IV characteristics and EQE spectra, in addition to those of TRPL, are introduced. All three experimental methods are simulated with the same model. After demonstrating the validity of the simulation model, a parameter variation is carried out. The goal of this variation is to investigate the influence of single material parameters on TRPL lifetime and open circuit voltage. This way the correlation between both quantities can be analyzed.

4.2.1 Theory

From the formula for the open circuit voltage (Eq. (4.1)) it is expected that V_{OC} depends directly on the carrier lifetime, as the saturation current density J_0 also shows this dependency [89].

$$V_{OC} = \frac{kT}{q} \ln \left[\frac{J_{SC}}{J_0} + 1 \right] \quad (4.1)$$

Some studies report a correlation between PL lifetime and open circuit voltage as an indirect measure of cell efficiency [61, 62]. Meanwhile, other studies show only a weak correlation [90, 91] or are not able to establish any clear correlation [60, 92]. This discrepancy in the results is partly attributed to the fact that while CIGSe solar cell efficiency becomes higher over the years, parameters that did not play a dominant role before, such as defect density, become more and more relevant [92].

Previous studies about the correlation between photoluminescence lifetime and open circuit voltage take experimental results and give an analytical approximation for the observed correlation.

Repins et al. [91] describe the relation between V_{OC} and τ_{PL} with the empirical constants C_1 and C_2 , with I_0 as the initial intensity of the TRPL decay curve.

$$V_{OC} = C_1 \ln \left(\tau_{PL} \sqrt{I_0} \right) + C_2 \quad (4.2)$$

For TRPL measurements performed with a 670 nm laser they obtain a coefficient of determination of $R^2 = 0.68$ for the correlation between V_{OC} and τ_{PL} . When measured with a 905 nm laser they obtain a better correlation with $R^2 = 0.83$.

Maiberg et al. [92] have identified an entire family of curves for $V_{OC}(\tau_{PL})$. For this description they start from the dependence of V_{OC} on the short circuit current density J_{SC} and saturation current density J_0 and parametrize both current densities as functions of the PL decay lifetime τ_{PL} , the density of electrons in trap states n_t and the density of trap states N_t . They have found that this family of curves can describe the spread of different values of V_{OC} for the same PL lifetime, which arises from a fluctuation in the density of traps. This is a first model to explain the observed lack of correlation between V_{OC} and τ_{PL} .

$$V_{OC} = \frac{kT}{q} \ln \left(\frac{J_{SC} \left(\frac{n_t}{N_t} \tau_{PL} \right)}{J_0 \left(\frac{n_t}{N_t} \tau_{PL} \right)} \right) \quad (4.3)$$

4.2.2 Research steps

The base for the simulation model and experiments are the same as in previous sections. IV and EQE simulations and experiments were performed on layer stacks of ZnO:Al/i-ZnO/CdS/CIGSe, while TRPL measurements and simulations are done on a layer stack of CdS/CIGSe. In this section two different types of TRPL simulations are carried out. The first type serves to verify the simulation model. Therefore it must match the conditions and results of experiments as closely as possible. The second type of simulation is applied to investigate the role of individual absorber material parameters. Such simulations consider only the bare absorber layer.

The 1-D simulations at 300K for this section were carried out with Sentaurus TCAD version L-2016.3 [79]. For TRPL simulations, open circuit conditions were applied. In EQE simulations the system was set to short circuit conditions, while for IV simulations, the voltage between the two contact surfaces is set to a range of values corresponding to the experiment. The spectrum of illumination is changed between the experiments, with monochromatic, pulsed excitation for TRPL, constant monochromatic excitation with varying wavelength for EQE and constant excitation with solar spectrum for IV.

An important difference to the simulation model from previous sections are the capture cross sections of the defect states in the CIGSe absorber. So far the capture cross sections were assumed to be highly asymmetric with $\sigma_n = 10^{-14} \text{ cm}^2$ and $\sigma_p = 10^{-18} \text{ cm}^2$ and therefore the defect states were treated as pure traps with negligible recombination. To tune results obtained with a single simulation model to those of IV, EQE and TRPL measurements simultaneously, the capture cross sections had to be adjusted as free fitting parameters. In this section the values are set to $\sigma_n = 10^{-14} \text{ cm}^2$ and $\sigma_p = 10^{-15} \text{ cm}^2$. While these values are still significantly asymmetric, recombination over the defect states cannot be longer neglected. Additionally, recombination at the back contact surface was also added to the model.

In a first step, the simulation model is used to reproduce the experimental results of IV, EQE and TRPL measurements. This is done to demonstrate the suitability of the simulation model for the later steps. The TRPL simulations in this case are done for two injection levels with $\Delta n_0 = 0.7 \cdot N_A$

Simulation parameter	Step	Range of values
Doping concentration N_A (cm^{-3})	logarithmic	$n:(0.1-2)\cdot 10^{16}$
Hole mobility μ_p (cm^2/Vs)	logarithmic	0.01-5
Total defect density N_t (cm^{-3})	linear	$(0-1.4)\cdot 10^{16}$
Central energy of defect distribution $E_C - E_T$ (eV)	linear	0.094-0.5
(Ga)/(Ga+In)-ratio back side GGI_{Back}	linear	0.22-0.5

Table 4.2.1: Parameters of the CIGSe material varied during the study of the correlation between open circuit voltage and photoluminescence lifetime. The range of variation and the type of step is given. Step size is kept constant in both the linear and the logarithmic case.

for low injection and $\Delta n_0 = 3 \cdot N_A$ for high injection. The parameter values of light soaked samples are used for this step.

In a second step, a series of parameter variations is carried out to investigate the correlation between V_{oc} and τ_{PL} . In this case TRPL simulations were performed for pure CIGSe layers. This method was chosen to again avoid changes to the results coming from the dynamics of excitation at a p-n junction and to focus on the behavior of the absorber. A variation of individual parameters was carried out to help extract further information from simulations. The range of parameter values used is shown in Table 4.2.1.

To obtain data for this analysis, the PL decay lifetime has to be extracted from the simulated curves. This is done by plotting the instantaneous lifetime τ_{inst} from Eq. (3.1) and extracting the asymptotic value τ_∞ defined in Eq. (3.2). The motivation for this type of analysis is to find a value for the PL lifetime that is descriptive of the simulated decay curve but is mostly tied to the actual charge carrier lifetime of the material and not to time-dependent processes coming from pulsed excitation (see section 3.2).

Fig. 4.4 shows examples of the influence of single material parameters on the shape of TRPL decay curves and on their corresponding $\tau_{inst}(t)$ for ideal samples with no defect recombination. Here, increasing the excitation power of the laser changes the dynamics and therefore also the TRPL decay. However it can also be recognized in the plot of τ_{inst} that the decays converge towards a common lifetime. This long lifetime is more closely related to the recombination lifetime of the carriers in the absorber. The differences in the early part of the decay are caused by the changes to the concentration gradient of the excited electrons and to the bending of the bands. In contrast, when the doping concentration is increased, the asymptotic lifetime τ_∞ changes significantly. This is because of the faster radiative recombination.

The CIGSe parameters chosen for the variation are well known to have an influence on the efficiency of thin film solar cells. These were the doping concentration N_A , the gallium content at the back contact GGI_{back} , the density of defects N_t , the distance of defect states from the conduction band $E_C - E_t$ and the mobility of holes μ_p .

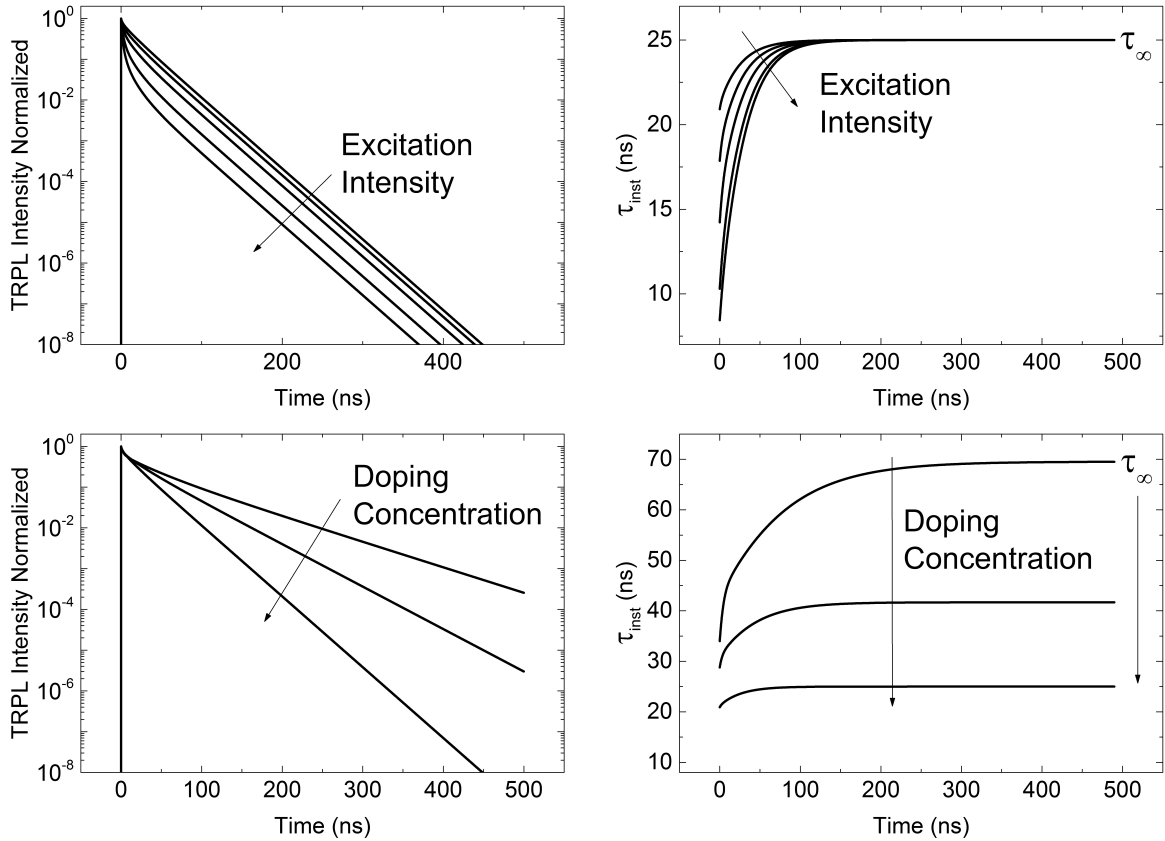


Figure 4.4: From [10]: Simulated TRPL decays (left side) of isolated CIGSe absorbers and their corresponding graphs for the instantaneous lifetime τ_{inst} (right side). Here an ideal model with no defect recombination is used. The influence of different model and simulation parameters on the extracted asymptotic lifetime τ_{∞} is shown.

Two distinct batches of parameter variations were carried out. In both batches single parameter values are changed, while all other parameter values are left at the values corresponding to a base parameter set. The two batches differ in the parameter set chosen as a base. The first batch of simulations (Fig. 4.6 “a”) starts from a simplified model, in which the CIGSe absorber has no composition gradient, no defect states inside the band gap and no surface recombination at either front or back contact. This simplified base point for the parameter variation is labeled “Simplified Model”. This first batch of simulations is done with the goal to better isolate the effect of each single parameter. An exception to the rule was done when varying the energy of defects. In this case the simplified model was adjusted to include defect states with the density listed in Table 3.3.1 for the LS state, since otherwise the result of changing the defect energy would be meaningless. The second batch of simulations (Fig. 4.6 “b”) starts from the parameter set used to simulate the experimental data and is labeled “Match Exp.”. Here recombination over defects, composition gradient and surface recombination are taken into account. This step was taken to test the validity of the results from the first batch in a setting in which the effects of the parameters are combined. The plots for V_{OC} against the extracted PL lifetime τ_{∞} resulting from these variations can be seen in Fig. 4.6 “a” and “b”.

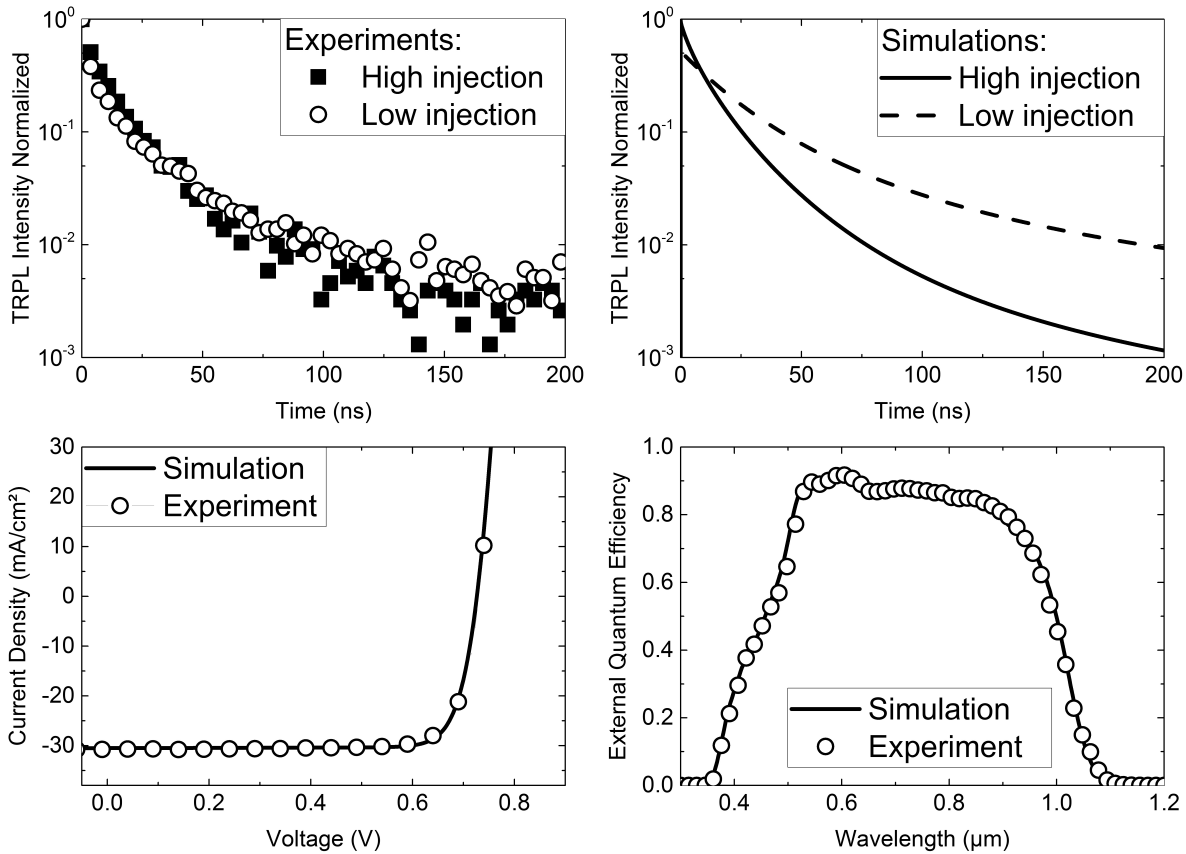


Figure 4.5: From [10]: Results of simulations compared to experiments. On the upper left are the TRPL experiments for LS samples in low and high injection conditions. The corresponding simulations are shown at the upper right. IV simulation and experimental data are shown on the lower left, while EQE is on the lower right.

4.2.3 Results

Verification of the model

With the modifications mentioned above, the established simulation model is used to reproduce the results of TRPL, IV and EQE experiments. The comparison between simulation and experiment can be seen in Fig. 4.5. The results of the TRPL simulations are for CdS/CIGSe layer stacks, to match the experimental conditions. For IV and EQE ZnO:Al/i-ZnO/CdS/CIGSe layer stacks were used. The agreement achieved between experiments and simulation is high in the case of EQE and IV. At high injection the TRPL simulation reproduces the experimental results accurately. In low injection however, the simulation predicts a decay slower than observed. This again is due to the model overestimating the influence of charge carrier separation at the space charge region in LS samples, as seen in section 4.1.2. With these results as a base, it is then reasonable to use the simulation to estimate the change in open circuit voltage and photoluminescence lifetime created by the variation of single parameters.

Parameter variation

The results of the parameter variation are compacted into Fig. 4.6. The TRPL simulations for this study were done on CIGSe absorbers without CdS buffer layer. The graphs show plots of V_{OC} against τ_{∞} . The axis for the asymptotic lifetime is scaled logarithmically. First the results for the simplified model (graph “a”) will be discussed. It can be quickly recognized that many different relations between V_{OC} and τ_{∞} arise. The type of correlation observed is strongly dependent on the parameter being varied. In some cases, a positive correlation was found, for example, when increasing the distance of the defect states from the conduction band E_T . In other cases, there is a negative correlation, like when the doping concentration N_A is changed. A last type of case presents an independent behavior of V_{OC} and τ_{∞} , e.g. when the gradient of the gallium content is increased.

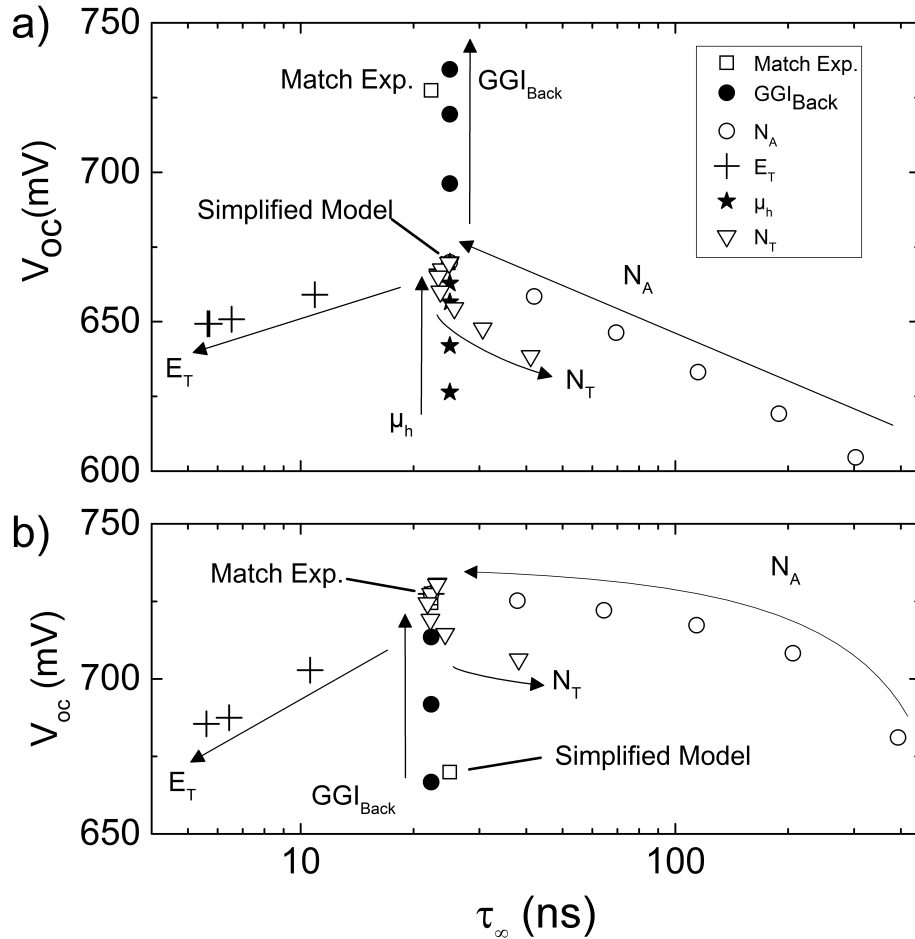


Figure 4.6: From [10]: Results of parameter variation for the study of the correlation between open circuit voltage V_{OC} and asymptotic lifetime τ_{∞} . The lifetime axis is scaled logarithmically. Two sets of parameter variations were carried out: a) starting the variation from a simplified simulation model with no defect recombination, no gallium gradient and no front surface recombination, b) starting from the parameter set used to match experiments in Fig. 4.5. The parameters varied are the gallium content at the back contact GGI_{Back} , the doping concentration N_A , the density of defects N_T , the mobility of holes μ_h and the distance of defects from the conduction band E_T .

4 Results

The results obtained for each parameter variation will now be discussed individually. In general it is useful to think of the open circuit voltage as a function of the splitting of the quasi Fermi levels in the absorber. The goal of this discussion is to recognize if the results of the simulation are physically reasonable and can be interpreted as valid, at least in a general, qualitative sense. It is also useful to develop an intuitive understanding of the behavior observed.

Energy of defects

When the distance of defects from the conduction band is increased, the rate of emission of electrons back to the conduction band is reduced drastically (Eq. (3.17)), making it more probable for the electrons to recombine with holes. This increased recombination naturally decreases the lifetime of charge carriers and therefore the asymptotic lifetime. At the same time the density of carriers in both bands is reduced by the stronger recombination, reducing the splitting of quasi Fermi levels and accordingly, the V_{OC} . This type of behavior is the one expected for ideal semiconductors, i.e. a positive correlation between PL lifetime and open circuit voltage. This variation series is the only one in which this type of behavior is observed. In general it can be expected that any material parameter which directly and primarily affects the non-radiative recombination rate will have this type of effect.

Defect concentration

The defect concentration has a direct influence on the recombination lifetime. Therefore an increased density of defects is expected to decrease both V_{OC} and PL lifetime simultaneously. This behavior can change however, if the defects are shallow and trapping and emission start playing a role. This is what can be seen in Fig. 4.6. Here the relation between V_{OC} and τ_{∞} changes as the density of the defects increases. At first, the expected positive correlation is seen, but as the density increases further, the trapped electrons do not have enough recombination partners due to the smaller capture cross section assumed for holes. This increases the PL lifetime, but since the non-radiative recombination rate is still increasing, V_{OC} is further reduced, creating a shift into a negative correlation. A correct assessment of material quality via TRPL is therefore only possible if additional information is available. In this case the defect landscape should be known and the possible influence of trapping and emission over flat defects shall be considered.

Doping concentration

An increase in doping concentration was here observed to increase the open circuit voltage, while decreasing the PL lifetime, creating an effect opposite to the one seen when the non-radiative recombination is increased. Since the first set of simulations is done for a simplified model with no recombination over defects, the radiative recombination dominates the PL decay. As seen in Eq. 2.30, the radiative lifetime becomes shorter with increasing doping concentration. Moreover, with increased doping in the absorber, the quasi Fermi level of holes moves closer to the valence band,

increasing the splitting of the Fermi levels and therefore the V_{OC} . Additionally, the space charge region in the p-type absorber becomes smaller and its band bending becomes stronger with higher doping. This has an effect on both, PL decay due to the effect of charge carrier separation, and on current collection, since the size of the space charge region is reduced. This is an example of a counter-intuitive result in which the efficiency of the solar cell is increased while the PL lifetime is decreased, e.g. due to the metastable changes of the sample. Therefore it becomes important to be aware of the history of a sample before trying to make assessments about its quality for PV applications via TRPL measurements.

Hole mobility

The mobility of charge carriers directly influences how carriers are redistributed after excitation. As the mobility becomes small, the charge diffusion is reduced and radiative recombination dominates. This changes the initial PL decay, but not the asymptotic lifetime τ_{∞} . In the presence of a p-n junction, this effect is even more marked, as charge carrier separation is also reduced. In both cases, a lower mobility results in a strongly reduced density of holes towards the back contact, which diminishes the splitting of quasi Fermi levels and therefore the V_{OC} . This is an example in which the simulation predicts an almost complete lack of correlation between V_{OC} and τ_{∞} . Any material parameter having primarily an influence on the redistribution of charge carriers after excitation but not on the recombination lifetime would be expected to have this type of effect.

Gallium gradient

As the content of gallium towards the back side of the absorber becomes higher, so does its band gap. This increases the splitting of the quasi Fermi levels and the V_{OC} . With the assumption used here of a linear gradient in gallium concentration over the depth of the absorber, varying GGI_{Back} leaves the asymptotic lifetime τ_{∞} unchanged. This is again, because the recombination lifetime is unaffected and only the redistribution of charge carriers after excitation is changed. The increase in the band gap towards the back side, which primarily affects the conduction band edge, creates a gradient in the electric potential for electrons. This potential gradient hinders the diffusion of electrons towards the back side, therefore influencing the early part of the TRPL decay. A change in the gradient of a linear gallium grading therefore significantly affects the V_{OC} but does not influence the PL lifetime. As the composition gradient is an important aspect of production, it is therefore necessary to check that the gradient is adequate before analyzing the quality of CIGSe absorber material via TRPL inspection.

Changing the shape of the gallium gradient, e.g. to a so called v-gradient, can significantly change these results. Simulations were carried out to test this constellation. In the case of a v-shaped gradient, the passivation of the front surface plays an important role. If front surface recombination is high, then an increase of gallium towards the front surface of CIGSe helps increase the charge carrier lifetime. If surface recombination is low or neglected, however, the asymptotic lifetime is again unaffected by the gallium gradient.

Combined effects

The results of the parameter variation for the case in which trap recombination, surface recombination and composition gradient are considered simultaneously (Fig. 4.6 “b”) are discussed here. While most of the results already presented still apply in this case, some differences can be observed. The influence of changing the hole mobility on the open circuit voltage is negligible when recombination over defects is taken into consideration. This is because for the experimental conditions chosen here the influence of non-radiative recombination and trapping over defects dominate over the effect of diffusion on the TRPL decay when both are considered simultaneously. Additionally, the rate of change of V_{OC} with increasing doping concentration is changed when recombination over defects is taken into account. The density of defects is kept constant during the N_A variation and this changes the ratio of defects to doping, which makes the role of recombination stronger with decreasing doping concentration. In real samples the doping and defect concentration are changed simultaneously due to metastability of the samples. This however does not change the negative correlation between V_{OC} and τ_∞ stemming from metastable changes.

4.2.4 Summary

The model used previously to calculate TRPL decays and successfully reproduce experimental results was adjusted to be able to additionally reproduce IV and EQE experiments with the exact same parameter set. A very good agreement between experiment and simulation was achieved for IV and EQE. TRPL simulations were able to reproduce experiments to a reasonable degree, with deviation from the experiments growing with decreasing injection level. After verifying the simulation model, an investigation of the correlation between open circuit voltage and photoluminescence lifetime was carried out by using parameter variations in the simulation model. IV simulations of entire cell stacks were used to calculate the open circuit voltage while TRPL simulations of pure CIGSe absorbers were used to obtain the photoluminescence lifetime. For this end the calculated TRPL curves were analyzed with help of the definition of an instantaneous lifetime and an asymptotic lifetime.

The influence of each individual material parameter was studied first. In this step a simplified simulation model without defect recombination, gallium gradient or surface recombination was used as the base case for the parameter variation to better isolate the effect of each parameter. No CdS buffer layer was included in TRPL simulations during the parameter variation to avoid the influence of the p-n junction on the results.

A second set of parameter variations was performed to confirm the results from the first series. In this second series the base case used contains the parameter values from simulations that reproduce experimental results accurately. From the parameter variation several different relations between open circuit voltage and photoluminescence lifetime were found. In the case of increased non-radiative recombination, the correlation was positive, as observed when the distance of defects to the conduction band was increased. In the case of increased Fermi level splitting but decreased radiative lifetime, a negative correlation was observed. This was the case with the variation of the

doping density. Increasing the density of defects can have two different effects. If the defects are deep inside the band gap and trapping of electrons plays no important role, then the open circuit voltage and the asymptotic lifetime are reduced simultaneously by increasing defect density and the correlation is positive. If on the other hand the defects are shallow and trapping is dominant, increasing the defect concentration raises the decay lifetime while still decreasing the open circuit voltage, thus a negative correlation emerges.

Two cases of non-correlation between V_{OC} and τ_{∞} were observed. This was seen for the variation of hole mobility and gallium content gradient. These two parameters do not affect the charge carrier recombination lifetime directly, but rather influence the TRPL decay by changing the dynamics of redistribution of the excited charge carriers during the first nanoseconds after excitation. When recombination over defects is considered, however, the influence of the mobility on the open circuit voltage was reduced to a negligible level. If recombination at the front surface is strong, an increased gallium gradient toward the front of the absorber can also have an influence on charge carrier lifetime.

The results are in agreement with literature, especially with the research done by Maiberg et al. [92], who have presented a first explanation for the observed lack of correlation between open circuit voltage and PL decay lifetime. In Ref. [92] this was calculated to be an effect of fluctuating defect densities between samples. To this explanation a further one is added here. It is also a possibility that fluctuations in the gradient of gallium content grading between samples also leads to a non-correlation between open circuit voltage and photoluminescence lifetime.

From the obtained results it is evident that TRPL measurements can only be used to assess material quality of CIGSe absorbers for photovoltaic applications if detailed knowledge about the energy of defects and composition gradient of the material are previously known. It is therefore recommended to make TRPL measurements more reliable by considering the spectral distribution of the time-resolved photoluminescence signal, while also observing the change in response by varying the wavelength of excitation. These methods, previously used by Kuciauskas et al. [41,44], permit to analyze the charge carrier lifetime and the composition grading of the samples with non-destructive and contactless methods, while yielding relevant information for the assessment of material quality. This relates directly to the motivation presented for this work.

4.3 Influence of p-n junction

In cases of high doping and low injection the TRPL decays for CdS/CIGSe layer stacks calculated with the simulation model here show a significant difference with the experimental data from literature. This difference manifested in previous sections in the form of a strong and fast decay during the first few nanoseconds of the calculated curves. The source of this effect suggested until now has been the influence of the p-n junction in the form of charge separation. Two predictions are made based on the results given by the simulation model. First, the presence of a CdS/CIGSe junction brings about a very fast PL decay in the first nanoseconds, coming from charge separation. Second, the presence or absence of such behavior is found to be dependent on the injection level. In this chapter the physical arguments to expect a fast decay for a p-n junction under low injection are presented. Additionally, this predicted fast decay is demonstrated in experiments. With this step, the simulation model is further validated by formulating a prediction that is also experimentally verified. The validity of the prediction is tested for varying doping concentrations of the samples. TRPL measurements with and without CdS buffer layers and under different injection levels provide further support for the claimed prediction.

4.3.1 Theory

As the charge carriers are generated in a strong electric potential gradient inside the space charge region, holes and electrons flow in opposite directions and the radiative recombination, dependent on the local value of the product $n \cdot p$, decreases rapidly. This gives rise to the fast decay observed during the first few nanoseconds of simulated curves under low injection. This effect is dependent on the injection level due to the screening effect that the generated charge carriers in the space charge region can have on the electric field present in the depletion zone. In Fig. 4.7 the energy bands of the CdS/CIGSe junction right after excitation ($t = 1$ ns) are presented for the high injection case ($\Delta n_0/N_A = 12.3$). Due to the high concentration of charge carriers generated toward the CdS/CIGSe interface, the band bending is reduced and the influence of charge separation is reduced. This screening effect is smaller with decreasing injection level.

The effect of p-n junction on TRPL measurements has been previously observed [76,88]. Metzger et al. [76] have measured and simulated a similar behavior for entire solar cells with ZnO/CdS/CIGSe layer stacks. However, they report that the effect vanishes for layer stacks composed only of CdS/CIGSe. They back up their results with one-dimensional, time-resolved simulations. This is a fundamentally different result from the one obtained from calculations in this work. The reasons for this deviation will also be discussed.

4.3.2 Research steps

Following the prediction that the effect of charge carrier separation is dependent on the injection level, a series of experiments at largely different injection levels were carried out. Making use of the metastable effects present in CIGSe absorbers, two sample sets with different doping concentrations

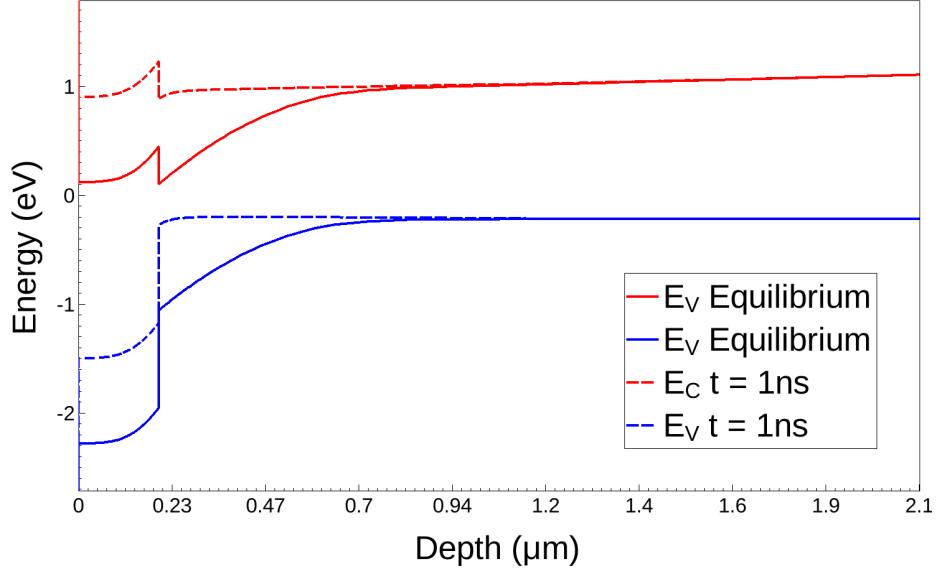


Figure 4.7: Band diagram of the CdS/CIGSe junction in equilibrium (solid lines) and 1 nanosecond after excitation with a laser pulse (dashed lines). The data is extracted from simulations under high injection conditions ($\Delta n_0/N_A = 12.3$) and correspond to a dark annealed sample.

were prepared. By measuring each set of samples under the appropriate excitation power, the same injection level can be achieved for both samples. For this section new samples were prepared from material previously manufactured by the industry partner. Like in previous chapters, dark annealed samples were treated for 15 hours at 90°C in the dark, while light soaked samples were additionally treated for 15 hours at 90 °C under AM 1.5 illumination spectrum at 1000 W/m².

The doping concentration of the two sets of samples was measured by capacitance-voltage characterization. For the dark annealed sample a value of $N_{A,DA} = (4.6 \pm 0.5) \cdot 10^{15} \text{ cm}^{-3}$ was measured, while for the light soaked sample, a value of $N_{A,LS} = (3.2 \pm 0.5) \cdot 10^{16} \text{ cm}^{-3}$ was obtained.

Additionally, the photoconversion efficiency of the samples was tested via current-voltage characteristics under AM1.5 illumination spectrum at 25 °C. Due to the small active area of the samples of $A_{DA} = (0.31 \pm 0.01) \text{ cm}^2$ and $A_{LS} = (0.25 \pm 0.01) \text{ cm}^2$, no metallic grid was applied on top of the ZnO layer for electrical characterizations. The values of the short circuit current were determined by quantum efficiency measurements and were taken as a calibration point for the light intensity of current-voltage measurements.

From the measured doping concentrations, the injection level at each excitation power was calculated. The data from this calculation can be extracted from Table 4.3.1. The following equation was used to calculate the injection level, i.e. the density of charge carriers initially generated at the absorber depth $x = 0$ in relation to the doping concentration:

$$\frac{\Delta n_0}{N_A} = \left(\frac{dN_{Photons,Pulse}}{dx} \frac{1}{A_{Laser}} \right) \Big|_{x=0} \frac{1}{N_A} \quad (4.4)$$

P_{Laser} (mW)	0.16	0.45	0.73	1.2	2.0	3.15
Injection level DA sample (multiples of N_A)	1	2.8	4.5	-	12.3	-
Injection level LS sample (multiples of N_A)	0.1	0.4	0.6	1	1.8	2.8

Table 4.3.1: Injection levels for dark annealed and light soaked samples under different excitation powers, as calculated with Eq. (4.4)

$$\frac{dN_{Photons,Pulse}}{dx} = \alpha(\lambda)N_{Photons,Pulse} \quad (4.5)$$

$$N_{Photons,Pulse} = \frac{E_{Photon}}{\bar{E}_{Pulse}} = \frac{hc}{\lambda} \frac{1}{(\bar{P}_{Laser}/f_{Laser})} \quad (4.6)$$

Here $N_{Photons,Pulse}$ is the total number of photons in a single pulse, A_{Laser} is the effective area of excitation and x is the depth inside the absorber. The total number of photons in a pulse can be calculated from the wavelength used for excitation λ , the pulse rate of the laser f_{Laser} and the average laser power \bar{P}_{Laser} with the Planck constant h and the speed of light c . The derivative of $N_{Photons,Pulse}$ over depth at $x = 0$ can be calculated from the absorption coefficient $\alpha(\lambda)$ corresponding to the wavelength λ . Here Beer-Lambert absorption is assumed. E_{Photon} stands for the energy of a single photon.

The simulation model was adjusted to include the measured doping concentrations of the samples. The density of traps was assumed to be the same as in previous samples. This includes the variation caused by dark annealing and light soaking, which is also taken from the simulation models presented in previous chapters. Though this step introduces an uncertainty, it was demonstrated in previous chapters that the difference in TRPL decay between the light soaked and dark annealed samples stems mainly from the change in doping concentration and that the difference in defect concentration has only a negligible effect. The values of the capture cross sections of defects are kept the same as in section 4.2. The parameters used for fitting of the curves in this section are the doping, thickness and electron affinity of the CdS buffer layer. The values for these three parameters, however, are kept equal for LS and DA samples.

To test the prediction that the observed effect of charge separation is caused by the p-n junction, TRPL measurements on samples with and without CdS buffer layer were carried out. The ZnO layer was etched from all samples by submerging them into an aqueous solution of 5% mass acetic acid for 3 minutes followed by a submersion in water for 1 minute to remove the etching agent. To etch the CdS layer the samples were submerged in an aqueous 5% mass hydrochloric acid solution for 3 minutes, again followed by 1 minute submersion in water. These methods of etching have been previously tested for samples from the same fabrication process [12, 52] and have been shown to yield the desired result, which is to selectively etch away only one layer respectively.

The TRPL measurements of CdS/CIGSe junctions and of bare CIGSe absorbers were done for multiple injection levels. All the experiments are compared to simulations to evaluate the validity of the predictions. Due to limitations of the experimental setup, no case of true low injection ($\Delta n_0 \ll N_A$) could be measured for the dark annealed samples. This was due to the relatively low doping concentration obtained after dark annealing, which would mean that a very low density of photons would be necessary to achieve low injection. This very weak excitation brings also a very weak photoluminescence emission, which is not detectable with the photomultiplier used and is completely overshadowed by the background noise.

4.3.3 Results

Electrical Characterization

The efficiency of the samples measured via current-voltage measurements was of $\eta_{DA} = (18.7 \pm 0.6) \%$ and $\eta_{LS} = (16.8 \pm 0.7) \%$ respectively. The open circuit voltage values extracted are $V_{OC,DA} = (670 \pm 2) \text{ mV}$ and $V_{OC,LS} = (710 \pm 2) \text{ mV}$. For the short circuit current the values $J_{SC,DA} = 33.1 \text{ mA/cm}^2$ and $J_{SC,LS} = 30.1 \text{ mA/cm}^2$ have been used as the reference point for adjustment of the illumination power during IV measurements.

The observed difference in open circuit voltage follows the trend expected when considering the measured change in doping concentration. However, the efficiency of the LS sample is lower than that of the DA sample, which is contrary to the previously observed behavior. This is interpreted as an increased recombination in the LS sample due to small shunts that mainly reduce the value of the short circuit current. Despite the material quality of the LS sample being lower, i.e. non radiative recombination being higher, the overall photoconversion efficiency of both samples is high enough for the samples to be deemed suitable for further TRPL investigations. Therefore it must be kept in mind that the overall TRPL decay of LS samples will probably present shortened lifetimes due to recombination over shunts. Nonetheless, the focus of this section is on the effect of charge carrier separation at the p-n junction and its dependence on doping concentration. Considering this, the results of TRPL measurements can still be adequately interpreted due to the fact that LS and DA samples have significantly different values of N_A , while showing only small differences in material quality. Lock-in thermography analysis was applied to the investigated samples previous to the electrical characterization. This was done to rule out the presence of large shunts that would greatly reduce the efficiency of the samples. Smaller shunts, however, like the ones assumed to be present here, are not detectable by this method.

TRPL

The results for experiments and simulations at two injection levels $\Delta n_0 = N_A$ and $\Delta n_0 = 2.8 \cdot N_A$ are shown in Fig. 4.8. A level of agreement similar to that observed in previous sections was achieved by tuning the doping concentration, thickness and electron affinity of the CdS buffer layer

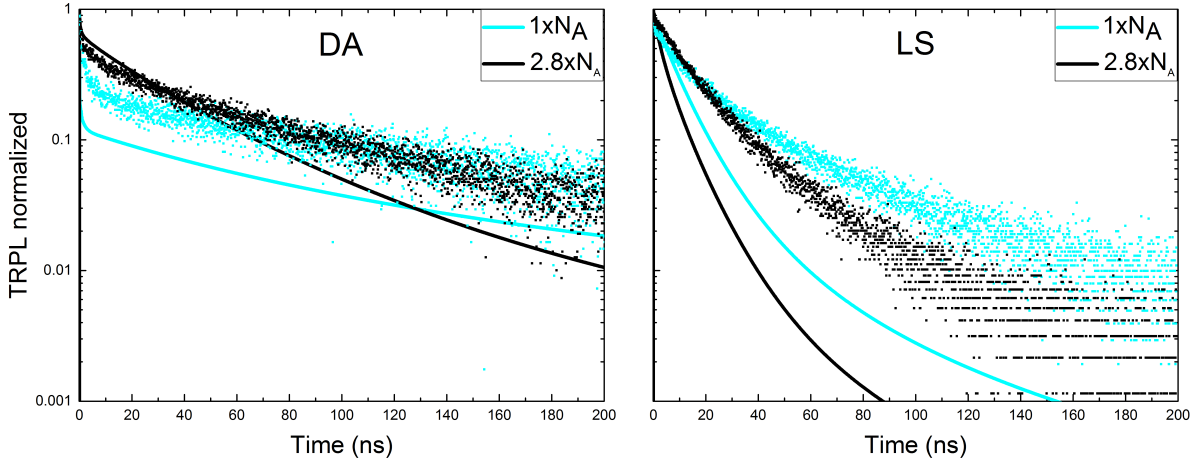


Figure 4.8: Results of simulation (solid lines) and experiments (scattered) of TRPL at two distinct injection levels with initial excited carrier densities $\Delta n_0 = N_A$ and $\Delta n_0 = 2.8 \cdot N_A$. On the left side the results for a dark annealed sample are presented, while the right side contains the data for a light soaked sample.

in the simulation. These values were kept equal for all simulated curves of both sample sets. The results shown here are for the values $N_{D,CdS} = 10^{17} \text{ cm}^{-3}$, $d_{CdS} = 200 \text{ nm}$ and $\zeta_{n,0,CdS} = 4.0 \text{ eV}$.

For the light soaked sample, the deviation between experiment and simulation observed in previous chapters is still present. For the dark annealed samples, the lower injection level $\Delta n_0 = N_A$ is the first time the fast decay during the first few nanoseconds is experimentally observed for the investigated samples in this work. This is in accordance to the predictions of strong charge separation effects at the p-n junction at low injection. This assumption was further tested by measuring TRPL after etching the CdS layer, which will be discussed later in this section. Although both samples were measured under the same injection levels, the effect of charge separation was not observed for the LS sample at $\Delta n_0 = N_A$. This result lies in contradiction to the prediction of charge separation being exclusively a function of injection level. This can be explained by considering the effect of field screening caused by the injected charge carriers, which is dependent on the width of the space charge region. This point will be further analyzed later in this chapter.

CdS/CIGSe junctions

In Fig. 4.9 the results of TRPL measurements and simulations of CdS/CIGSe p-n junctions at four different excitation powers ($P_{Laser} = 0.16, 0.45, 0.73, 2.0 \text{ mW}$) are presented. For injection levels $\Delta n_0 < N_A$ the LS sample presents a marked transition between a fast and a slow decay regime. This, although not observed at the same injection levels as in the DA sample, is still in accordance to the prediction of charge separation at the p-n junction. Especially at very low excitation and injection ($P_{Laser} = 0.16 \text{ mW}$, $\Delta n_0 = 0.1 \cdot N_A$) this effect is very strong both in experiments and simulations for the LS sample. The effect has thus been predicted and observed for samples with different doping concentrations. Additionally it has been shown to be dependent on the injection level, due to screening effects at high injection. However the dependence on injection level appears to not be the same for the different samples. Both simulations and experiments show that the

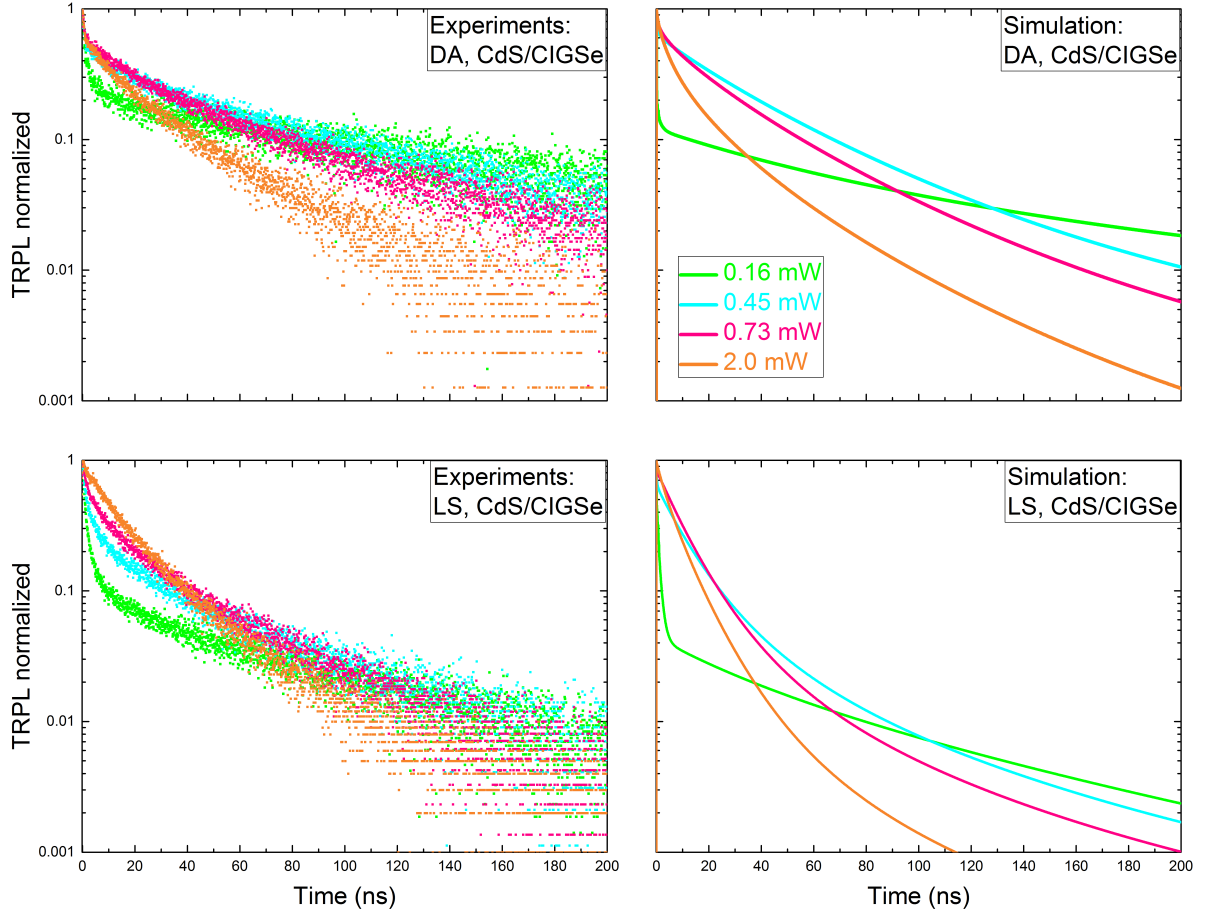


Figure 4.9: Results of experiments (left hand side, scattered) and simulation (right hand side, solid lines) of TRPL of CdS/CIGSe junctions at four different excitation powers ($P_{Laser} = 0.16, 0.45, 0.73$ and 2.0 mW). On the upper row the results for a dark annealed sample are presented, while the lower row contains the data for a light soaked sample.

effect of charge separation starts playing a role below a certain threshold of the injection level, with this threshold being dependent on the doping concentration of the sample. Further analysis of simulated physical quantities, especially of the spatial distribution of excited charge carrier, has been analyzed to understand this deviation between prediction and results. Again, the main point to consider here is the effect of field screening arising from the accumulation of injected charge carriers in the space charge region. For a more detailed explanation, see below.

CIGSe absorbers

To test whether the effect indeed comes from the presence of a p-n junction, TRPL measurements with bare CIGSe absorbers were carried out. The same excitation powers as for measurements of CdS/CIGSe junctions were used. The results of these measurements and the corresponding simulations are presented in Fig. 4.10. The calculated decay curves for both bare CIGSe absorbers deviate significantly from experiments. The reason for this could be that in the simulations no surface recombination was taken into account. This is a very strong assumption, since the role of the

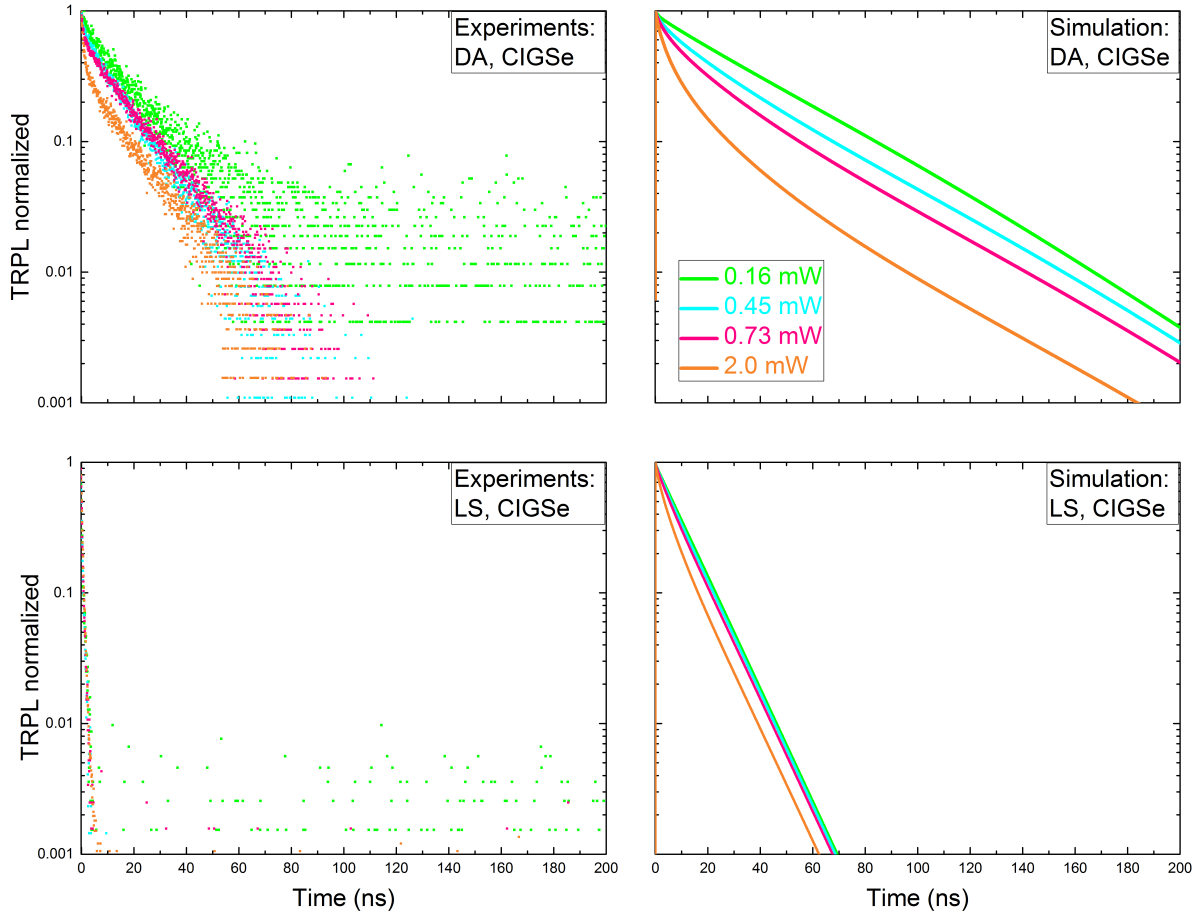


Figure 4.10: Results of experiments (left side, scattered) and simulation (right side, solid lines) of TRPL of bare CIGSe absorbers at four different excitation powers ($P_{Laser} = 0.16, 0.45, 0.73$ and 2.0 mW). On the upper row the results for a dark annealed sample are presented, while the lower row contains the data for a light soaked sample.

CdS layer is to passivate the surface of the CIGSe absorber. To arrive at a better agreement between experiments and simulation, the surface recombination velocity had to be adjusted individually for the different samples to the values $S_{0,DA} = 10 \text{ cm s}^{-1}$ and $S_{0,LS} = 10^4 \text{ cm s}^{-1}$. This is also a very large deviation between both samples, for which no clear explanation was found yet. Moreover, the LS sample shows an unexpectedly short decay lifetime in experiments of only a few nanoseconds. This could be due to recombination over shunts in the CIGSe absorber which were hinted at by the results of IV characterization.

Despite these problems, however, some results can still be obtained from the measurements and simulations of the bare DA absorbers. The first important result is that even at low injections, both simulations and experiments show no transition from fast to slow decay over the measuring time. Moreover, in experiments the decay goes from a mostly monoexponential to a bimolecular decay with increasing injection level, with no crossover between curves at low and high injection. This is in agreement with the simulated curves and corresponds to the predicted results. Thus, despite some strong deviations between experiments and simulations, a qualitative verification of the prediction has been achieved.

Field screening

It was previously observed that in contrast to predictions, the charge separation effects become dominant at different injection levels, depending on the doping densities of the samples. Metzger et al. have already mentioned this [76] but given no mathematical framework for this effect. Fafard et al. [93], Kuokstis et al. [94] and Cingolani et al. [95] have investigated in detail the screening of the electric field at the p-n junction of diodes caused by injection of charge carriers. They have reported that the strength of the screening field is directly proportional to the injected charge carrier density accumulated in the space charge region. Moreover, they have reported that the injection level necessary to counteract the intrinsic field is proportional to the width of the space charge region in the absorber. These characteristics are summarized in Eq. 4.7, which relates the total electric field in the space charge region F to the intrinsic field F_0 and the injected field caused by excited carriers F_i .

$$F = F_0 - F_i = F_0 - \frac{\rho_i q L_n}{\varepsilon_0 (\varepsilon_n L_p + \varepsilon_p L_n)} \quad (4.7)$$

As stated in Ref. [94], the intrinsic field F_0 is a constant that depends only on the charge carrier concentration of the absorber and of the buffer layer. On the other hand, the injected field F_i is dependent on the density of injected carriers ρ_i , the widths of the depletion regions in the charge carrier well, here corresponding to the absorber L_p , and in the barrier, here corresponding to the buffer layer L_n , and the respective relative permittivities of the layers ε_p , ε_n .

The density of photons absorbed after excitation is independent of the conditioning of the CIGSe samples, but the width of the space charge region is proportional to the square root of the doping concentration. Therefore the injection level necessary to generate a screening field strong enough to break the effect of charge carrier separation at the p-n junction changes depending on the doping concentration. Thus, the effect observed can be understood when thinking of the density of excited charge carrier in relation to the width of the space charge region. This means that, since the space charge region in the LS samples is narrower than in DA samples, a lower injection level is necessary to counteract the influence of charge carrier separation, which confirms the results seen in simulations and experiments.

To further illustrate the theoretical arguments presented here, Fig. 4.11 shows the spatial distribution of charge carriers a short time after excitation ($t_1 = 10$ ps and $t_2 = 1$ ns) at injection levels $\Delta n_0 = N_A$ and $\Delta n_0 = 2.8 \cdot N_A$. The charge carrier density at equilibrium is also plotted to help visualize the width of the space charge region. At high injection levels the density of excited electrons Δn_0 directly after excitation ($t_1 = 10$ ps) is larger than or in the same order of magnitude as the doping concentration, which has the same value as the hole density in equilibrium and far away from the space charge region. If additionally, Δn_0 is larger than the doping concentration over the entire width of the space charge region, the influence of charge carrier separation is suppressed (compare to Fig. 4.8). This is the case for the light soaked sample at high and intermediate injection levels as well as for DA samples at high injection.

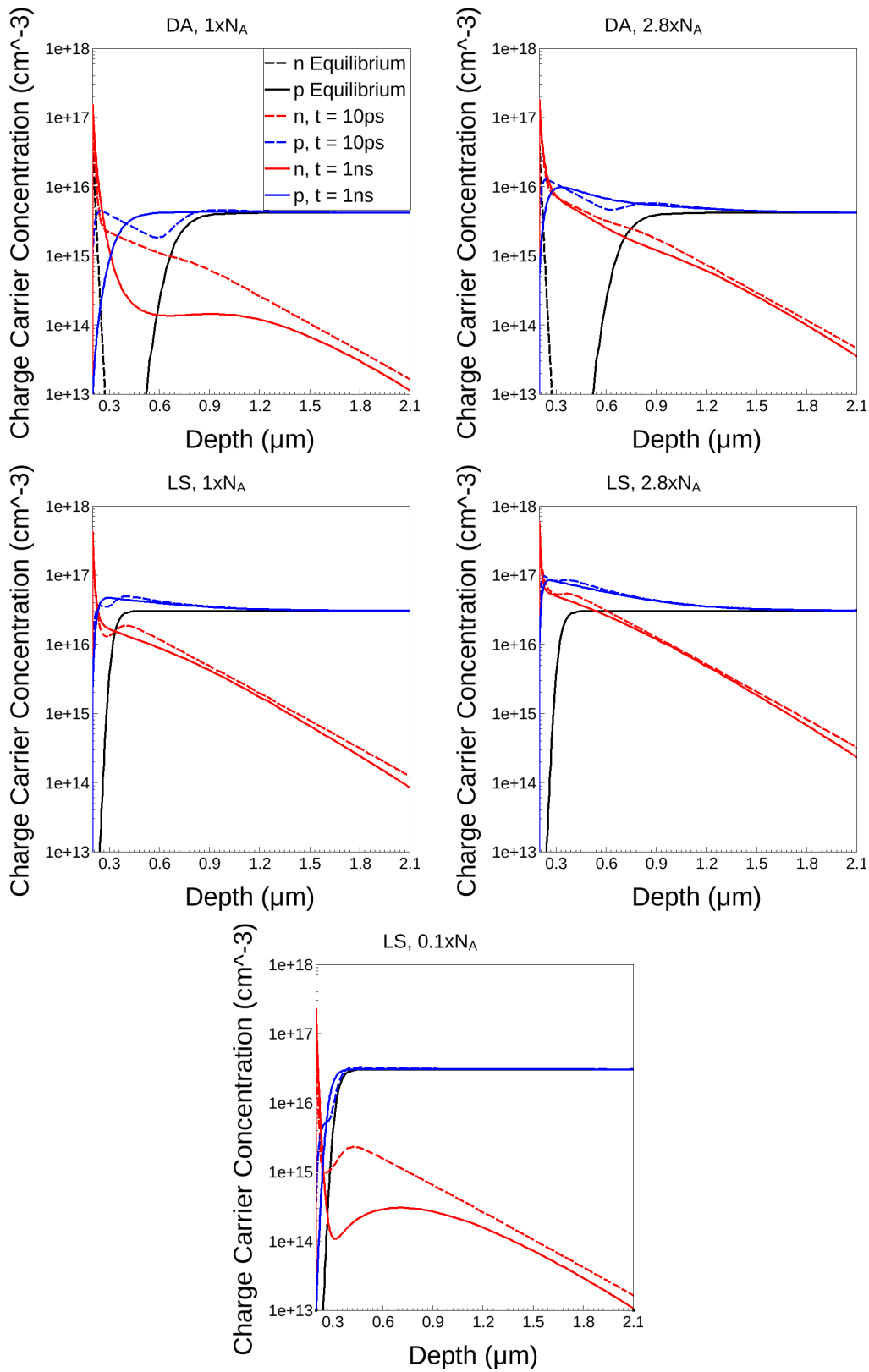


Figure 4.11: Spatial distribution of charge carrier densities after excitation. Electrons are shown in red, while holes in blue. Dashed colored lines show the densities 10 picoseconds after excitation, while solid colored lines correspond to 1 nanosecond after excitation. Electron densities in equilibrium conditions are presented as dashed black lines and hole densities in equilibrium conditions as solid black lines. Upper row: data for dark annealed samples at two different injection levels. On the left side is $\Delta n_0 = N_A$ and on the right side is $\Delta n_0 = 2.8 \cdot N_A$. Middle row: data for light soaked samples under the same injection levels. Lowest row: plot for the light soaked sample at low injection level $\Delta n_0 = 0.1 \cdot N_A$.

When the intrinsic field is thus screened by the injected charge carriers, the change in spatial distribution of n is also diminished, as seen in the graphs for n at $t_2 = 1$ ns. For the DA sample at injection level $\Delta n_0 = N_A$ the excited charge carriers are not enough to screen the intrinsic field and thus charge carrier separation occurs fast. Therefore in this case the distribution of electrons and holes changes significantly during the first nanosecond after excitation, as can be seen in Fig 4.11. For the light soaked sample a much lower injection level is necessary for the screening to be able to suppress charge carrier separation. As an example, a very low injection level ($\Delta n_0 = 0.1 \cdot N_A$) is shown in Fig. 4.11. There it can be seen that in such a case the excited carrier density is also too low to screen the intrinsic field and charge carrier separation happens very rapidly. However, this is not the case for the LS sample at higher injection levels ($\Delta n_0 = N_A$ and $\Delta n_0 = 2.8 \cdot N_A$). There, the screening of the field makes charge carrier separation much slower. Thus, the observed effects in simulations and experiments are explained by theory and the explanation provided is backed up by simulation.

One further point of discussion is the deviation between the results of Metzger et al. [76] and the ones presented in this work in regards to the influence of the CdS buffer layer as an effective partner for a p-n junction. In Ref. [76] the CdS/CIGSe junction is reported to have an electric field too weak to create any visible effects of charge carrier separation. However, in this work, the opposite has been observed in both simulations and experiments. The reasons for this are several. First, one of the main differences between both works is the doping density of the CdS layer, which was set to 10^{16} cm^{-3} by Metzger et al. [76], but is in the order of magnitude of 10^{17} cm^{-3} in this work. Moreover, the doping density of the p-type absorber was also set to a high value by Metzger et al. [76] ($2 \cdot 10^{16} \text{ cm}^{-3}$), which has been shown here to contain a very narrow space charge region and therefore need only a relative low injection level to screen the influence of charge separation.

From Fig. 4.12 it is also possible to recognize the reason for the difference between measurements of bare CIGSe absorbers and CdS/CIGSe junctions at high injection. Even though the field of the p-n junction is screened at sufficiently high injection, this does not mean that the material then behaves like the bare absorber. First, because of type inversion and band bending at the space charge region, the initial distribution of charge carriers after excitation in the CdS/CIGSe junction is still significantly different from what would be generated in a bare absorber. This difference in charge carrier densities over depth translates to their local product $n \cdot p$, which defines the rate of radiative recombination and thus the time development of PL emission. Additionally, the depth-dependent values of the quasi Fermi levels are also different between both cases. In the bare absorber there is no electric potential driving electrons towards the surface and counteracting their chemical potential. In the p-n junction however, as the charge carriers recombine over time, the intrinsic field of the junction is eventually left without screening and the effect of charge separation again plays a role, even if it is diminished. For all these reasons the measurement of bare absorbers and of CdS/CIGSe junctions at high injection are not directly comparable.

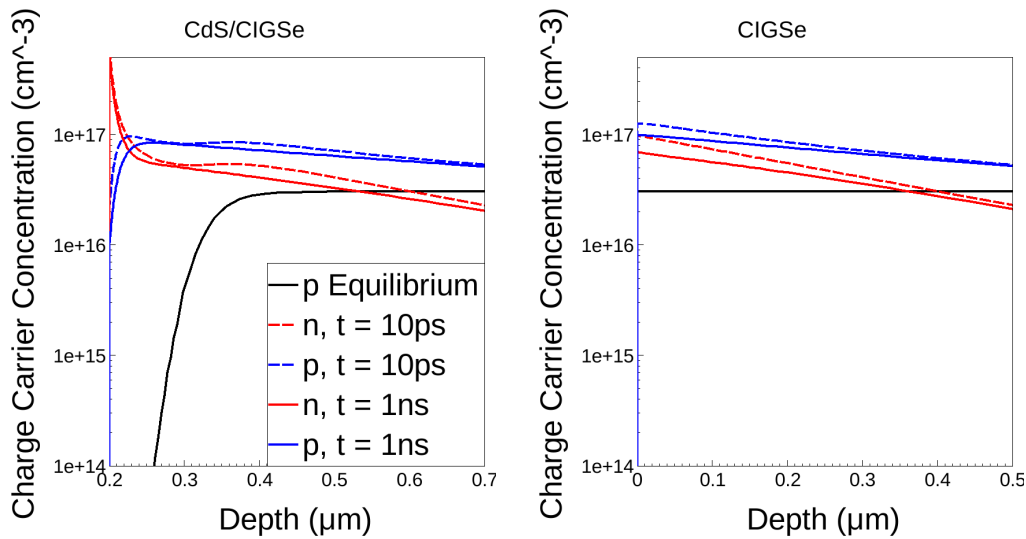


Figure 4.12: Spatial distribution of charge carrier densities in the absorber material after excitation (electrons red, holes blue) at high injection ($\Delta n_0 = 2.8 \cdot N_A$) and for short times after excitation (dashed lines 10 ps, solid lines 1 ns). The results are shown for a CdS/CIGSe junction (left) and a bare CIGSe absorber (right). The hole density in equilibrium is plotted as a solid black line. The data corresponds to the LS state.

Extraction of minority carrier lifetime

Despite the possibility of screening the intrinsic field at the CdS/CIGSe junction when measuring under high injection conditions, the question of correlation between PL decay lifetime measured and actual minority carrier lifetime remains open. In Ref. [88] the influence of the p-n junction and charge separation on TRPL measurements has been investigated for samples from the same producer as the ones investigated in this work. There it has been shown that the PL decay lifetimes at high injection still differ between measurements with or without CdS. Specifically, the PL decay has been measured to be faster in the pure absorber under high injection than in the CdS/CIGSe junction under the same injection conditions.

The reason for this behavior can be understood when thinking of the distribution of charge carriers in the region of the absorber close to its surface. In Fig. 4.12 the charge carrier densities up to a depth of 500 nm inside the absorber are plotted for two times shortly after excitation ($t_1 = 10$ ps and $t_2 = 1$ ns) at high injection ($\Delta n_0 = 2.8 \cdot N_A$) and for absorbers with and without CdS buffer layer. This plot shall help visualize the following discussion.

At a p-n junction, the area close to the interface is depleted. If the depletion of the space charge region is strong, i.e. if the doping of the n-region is high in relation to the doping of the p-region, then the hole density is significantly lower than the electron density, even after excitation. In the pure absorber the excited concentrations remain at values very close to each other, at least in the same order of magnitude. Meanwhile in a p-n junction the concentrations at the interface can differ by at least an order of magnitude, depending on the injection level. This means that in a strongly depleted space charge region, like the one presented in the samples investigated in this work and in Ref. [88], electrons at the surface of the absorber have fewer recombination partners at high injection

than electrons under the same conditions in a bare absorber. Therefore the radiative recombination rate at high injection in the p-n junction is reduced compared to the one in a bare absorber, since R_{rad} is dependent on the local product of the carrier concentrations $n \cdot p$. For applications this means that the true charge carrier lifetime of the bare absorber can only be approximated by the PL lifetime at high injection of CdS/CIGSe junctions if the depletion of the absorber in the space charge region is low, i.e. for low doping concentrations of the buffer layer.

Extraction of buffer layer doping

From the theoretical calculations presented in this section it is expected that a variation of injection level in TRPL measurements could be used to analytically obtain a value for the doping concentration of CdS layers. This is a parameter classically regarded as not experimentally available due to the very low thickness of the CdS layers used in CIGSe solar cells (< 100 nm). It is possible to achieve this thanks to the analytic expression for the field F inside the space charge region of CdS/CIGSe junctions under light-induced excitation (Eq. 4.7). This field is formulated as the sum of the intrinsic electric field F_0 and of the screening field induced by injected charge carriers F_i . Additionally, it shall be considered that the widths of the space charge region in each layer are related to one another by the quotient of their doping concentrations $N_{C,CdS}$ and $N_{A,CIGSe}$.

$$L_p = \frac{N_{D,CdS}}{N_{A,CIGSe}} L_n \quad (4.8)$$

By inserting Eq. 4.8 into Eq. 4.7 the strength of the screening field can also be related to the doping concentrations of the layers. The doping concentration of the CIGSe layer can be measured, while all the other information necessary to calculate the strength of the field can be extracted from the experimental conditions, except for the CdS doping. If an injection level variation is carried out until the point at which the effect of charge carrier separation disappears, it would then be possible to solve Eq. 4.7 for the doping concentration of the buffer layer. This corresponds to the point where F_0 and F_i cancel each other out. Such an analysis would permit to extract the doping density of the buffer layer from TRPL measurements. This method has been so far only theorized and must be experimentally tested on CdS/CIGSe heterojunctions. It must be kept in mind that the calculations presented here include strong assumptions and simplifications of the system. At this point the suitability of this method is proposed as the subject of future investigations.

4.3.4 Summary

A prediction was done based on the simulation model presented in previous sections. The simulation model predicted a strong influence of charge carrier separation on the TRPL curves of CdS/CIGSe layer stacks at low injection levels. TRPL measurements on such junctions were carried out to test this prediction. The expected behavior was found in samples with two distinct doping concentrations. Different from what was expected, the influence of charge carrier separation was not purely a function of injection level. As shown by Refs. [93–95], the effect comes from screening

of the intrinsic field at the p-n junction by injected charge carriers. These sources also show that the injection level necessary to screen the intrinsic field is dependent on the width of the space charge region. While the width of the space charge region of samples investigated in this work is dependent on their doping concentration, the density of absorbed photons is not. Therefore the same effect as stated in literature is observed here. Namely, the injection level necessary to suppress the effect of charge carrier separation is dependent on and decreases with doping concentration. Further verification of the effects predicted by the simulation model was achieved by measuring the TRPL decay of bare CIGSe absorbers.

The observation of carrier separation effects at CdS/CIGSe junctions contrasts with previous sources investigating the same effects for ZnO/CdS/CIGSe layer stacks [76], which claim that the field at the CdS/CIGSe junction is not sufficient to create visible charge carrier separation effects. This deviation from literature probably stems from the fact that here also relatively low injection levels and low doping concentrations of the CIGSe absorber were investigated and that the assumed doping concentration of the CdS buffer layers here is higher than in literature.

These results have several implications for the use of TRPL as a method to assess the material quality of CIGSe absorbers during production. While for bare absorbers the analytical interpretation of TRPL data is more reliable in low injection conditions, the opposite is true for the CdS/CIGSe junctions. However, with high injection further effects like bimolecular recombination start playing a role.

When TRPL measurements are carried out after production, the CdS buffer layer is often kept as a method to protect the CIGSe absorber from degradation and to passivate its surface. In this case additional information is necessary in order to interpret TRPL measurements correctly. Our simulations have shown that for CdS layers with high doping concentration or for CIGSe absorbers with low doping concentration, charge carrier separation effects can play a role even at intermediate injection levels, thus disturbing the results of TRPL analysis. This is because if the later and slower part of the PL decay is analyzed in these cases, the extracted lifetime is made artificially longer by the local separation of hole and electron concentrations along the depth of the absorber. Therefore the measured lifetime is not correctly correlated to the minority carrier recombination lifetime. For samples with high doping of the CIGSe material, e.g. light soaked samples, other problems may arise if low injection is measured. If the CdS buffer layer is present and highly doped, the effect of charge carrier separation is then very strong. Thus, it is recommended to measure on bare CIGSe absorbers whenever possible and if the use of CdS layers is necessary, then the effect of the p-n junction dependent on the injection level and doping concentration of the CdS and CIGSe layers must be taken into consideration.

Additionally it was found that the charge carrier lifetime of the bare absorber can be approximated by the PL decay lifetime of CdS/CIGSe junctions under high injection conditions only if the doping concentrations of the buffer layer is low, i.e. in the same order of magnitude as the absorber layer doping. For a much higher doping of the buffer layer, the depletion of the space charge region in the absorber leads to a strong difference in the density of holes and electrons at the interface. This has as a consequence a reduced rate of radiative recombination when compared

to that of the bare absorber under the same excitation conditions, since the local product $n \cdot p$ is strongly reduced in the space charge region.

A method of extraction for the doping concentration of thin CdS buffer layers has been proposed from simple theoretical considerations. This material parameter has so far been generally regarded as not experimentally available due to limitations by the thickness of the buffer layer. The method involves a variation of injection level in TRPL measurements of CdS/CIGSe junctions to find the point at which the intrinsic field of the junction and the field created by the excited charge carriers cancel out due to screening effects. Such a method is still to be tested and was derived from a strongly simplified model of the p-n junction.

4.4 General Discussion

In this section, further points of general discussion about the validity of the methods and results will be presented. These are aspects that affect all previous sections and have not been discussed in detail so far.

Lifetime extraction

As a method to extract lifetime values from simulated TRPL curves, the definitions of an instantaneous lifetime τ_{inst} according to Eq. (3.1) and of an asymptotic lifetime τ_{∞} from Eq. (3.2) were used. This method of analysis requires the data to be smooth, since the derivative of the PL intensity over time is calculated to extract τ_{inst} . However, this method has an important limitation regarding the analysis of experimental data, which inherently presents a noisy component which is more dominant towards the lower values of PL emission. Since the late part of the decay is the one of interest for the extraction of τ_{∞} , it becomes hard to extract reliable values for the asymptotic lifetime from experimental data directly. This is because the noise creates large fluctuations and spikes in the derivatives, from which τ_{inst} is calculated.

While this method is not easily applicable to experimental data, the theoretical considerations behind it point to the fact that τ_{∞} would in theory be the most suitable value to assign as PL lifetime if the goal is to obtain a value correlated to the minority carrier lifetime. This is because the evaluation of τ_{∞} foregoes effects that are only present in transient measurements, such as redistribution of the charge carriers after excitation, and focuses on the regime of PL decay that is not dominated by diffusion or drift but rather by trapping, emission and recombination. Therefore the instantaneous and asymptotic lifetime are still interesting quantities to consider and are definitely suitable to describe simulated TRPL decay curves of systems that are too complex to analytically approximate with a monoexponential, biexponential or bimolecular model. Especially for complex systems with multiple channels of non-radiative recombination, an analytical solution to the differential equation for the evolution of the charge carrier density over space and time is usually not known if the assumption of low injection level is discarded.

Some possibilities exist that would allow to test the analysis of experimental data via instantaneous lifetime. For this it would be necessary to smooth the data. Methods such as approximation of the data via a spline, i.e. a piecewise polynomial function that is also differentiable at all points, would help reduce noise and possibly yield reliable results. Another option would be to smooth the experimental data itself and cut out the noise by first applying a low pass frequency filter to it. This point is therefore of great interest and shall be further explored in future studies.

Molybdenum back contact

Some strong simplifications at the back contact of the absorber were made for simulations. Namely a perfectly conducting metallic contact was assumed, while also neglecting the possibility of formation of Schottky contacts between metal and semiconductor. This, of course, changes the

dynamics of charge carriers near the back contact. With the formation of a Schottky contact the bands of the semiconductor would bend near the back interface and this would either create a well or a barrier for electrons, while having the opposite effect for holes respectively. The direction of the band bending and the height of the Schottky barrier depend on the relation of the electron affinity of the semiconductor, the Fermi level of the metal and the distance of the Fermi level of the semiconductor to its conduction band [15].

From theory it would be expected that the presence of a back contact should have no significant effect on TRPL measurements. This is because of the exponential decay of the excitation profile over depth. This means that most charge carriers are generated and recombine at the front interface and only a very small fraction of the electrons ever reach the back contact. This is specially the case if the absorber is set to have a band gap grading like the one of the investigated samples. In such a sample, the influence of the bending at the back contact truly becomes negligible. This is the reason why the simplification of the system at the back interface for simulations was justified for TRPL simulations. IV and EQE simulations, however, might still be affected by band bending near the back surface even in absorbers with band gap grading.

Simulations of absorbers without a band gap grading and with a Schottky barrier at the back interface were carried out with the simulation model presented in this work and show that in such cases, the flow of electrons towards the metallic back contact has a strong influence on the simulated time-resolved PL decay. This is a sign that not all aspects of this subject have been understood and these simulation results should be compared to TRPL measurements of real absorbers without band gap grading. This shall also be the subject of future studies.

Lastly, a further simplification was made at the back surface of the absorber by neglecting the possibility of interface recombination. This plays only a negligible role in absorbers with band gap grading, as long as the recombination is calculated over a fixed velocity without the presence of charged defects. As soon as charged defects at the back interface are taken into account, the bending of the semiconductor bands changes and this could have a strong influence on simulated and measured TRPL curves. This, again, is an important subject for future investigations.

Dimensionality

All simulations presented in this work are done in a one-dimensional model. This by itself is a strong simplification of reality. Real CIGSe absorbers present lateral inhomogeneities in composition, defect density, band gap and electric potential, among others, which have a significant effect on PL yield and PL decay lifetime [53, 92, 96–100]. These fluctuations make two and even three dimensional simulations necessary to accurately describe the microscopic photoluminescence behavior of these thin-film solar cells. However, as discussed in previous chapters, the lateral inhomogeneities play a negligible role when the area of excitation in TRPL measurements is several orders of magnitude larger than the grain diameter of CIGSe, as is the case in the experimental setup used for this work. Similarly, the role of diffusion of charge carriers outwards from the center of excitation becomes negligible with increasing laser spot size. Nonetheless, future studies shall take the consequences of the one-dimensional simplification into account. Furthermore, it is an

interesting question how the PL decay lifetime measured with large spots relates to the PL lifetime of single grains, i.e. whether the macroscopic PL lifetime is constructed as an average of the PL lifetimes of single grains, or whether it is rather dominated by the shortest or longest lifetimes available among material grains. The theoretical calculations on this matter have been already presented by Maiberg et al. [53], while experimental evidence is still sparse. This would be a suggestion for a future topic of investigation and one that can only be supported by simulations in higher dimensions.

Free fitting parameters

Some material parameters used in this study are not experimentally available and their values had to be assumed to a similar order of magnitude as found in literature. These unmeasured parameters are most often taken as the free fitting parameters that must be adjusted to accurately reproduce the experimental results. Nonetheless, the values of fitting parameters were not chosen arbitrarily. Firstly, for any given simulation series, the values of the fitting parameters are kept constant for all experimental conditions and all samples measured or simulated. This is a significant difference of entirely free fitting parameters, which could be used to adjust every single curve separately. This adjustment of values for individual simulation runs is generally not done in this work, since the fitting parameters are not expected to be dependent on the sample conditioning or on the experimental conditions. The clearest examples of fitting parameters in this work are the doping concentration of the buffer layer and the capture cross sections of defects. Although the freedom to fit with three independent parameters could point to a lack of meaningful results from simulations, it must also be taken into account that a large number of different experiments have been simulated to increase the level of confidence on the obtained parameter set. The data reproduced present a variation of experimental methods, experimental conditions and of CIGSe material characteristics. With these variations, the space of possible parameter sets that accurately reproduce all experimental curves is greatly reduced. Moreover, the accuracy of the model was further tested by presenting a prediction, which was then confirmed by experiments. This means that even though the values of all parameters could not be determined with absolute accuracy, the correctness of the physical models in the simulation and the interpretations extracted from it have been sufficiently certified at multiples points.

5 Summary

In this work the first simulation model capable of accurately reproducing results of time-resolved photoluminescence measurements, as well as quantum efficiency spectra and current-voltage characteristics of thin film CIGSe solar cells is presented. This simulation model is used as a base to investigate the suitability of TRPL measurements to assess the material quality of CIGSe absorbers during production. The simulation model was additionally used to develop a deeper understanding of the physical processes playing a role in TRPL measurements.

A one dimensional simulation model of CIGSe absorbers was used. This model of the absorber includes a linear band gap grading, shallow defects near the conduction band and asymmetric capture cross sections at the defect states. The presence of front interface recombination but no back contact recombination and an idealized metallic back contact without a Schottky barrier are further characteristics of the model. Thermionic emission at the CdS/CIGSe interface, however, was taken into account. Absorption coefficients for the absorber were partly calculated based on measured band gap and composition gradient, and partly extracted from literature. The defect energy and concentration, doping density, as well as band gap, composition gradient and total depth of the absorber were taken from experimental data. Other parameters such as doping concentration and electron affinity of the CdS buffer layer were used as free fitting parameters, together with the capture cross sections of defects in the absorber.

From simple theoretical principles it was recognized that TRPL measurements can be interpreted in a significant manner only if a variation of the sample characteristics or the experimental conditions is carried out. Moreover, given the existence of free fitting parameters in the simulation model, simulations of experiments with varying condition and of samples with varying characteristics must be carried out. This is done with the goal to achieve a reasonable confidence on the values of the parameter set used.

The simulation model was first validated by reproducing the results of experiments of CdS/CIGSe junctions in two distinct states, namely dark annealed and light soaked, and under multiple experimental conditions. From literature it is known that these states differentiate themselves in their doping concentration and defect density and that these changes are reversible. It was found that the metastable changes in PL decay behavior seen in CIGSe absorber layers after treatment with heat and solar spectrum illumination stem mainly from the increased doping concentration. Furthermore, the observed change in defect density and energy have only a negligible effect on TRPL measurements.

The accuracy of model was further confirmed by reproducing TRPL measurements, IV characteristics and EQE spectra, all with the same parameter set. The model was then used to investigate the influence of individual material parameters on the open circuit voltage of complete cells and on the PL lifetime of bare CIGSe absorbers. The results show that open circuit voltage and PL lifetime positively correlate only when specific material parameters are changed, such as those directly influencing the rate of non-radiative SRH recombination. For the variation of other parameters such as the doping concentration, a negative correlation between V_{OC} and PL lifetime was observed. No correlation between these two quantities was found when parameters that only influence the initial redistribution of charge carriers after excitation were changed. This is because such parameters have no influence on the recombination lifetime of charge carriers. Examples of such parameters are the slope of the composition gradient and hole mobility. These results were compared to literature regarding the existence of a correlation between open circuit voltage and PL lifetime. It was recognized that besides the sources of lacking correlation recognized in literature, i.e. fluctuating defect densities, a fluctuation in band gap gradient during production could also lead to a lack of correlation. In conclusion to this topic, it was found that TRPL is suitable as a method of evaluation of solar cell efficiency only if the composition gradient is determined. For this reason, it is recommended that spectral analysis of TRPL results is added to the evaluation procedures to obtain the necessary information about composition gradient.

Predictions were made using the simulation model regarding the influence of p-n junctions on TRPL measurements. The prediction of accelerated PL decay at low injections was verified by experiments and was found to exist also in CdS/CIGSe junctions and not only in entire cell stacks. This stays in contrast to previous literature findings. This discrepancy may lie on the higher doping concentration of CdS layers investigated here when compared to those from similar works in literature. It was also found that charge carrier separation is not a direct function of injection level. Rather it was established that the necessary injection level to screen the intrinsic field at the p-n junction is dependent on the doping concentration. This is in accordance to literature regarding other types of p-n junctions such as diodes. From very simple theoretical considerations, a method to experimentally extracting the doping concentration of CdS buffer layers was proposed. The calculations for this method contain strong simplifications which are still to be tested regarding their validity for real CdS/CIGSe junctions.

In conclusion, it was found that the prediction of device efficiency from TRPL measurements requires additional information about the composition gradient of the absorber. This is because a difference in gradient significantly changes the open circuit voltage while leaving the PL lifetime unaffected. This is however only the case if no front contact gradient is used or, if it is present, if front interface recombination is negligible. Such information can be also obtained from TRPL measurements via variation of the detection and excitation wavelength [41]. Another finding was that in contrast to the investigation of bare absorbers, low injection conditions in TRPL measurements of CdS/CIGSe junctions can be detrimental to the extraction of minority charge carrier lifetime. With this, the main goals of a deeper understanding of the physical processes behind TRPL decays and of formulating an experimental method of charge carrier lifetime extraction capable of predicting device efficiency, were met.

Further topics of investigation are still open, which can use the simulation model established here as a basis. The influence of parameters fluctuations over the area of the absorber would be an interesting application for two dimensional simulations of the model. The effect of Schottky contacts at the back interface of the absorber with the metallic molybdenum back contact would also be a topic of interest. An evaluation of the suitability of the method proposed to extract the doping concentration of CdS buffer layers from TRPL measurements via variation of the injection level could have a deeper impact on the research community for this material.

Appendices

Appendix A - Optical Constants

The wavelength dependent complex refractive index of each material is divided into real part n and imaginary part k .

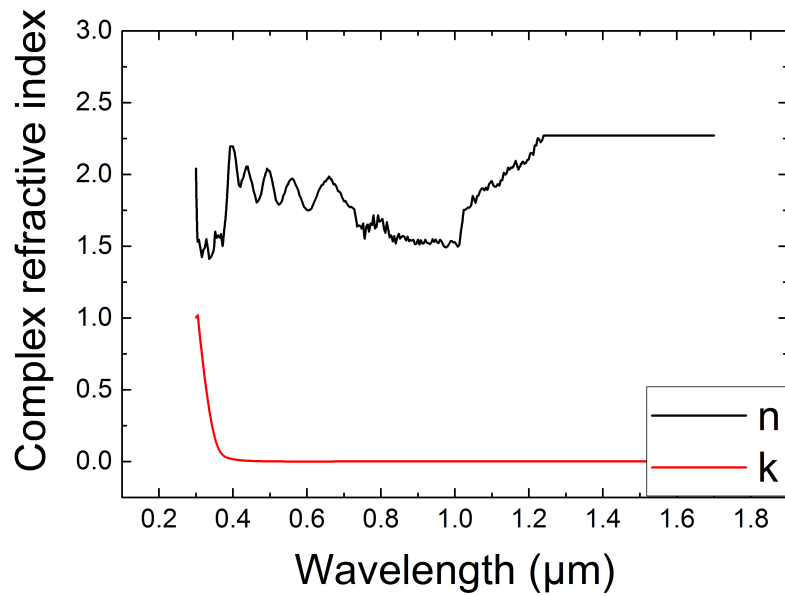


Figure 5.1: Optical constants ZnO

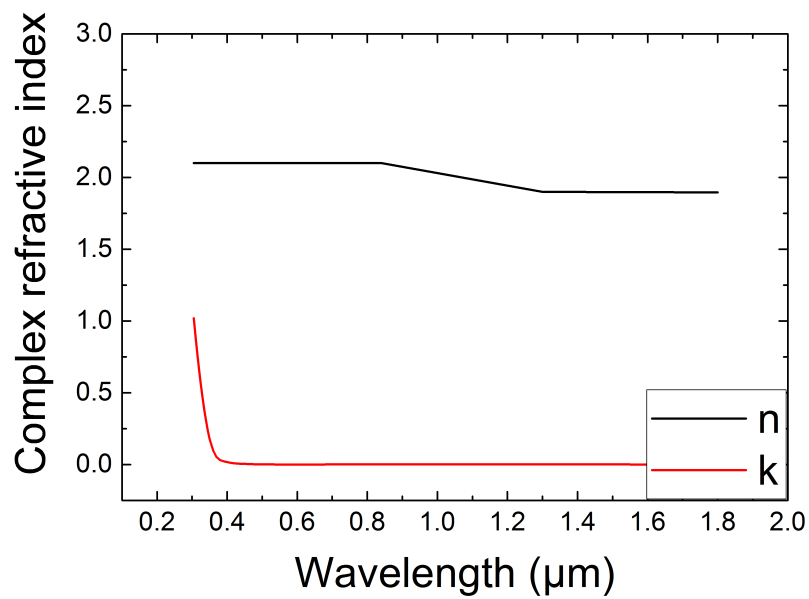


Figure 5.2: Optical constants i-ZnO

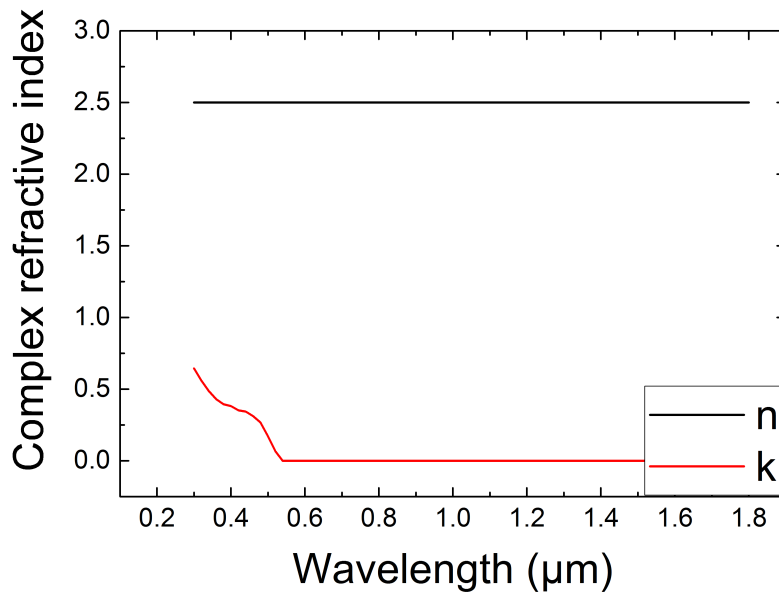


Figure 5.3: Optical constants CdS

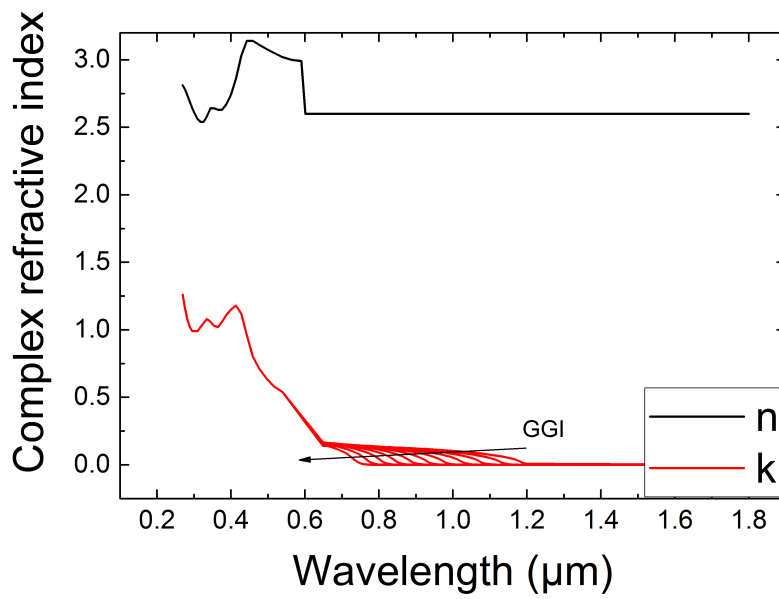


Figure 5.4: Optical constants CIGSe

Bibliography

- [1] Renewable Energy Policy Network for the 21st Century. Renewables 2016 global status report, 2017.
- [2] Bundesministerium für Wirtschaft und Energie. Erneuerbare Energien in Zahlen: Nationale und internationale Entwicklung im Jahr 2016, 2017.
- [3] M. J. De Wild-Scholten. Energy payback time and carbon footprint of commercial photovoltaic systems. *Solar Energy Materials and Solar Cells*, 119:296–305, 2013.
- [4] M. Powalla, S. Paetel, D. Hariskos, R. Wuerz, F. Kessler, P. Lechner, W. Wischmann, and T. M. Friedlmeier. Advances in cost-efficient thin-film photovoltaics based on Cu(In,Ga)Se₂. *Engineering*, 3:445–451, 2017.
- [5] V. M. Fthenakis. Overview of potential hazards. In *Practical Handbook of Photovoltaics: Fundamentals and Applications*. Elsevier Science, Oxford, 2003.
- [6] P. Jackson, R. Wuerz, D. Hariskos, E. Lotter, W. Witte, and M. Powalla. Effects of heavy alkali elements in Cu(In,Ga)Se₂ solar cells with efficiencies up to 22.6%. *Physica Status Solidi - Rapid Research Letters*, 10:583–586, 2016.
- [7] Solar Frontier. Press release: Solar Frontier’s CIS thin-film submodule achieves highest efficiency world record of 19.2%, http://www.solar-frontier.com/eng/news/2017/0227_press.html, accessed 29.01.2017.
- [8] M. A. Green, Y. Hishikawa, W. Warta, E. D. Dunlop, D. H. Levi, J. Hohl-Ebinger, and A. W.H. Ho-Baillie. Solar cell efficiency tables (version 50). *Progress in Photovoltaics: Research and Applications*, 25:668–676, 2017.
- [9] J. F. López Salas, S. J. Heise, M. Richter, V. Gerliz, M. S. Hammer, J. Ohland, and I. Hammer-Riedel. Simulation of metastable changes in time resolved photoluminescence of Cu(In,Ga)Se₂ thin film solar cells upon light soaking treatment. *Thin Solid Films*, 633:40–44, 2017.
- [10] J. F. López Salas, M. Richter, J. Parisi, and S. J. Heise. Simulation of photoluminescence lifetime and open-circuit voltage in Cu (In,Ga)Se₂ thin film solar cells. *Journal of Applied Physics*, 122:203103, 2017.

- [11] S. J. Heise, V. Gerliz, M. S. Hammer, J. Ohland, and J. Keller. Light-induced changes in the minority carrier diffusion length of Cu (In,Ga)Se₂ absorber material. *Solar Energy Materials & Solar Cells*, 163:270–276, 2017.
- [12] V. Gerliz. *Charakterisierung des metastabilen Verhaltens der Chalkopyritdünnschichtsolarzellen mit der zeitaufgelösten Photolumineszenzspektroskopie*. PhD thesis, University of Oldenburg, 2016.
- [13] P. Y. Yu and M. Cardona. *Fundamentals of Semiconductors: Physics and Materials Properties, 3rd Edition*. Springer-Verlag, Berlin Heidelberg, 2005.
- [14] P. Würfel. *Physics of Solar Cells: From Principles to New Concepts*. WILEY-VCH Verlag GmbH & Co. KGaA, Weinheim, 2007.
- [15] S. M. Sze and K. K. Ng. *Physics of Semiconductor Devices, Third Edition*. John Wiley & Sons, Inc., Hoboken, New Jersey, 2006.
- [16] J.W. Orton and P. Blood. *The Electrical Characterization of Semiconductors : Measurement of Minority Carrier Properties, Techniques of Physics 13*. Academic Press, London, 1990.
- [17] R. K. Ahrenkiel. *Minority-Carrier Lifetime in III-V Semiconductors, Semiconductors and Semimetals Vol. 39*. Academic Press, London, 1993.
- [18] W. Shockley and W. T. Read. Statistics of the recombination of holes and electrons. *Physical Review*, 87:835–842, 1952.
- [19] R. N. Hall. Electron-hole recombination in germanium. *Physical Review*, 87:387, 1952.
- [20] S. Siebentritt, M. Igalson, C. Persson, and S. Lany. The electronic structure of chalcopyrites - Bands, point defects and grain boundaries. *Progress in Photovoltaics: Research and Applications*, 18:390–410, 2010.
- [21] S. Siebentritt. Chalcopyrite compound semiconductors for thin film solar cells. *Current Opinion in Green and Sustainable Chemistry*, 4:1–7, 2017.
- [22] W. Shockley. On the surface states associated with a periodic potential. *Physical Review*, 56:317–323, 1939.
- [23] I. Tamm. Über eine mögliche Art der Elektronenbindung an Kristalloberflächen. *Zeitschrift für Physik*, 76:849–850, 1932.
- [24] A. Koprek, O. Cojocaru-Miredin, R. Wuerz, C. Freysoldt, B. Gault, and D. Raabe. Cd and impurity redistribution at the CdS/CIGS interface after annealing of CIGS-based solar cells resolved by atom probe tomography. *IEEE Journal of Photovoltaics*, 7:313–321, 2017.
- [25] D. Abou-Ras, S. S. Schmidt, R. Caballero, T. Unold, H. W. Schock, C. T. Koch, B. Schaffer, M. Schaffer, P. P. Choi, and Oana Cojocaru-Mirédin. Confined and chemically flexible grain boundaries in polycrystalline compound semiconductors. *Advanced Energy Materials*, 2:992–998, 2012.

- [26] M. Powalla, M. Cemernjak, J. Eberhardt, F. Kessler, R. Kniese, H. D. Mohring, and B. Dimmler. Large-area CIGS modules: Pilot line production and new developments. *Solar Energy Materials and Solar Cells*, 90:3158–3164, 2006.
- [27] N. Kohara, S. Nishiwaki, Y. Hashimoto, T. Negami, and T. Wada. Electrical properties of the Cu(In,Ga)Se₂/MoSe₂/Mo structure. *Solar Energy Materials and Solar Cells*, 67:209–215, 2001.
- [28] T. Wada, N. Kohara, S. Nishiwaki, and T. Negami. Characterization of the Cu(In,Ga)Se₂/Mo interface in CIGS solar cells. *Thin Solid Films*, 387:118–122, 2001.
- [29] T. Eisenbarth, T. Unold, R. Caballero, C. A. Kaufmann, and H. W. Schock. Interpretation of admittance, capacitance-voltage, and current-voltage signatures in Cu(In,Ga)Se₂ thin film solar cells. *Journal of Applied Physics*, 107:034509, 2010.
- [30] M. Igalson, A. Urbaniak, K. Macielak, M. Tomassini, N. Barreau, and S. Spiering. Barriers for current transport in CIGS structures. *Proceedings of the 2011 IEEE 37th Photovoltaic Specialists Conference*, pages 002727–002731, 2011.
- [31] N. Neugebohrn, M. S. Hammer, J. Neerken, J. Parisi, and I. Riedel. Analysis of the back contact properties of Cu(In,Ga)Se₂ solar cells employing the thermionic emission model. *Thin Solid Films*, 582:332–335, 2015.
- [32] R. Scheer and H. W. Schock. *Chalcogenide Photovoltaics: Physics, Technologies, and Thin Film Devices*. WILEY-VCH Verlag GmbH & Co. KGaA, Weinheim, 2011.
- [33] M. Turcu, I. M. Kötschau, and U. Rau. Composition dependence of defect energies and band alignments in the Cu(In_{1-x}Ga_x)(Se_{1-y}S_y)₂ alloy system. *Journal of Applied Physics*, 91:1391–1399, 2002.
- [34] B. L. Williams, V. Zardetto, B. Kniknie, M. A. Verheijen, W. M.M. Kessels, and M. Creatore. The competing roles of i-ZnO in Cu(In,Ga)Se₂ solar cells. *Solar Energy Materials and Solar Cells*, 157:798–807, 2016.
- [35] S. Ishizuka, K. Sakurai, A. Yamada, K. Matsubara, P. Fons, K. Iwata, S. Nakamura, Y. Kimura, T. Baba, H. Nakanishi, T. Kojima, and S. Niki. Fabrication of wide-gap Cu(In_{1-x}Ga_x)Se₂ thin film solar cells: a study on the correlation of cell performance with highly resistive i-ZnO layer thickness. *Solar Energy Materials and Solar Cells*, 87:541–548, 2005.
- [36] M. N. Ruberto and A. Rothwarf. Time-dependent open-circuit voltage in CuInSe₂/CdS solar cells: Theory and experiment. *Journal of Applied Physics*, 61:4662, 1987.
- [37] M. Igalson and H. W. Schock. The metastable changes of the trap spectra of CuInSe₂-based photovoltaic devices. *Journal of Applied Physics*, 80:5765–5769, 1996.

- [38] R. Herberholz, U. Rau, H. W. Schock, T. Haalboom, F. Ernst, C. Beilharz, K. W. Benz, and D. Cahen. Phase segregation, Cu migration and junction formation in Cu(In,Ga)Se₂. *The European Physical Journal Applied Physics*, 6:131–139, 1999.
- [39] V. Nadazdy, M. Yakushev, E.H. Djebbar, A.E. Hill, and R.D. Tomlinson. Switching of deep levels in CuInSe₂ due to electric field-induced Cu ion migration. *Journal of Applied Physics*, 84:4322, 1998.
- [40] S. Lany and A. Zunger. Light- and bias-induced metastabilities in Cu(In,Ga)Se₂ based solar cells caused by the (V_{Se} - V_{Cu}) vacancy complex. *Journal of Applied Physics*, 100:113725, 2006.
- [41] D. Kuciauskas, Jian V. Li, M. A. Contreras, J. Pankow, P. Dippo, M. Young, L. M. Mansfield, R. Noufi, and D. Levi. Charge carrier dynamics and recombination in graded band gap CuIn_{1-x}Ga_xSe₂ polycrystalline thin-film photovoltaic solar cell absorbers. *Journal of Applied Physics*, 114:1–6, 2013.
- [42] M. Maiberg, T. Hölscher, S. Zahedi-Azad, and R. Scheer. Theoretical study of time-resolved luminescence in semiconductors. III. Trap states in the band gap. *Journal of Applied Physics*, 118:105701, 2015.
- [43] W. K. Metzger, I. L. Repins, and M. A. Contreras. Long lifetimes in high-efficiency Cu(In,Ga)Se₂ solar cells. *Applied Physics Letters*, 93:022110, 2008.
- [44] D. Kuciauskas, J. V. Li, A. Kanevce, H. Guthrey, M. Contreras, J. Pankow, P. Dippo, and K. Ramanathan. Charge-carrier dynamics in polycrystalline thin-film CuIn_{1-x}Ga_xSe₂ photovoltaic devices after pulsed laser excitation: Interface and space-charge region analysis. *Journal of Applied Physics*, 117:185102, 2015.
- [45] M. Maiberg, C. Spindler, E. Jarzembowski, and R. Scheer. Electrical characterization of Cu(In,Ga)Se₂-solar cells by voltage dependent time-resolved photoluminescence. *Thin Solid Films*, 582:379–382, 2015.
- [46] M. Maiberg and R. Scheer. Theoretical study of time-resolved luminescence in semiconductors. II. Pulsed excitation. *Journal of Applied Physics*, 116:123711, 2014.
- [47] R. K. Ahrenkiel and J. Dashdorj. Interface recombination velocity measurement by a contactless microwave technique. *Journal of Vacuum Science & Technology B: Microelectronics and Nanometer Structures*, 22:2063, 2004.
- [48] Y. D. Jho, J. S. Yahng, E. Oh, and D. S. Kim. Field-dependent carrier decay dynamics in strained In_xGa_{1-x}N/GaN quantum wells. *Physical Review B*, 66:035334, 2002.
- [49] P. Jackson, D. Hariskos, R. Wuerz, O. Kiowski, A. Bauer, T. M. Friedlmeier, and M. Powalla. Properties of Cu(In,Ga)Se₂ solar cells with new record efficiencies up to 21.7%. *Physica Status Solidi (RRL) - Rapid Research Letters*, 9:28–31, 2015.

- [50] G. Sozzi, S. Di Napoli, R. Menozzi, R. Carron, E. Avancini, B. Bissig, S. Buecheler, and A. N. Tiwari. Analysis of Ga grading in CIGS absorbers with different Cu content. *Proceedings of the 2016 IEEE 43rd Photovoltaic Specialists Conference*, pages 2279–2282, 2016.
- [51] S. H. Wei and A. Zunger. Band offsets at the CdS/CuInSe₂ heterojunction. *Applied Physics Letters*, 63:2549–2551, 1993.
- [52] S. J. Heise, V. Gerliz, M. S. Hammer, J. Ohland, J. Keller, and I. Hammer-Riedel. Light-induced changes in the minority carrier diffusion length of Cu(In,Ga)Se₂ absorber material. *Solar Energy Materials and Solar Cells*, 163:270–276, 2017.
- [53] M. Maiberg, F. Bertram, M. Müller, and R. Scheer. Theoretical study of time-resolved luminescence in semiconductors. IV. Lateral inhomogeneities. *Journal of Applied Physics*, 121:085703, 2017.
- [54] Spectra Physics Inc. Vanguard 532-2000 user guide, 2014.
- [55] Spectra Physics Inc. Model 375 dye laser with mode 376 dye circulator, instruction manual, 1979.
- [56] Sirah Lasertechnik GmbH. <http://www.sirah.com/dyes-accessories/laser-dyes-532-nm/dcm>, accessed 22.12.2017.
- [57] U. Rau and H. W. Schock. Chapter 6: Cu(In,Ga)Se₂ and related solar cells. In *Series on Photoconversion of Solar Energy - Vol 4: Clean Electricity From Photovoltaics, Second Edition*. Imperial College Press, London, 2015.
- [58] Spectra Physics Inc. Model 344s cavity dumper and model 454 cavity dumper driver, 1979.
- [59] J. P. Heritage and R. K. Jain. Subpicosecond pulses from a tunable cw mode-locked dye laser. *Applied Physics Letters*, 32:101–103, 1978.
- [60] S. Shirakata and T. Nakada. Time-resolved photoluminescence in Cu(In,Ga)Se₂ thin films and solar cells. *Thin Solid Films*, 515:6151–6154, 2007.
- [61] B. Ohnesorge, R. Weigand, G. Bacher, A. Forchel, W. Riedl, and F. H. Karg. Minority-carrier lifetime and efficiency of Cu(In,Ga)Se₂ solar cells. *Applied Physics Letters*, 73:1224–1226, 1998.
- [62] S. i. Shimakawa, K. Kitani, S. Hayashi, T. Satoh, Y. Hashimoto, Y. Takahashi, and T. Negami. Characterization of Cu(In,Ga)Se₂ thin films by time-resolved photoluminescence. *Physica Status Solidi (a)*, 203:2630–2633, 2006.
- [63] Spectra Physics Inc. Model 409 autocorrelator instruction manual, 1980.
- [64] Wolfgang Becker. *The bh TCSPC handbook, sixth edition*. Becker & Hickl GmbH, Berlin, 2014.

- [65] T. Kirchartz, K. Ding, and U. Rau. Chapter 2: Fundamental electrical characterization of thin-film solar cells. In *Advanced Characterization Techniques for Thin Film Solar Cells*. Wiley-VCH Verlag GmbH & Co. KGaA., Weinheim, 2011.
- [66] J. Nelson. *The Physics of Solar Cells*. Imperial College Press, London, 2003.
- [67] J. Heath and P. Zabierowski. Chapter 4: Capacitance Spectroscopy of Thin-Film Solar Cells. In *Advanced Characterization Techniques for Thin Film Solar Cells: Second Edition*. Weinheim, 2016.
- [68] R. Scheer, A. Pérez-Rodríguez, and W. K. Metzger. Advanced diagnostic and control methods of processes and layers in CIGS solar cells and modules. *Progress in Photovoltaics: Research and Applications*, 18:467–480, 2010.
- [69] C. Frisk, C. Platzer-Björkman, J. Olsson, P. Szaniawski, J. T. Wätjen, V. Fjällström, P. Salomé, and M. Edoff. Optimizing Ga-profiles for highly efficient Cu(In, Ga)Se₂ thin film solar cells in simple and complex defect models. *Journal of Physics D: Applied Physics*, 47:485104, 2014.
- [70] F. Wan, F. Tang, H. Xue, W. Lu, Y. Feng, and Z. Rui. Effects of defect states on the performance of CuInGaSe₂ solar cells. *Journal of Semiconductors*, 35:1–6, 2014.
- [71] Synopsys Inc. <https://www.synopsys.com/silicon/tcad.html>, accessed 22.12.2017.
- [72] M. Burgelman, P. Nollet, and S. Degraeve. Modelling polycrystalline semiconductor solar cells. *Thin Solid Films*, 361:527–532, 2000.
- [73] R. Brüggemann. SC-Simul, <http://www.greco.uni-oldenburg.de/26446.html>, accessed 15.05.2017.
- [74] S. Fonash, J. Arch, J. Cuiffi, J. Hou, W. Howland, P. McElheny, A. Moquin, M. Rogosky, F. Rubinelli, T. Tran, and H. Zhu. <http://www.ampsmodeling.org/>, accessed 22.12.2017.
- [75] R. Varache, C. Leendertz, M.E. Gueunier-Farret, J. Haschke, D. Muñoz, and L. Korte. Investigation of selective junctions using a newly developed tunnel current model for solar cell applications. *Solar Energy Materials and Solar Cells*, 141:14–23, 2015.
- [76] W. K. Metzger, I. L. Repins, M. Romero, P. Dippo, M. Contreras, R. Noufi, and D. Levi. Recombination kinetics and stability in polycrystalline Cu(In,Ga)Se₂ solar cells. *Thin Solid Films*, 517:2360–2364, 2009.
- [77] M. Maiberg and R. Scheer. Theoretical study of time-resolved luminescence in semiconductors. I. Decay from the steady state. *Journal of Applied Physics*, 116:123710, 2014.
- [78] Synopsys Inc. Sentaurus Device user guide, version J-2014.09, 2014.
- [79] Synopsys Inc. Sentaurus Device user guide, version L-2016.03, 2016.

- [80] J. Keller. *Charakterisierung und Simulation von sequentiell prozessierten CIGSSe-Solarzellen mit chemisch gradierter Absorberschicht Möglichkeiten und Einschränkungen eines eindimensionalen Ansatzes*. PhD thesis, University of Oldenburg, 2012.
- [81] M. Richter. *Electro-Optical Modeling and Simulation of Cu(In,Ga)(Se,S)₂ Thin-Film Solar Cells*. PhD thesis, University of Oldenburg, 2014.
- [82] M. Richter, C. Schubbert, P. Eraerds, I. Riedel, J. Keller, J. Parisi, T. Dalibor, and A. Avellán-Hampe. Optical characterization and modeling of Cu(In,Ga)(Se,S)₂ solar cells with spectroscopic ellipsometry and coherent numerical simulation. *Thin Solid Films*, 535:331–335, 2013.
- [83] M. Richter, C. Schubbert, P. Eraerds, J. Parisi, I. Riedel, T. Dalibor, and J. Palm. Comprehensive simulation model for Cu(In,Ga)(Se,S)₂ solar cells. *Solar Energy Materials and Solar Cells*, 132:162–171, 2015.
- [84] M. Richter, I. Riedel, C. Schubbert, P. Eraerds, J. Parisi, T. Dalibor, and J. Palm. Simulation study of the impact of interface roughness and void inclusions on Cu(In,Ga)(Se,S)₂ solar cells. *Physica Status Solidi (A) Applications and Materials Science*, 212:298–306, 2015.
- [85] P. D. Paulson, R. W. Birkmire, and W. N. Shafarman. Optical characterization of CuIn_{1-x}Ga_xSe₂ alloy thin films by spectroscopic ellipsometry. *Journal of Applied Physics*, 94:879–888, 2003.
- [86] F. Urbach. The long-wavelength edge of photographic sensitivity and of the electronic absorption of solids. *Physical Review*, 92:1324, 1953.
- [87] J. T. Heath, J. D. Cohen, and W. N. Shafarman. Bulk and metastable defects in CuIn_{1-x}Ga_xSe₂ thin films using drive-level capacitance profiling. *Journal of Applied Physics*, 95:1000–1010, 2004.
- [88] S. J. Heise and J. F. López Salas. Charge separation effects in time-resolved photoluminescence of Cu(In,Ga)Se₂ thin film solar cells. *Thin Solid Films*, 633:35–39, 2017.
- [89] O. von Roos and P. T. Landsberg. Effect of recombination on the open circuit voltage of a silicon solar cell. *Journal of applied physics*, 57:4746–4751, 1985.
- [90] I. L. Repins, W. K. Metzger, C. L. Perkins, J. V. Li, and M. A. Contreras. Correlation between measured minority-carrier lifetime and C(In, Ga)Se₂ device performance. *IEEE Transactions on Electron Devices*, 57:2957–2963, 2010.
- [91] I. L. Repins, B. Egaas, L. M. Mansfield, M. A. Contreras, C. P. Muzzillo, C. Beall, S. Glynn, J. Carapella, and D. Kuciauskas. Fiber-fed time-resolved photoluminescence for reduced process feedback time on thin-film photovoltaics. *Review of Scientific Instruments*, 86:013907, 2015.

- [92] M. Maiberg, T. Hölscher, E. Jarzembowski, S. Hartnauer, S. Zahedi-Azad, W. Fränzel, and R. Scheer. Verification of minority carrier traps in $\text{Cu}(\text{In,Ga})\text{Se}_2$ and $\text{Cu}_2\text{ZnSnSe}_4$ by means of time-resolved photoluminescence. *Thin Solid Films*, 633:208–212, 2017.
- [93] S. Fafard, E. Fortin, and J. L. Merz. Excitation-intensity-dependent photoluminescence quenching due to electric-field screening by photocarriers captured in single-quantum-well structures. *Physical Review B*, 48:11062–11066, 1993.
- [94] E. Kuokstis, C. Q. Chen, M. E. Gaevski, W. H. Sun, J. W. Yang, G. Simin, M. Asif Khan, H. P. Maruska, D. W. Hill, M. C. Chou, J. J. Gallagher, and B. Chai. Polarization effects in photoluminescence of C- and M-plane GaN/AlGaN multiple quantum wells. *Applied Physics Letters*, 81:4130–4132, 2002.
- [95] R. Cingolani, A. Botchkarev, H. Tang, H. Morkoç, G. Traetta, G. Coli, M. Lomascolo, A. Di Carlo, F. D. Sala, and P. Lugli. Spontaneous polarization and piezoelectric field in GaN/Al_{0.15}Ga_{0.85}N quantum wells: Impact on the optical spectra. *Physical Review B*, 61:2712, 2000.
- [96] D. Eich, U. Herber, U. Groh, U. Stahl, C. Heske, M. Marsi, M. Kiskinova, and W. Riedl. Lateral inhomogeneities of $\text{Cu}(\text{In,Ga})\text{Se}_2$ absorber films. 362:258–262, 2000.
- [97] S. A. Schumacher, J. R. Botha, and V. Alberts. Photoluminescence study of potential fluctuations in thin layers of $\text{Cu}(\text{In}_{0.75}\text{Ga}_{0.25})(\text{S}_y\text{Se}_{1-y})_2$. *Journal of Applied Physics*, 99:063508, 2006.
- [98] L. Gütay and G. H. Bauer. Lateral variations of optoelectronic quality of $\text{Cu}(\text{In}_{1-x}\text{Ga}_x)\text{Se}_2$ in the submicron-scale. *Thin Solid Films*, 487:8–13, 2005.
- [99] G. H. Bauer and L. Gütay. Lateral features of $\text{Cu}(\text{In}_{0.7}\text{Ga}_{0.3})\text{Se}_2$ -heterodiodes in the μm -scale by confocal luminescence and focused light beam induced currents. *Thin Solid Films*, 515:6127–6131, 2007.
- [100] I. L. Repins, L. Mansfield, A. Kanevce, S. A. Jensen, D. Kuciauskas, S. Glynn, T. Barnes, W. Metzger, J. Burst, C. S. Jiang, P. Dippo, S. Harvey, G. Teeter, C. Perkins, B. Egaas, A. Zakutayev, J. H. Alsmeier, T. Lusky, L. Korte, R. G. Wilks, M. Bar, Y. Yan, S. Lany, P. Zawadzki, J. S. Park, and S. Wei. Wild band edges: The role of bandgap grading and band-edge fluctuations in high-efficiency chalcogenide devices. *Proceedings of the 2016 IEEE 43rd Photovoltaic Specialists Conference*, 2016-Novem:309–314, 2016.

Publications

- **J.F. López Salas**, S.J. Heise, M. Richter, V. Gerliz, M.S. Hammer, J. Ohland, I. Hammer-Riedel. Simulation of metastable changes in time-resolved photoluminescence of Cu(In,Ga)Se₂ thin film solar cells upon light soaking treatment. *Thin Solid Films* 633:40-44, 2017
- **J.F. López Salas**, M. Richter, S.J. Heise, J. Parisi. Simulation of photoluminescence lifetime and open circuit voltage in Cu(In,Ga)Se₂ thin film solar cells. *Journal of Applied Physics* 122:203103, 2017
- S.J. Heise, **J.F. López Salas**. Charge separation effects in time-resolved photoluminescence of Cu(In,Ga)Se₂ thin film solar cells. *Thin Solid Films* 633:35-39, 2017
- Ö. Demircioglu, **J.F. López Salas**, G. Rey, T.P. Weiss, M. Mousel, A. Redinger, S. Siebentritt, J. Parisi, L. Gütay. Optical properties of Cu₂ZnSnSe₄ thin films and identification of secondary phases by spectroscopic ellipsometry. *Optics Express* 25:5327, 2017
- A. Neumüller, O.Sergeev, S.J. Heise, S. Bereznev, O. Volobujeva, **J.F. López Salas**, M. Vehse, C. Agert. Improved amorphous silicon passivation layer for heterojunction solar cells with post-deposition plasma treatment. *Nano Energy* 43:228-235, 2017

Danksagung

An dieser Stelle möchte ich mich bei allen Menschen bedanken, die mir während meiner Promotion und bei der Erstellung dieser Arbeit geholfen haben. Ich möchte mich auch bei all denen bedanken, die mich allgemein im Studium oder während meines Aufenthaltes in Deutschland unterstützt haben. Insbesondere bedanke ich mich bei:

- Prof. Dr. Jürgen Parisi für die Möglichkeit bei der EHF meine Doktorarbeit zu schreiben sowie für seine Betreuung
- Dr. Stephan Heise für seine intensive Betreuung, die vielen, hilfreichen Besprechungen und die freundliche Arbeitsatmosphäre
- Dr. Michael Richter ebenfalls für seine Betreuung und unverzichtbare Unterstützung bei den Simulationen
- der Firma Manz AG für die Bereitstellung von Probenmaterial
- Dr. Jörg Ohland für seine Unterstützung im Labor, für das Korrekturlesen und für die entspannten Diskussionen über fachliche, persönliche und soziopolitische Themen
- Dr. Levent Gütay für das Korrekturlesen und dafür, dass er immer für eine gute Stimmung in der Arbeitsgruppe sorgt
- Dr. Viktor Gerliz für die Unterstützung in der Anfangsphase meiner Promotion
- Dirk Otteken für die Hilfe im Labor und die netten Gespräche
- allen weiteren Mitgliedern der EHF-Gruppe, mit denen ich schöne Film- oder Spielabende verbracht habe
- meinen Eltern, Geschwistern und meiner Freundin Jasmine Horter für ihre Liebe und Unterstützung
- Leilany und Oliver Wirkner, weil ich bei ihnen immer eine offene Tür und unschätzbare Hilfe gefunden habe. Ohne sie wären meine ersten Jahre in Deutschland viel schwieriger gewesen.

Agradecimientos

Deseo agradecerles a todas las personas que me ayudaron durante el doctorado y a la hora de escribir esta tesis. También le agradezco a todos aquellos que en general me dieron su apoyo durante mis estudios y mi estadía en Alemania. Especialmente le agradezco a:

- Prof. Dr. Jürgen Parisi por la posibilidad de escribir mi tesis de doctorado en la EHF y por su supervisión
- Dr. Stephan Heise por su supervisión conitnua, los numerosos y productivos diálogos y por la atmósfera de trabajo tan amigable
- Dr. Michael Richter también por su supervisión y por su ayuda invaluable en las simulaciones
- la compañía Manz AG por proveer el material para la investigación
- Dr. Jörg Ohland por su apoyo en el laboratorio, por leer y corregir esta tesis y por las relajadas discusiones acerca de temas técnicos, personales y sociopolíticos
- Dr. Levent Gütay por leer y corregir la tesis y por mantener los buenos ánimos del grupo
- Dr. Viktor Gerliz por su apoyo durante la fase inicial de mi doctorado
- Dirk Otteken por la yuda en el laboratorio y las conversaciones amenas
- todos los miembros del grupo EHF con quienes pude pasar tardes agradables jugando o viendo películas
- mis padres, hermanos, sobrinos y mi novia Jasmine Horter por su amor y apoyo
- Leilany und Oliver Wirkner por simepre recibirme con puertas abiertas. Sin ellos mis primeros años en Alemania hubieran sido mucho más difíciles.

Erklärung

Hiermit versichere ich, dass ich diese Arbeit selbständig verfasst und keine anderen als die angegebenen Quellen und Hilfsmittel benutzt habe. Außerdem versichere ich, dass ich die allgemeinen Prinzipien wissenschaftlicher Arbeit und Veröffentlichung, wie sie in den Leitlinien guter wissenschaftlicher Praxis der Carl von Ossietzky Universität Oldenburg festgelegt sind, befolgt habe.

Oldenburg, 24.04.2018
José Fabio López Salas

Curriculum Vitae

José Fabio López Salas

Geboren am 14. September 1990
in San José, Costa Rica

Promotion (Physik)
10/2014 - 04/2018 Carl-von-Ossietzky Universität Oldenburg
Abteilung Energie und Halbleiterforschung
Titel der Dissertation: “Modellierung und Simulation der
Rekombinationsdynamik in Cu(In,Ga)(Se)_2 Dünnschichtsolarzellen”

Masterstudium (M.Sc. Physik)
10/2012 - 09/2014 Carl-von-Ossietzky Universität Oldenburg
Titel der Masterarbeit: “Vergleichsstudie unterschiedlicher Methoden zur
Extraktion der Diodenparameter von Chalkopyrit-Solarzellen”
Gefördert durch den Deutschen Akademischen Austauschdienst (DAAD)

Bachelorstudium (B.Sc. Physik)
10/2009 - 09/2012 Karlsruher Institut für Technologie (KIT)
Titel der Bachelorarbeit: “Simulation und Auswertung der Energiebilanz
beim HTC Prozess einer Mehr-Kessel-Anlage anhand der Daten eines
einzelnen Reaktor-Kesselmoduls”
Gefördert durch den Deutschen Akademischen Austauschdienst (DAAD)

Schulbildung
02/2001 - 12/2008 Humboldt Schule, San José, Costa Rica